FAST CIRCULAR APERTURE SYNTHESIS IN SAR ALL-ASPECT TARGET IMAGING

A Dissertation
Presented to
The Academic Faculty

By

Jehanzeb Burki

In Partial Fulfillment
of the Requirements for the Degree
Doctor of Philosophy
in
Electrical and Computer Engineering

School of Electrical and Computer Engineering
Georgia Institute of Technology
December 2008

FAST CIRCULAR APERTURE SYNTHESIS IN SAR ALL-ASPECT TARGET IMAGING

Approved by:

Dr. Christopher F. Barnes, Advisor
Associate Professor, School of ECE
Georgia Institute of Technology

Dr. Hao Min Zhou
Associate Professor, School of Mathematics
Georgia Institute of Technology

Dr. Andrew F. Peterson
Professor, School of ECE
Georgia Institute of Technology

Dr. Justin K. Romberg
Assistant Professor, School of ECE
Georgia Institute of Technology

Dr. Douglas B. William
Professor, School of ECE
Georgia Institute of Technology

Date Approved: September 2008

TABLE OF CONTENTS

LIST OF TABLES

LIST OF FIGURES

CHAPTER 1

INTRODUCTION

Synthetic Aperture Radar (SAR) is an active coherent imaging sensor that offers all-weather, day-night, high-quality imagery. SAR is a mature but actively researched technology. Although much of the early work was aimed at military applications such as the detection and tracking of moving targets, the potential for utilizing this instrument as an imaging sensor for scientific applications was widely recognized. Applications include crop or forest condition assessment, flood and sea ice monitoring, ship and oil slick detection, land cover mapping, height mapping, and change detection. SAR has also found applications in disciplines such as forestry, geology, hydrology, oceanography and bathymetry. All SAR applications are aimed at terrain mapping or target imaging as shown in Fig. 1.1. Terrain consists of objects that cover large areas, such as fields, forests, lakes, rivers, and roads. A target is a specific object of interest that the radar illuminates. The typical target is man made and consists of multiple scattering centers. A typical SAR system has a RF/microwave front-end, front-end signal processing and back-end signal processing as shown in Fig. 1.2. The Front-end signal processing block houses the SAR focusing algorithm where as back-end processing is used for image enhancement such as speckle noise reduction. The back-end processing block may also include functionality such as automatic target recognition (ATR).

SAR imaging is not just described by a bunch of formulae; rather it *stands on the shoulders of giants* as any other evolved discipline of our age. SAR imaging shares the Huygens-Fresnel principle along with ultrasonic imaging, seismic imaging, and Fourier optics to name a few. The Green's function for SAR is identified by a cylindrical phase function. Various approximations of this Green's function have been in use, dictated by the processing technology of the time.

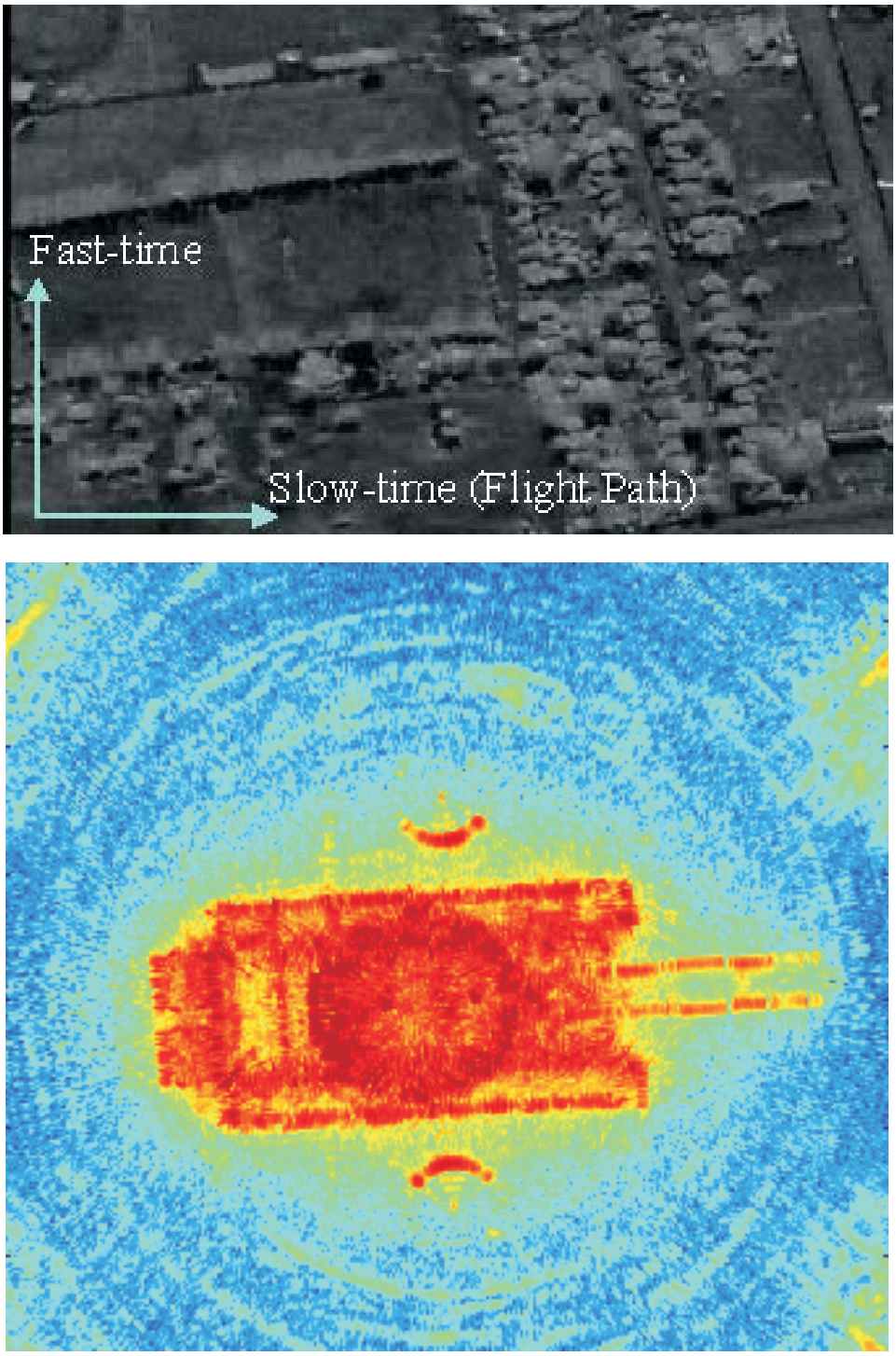

Figure 1.1. (a) Terrain mapping. (b) Target imaging.

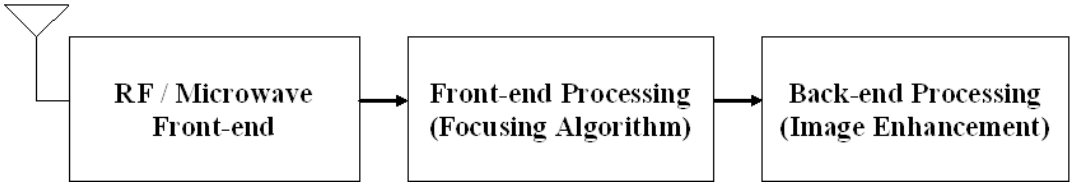

Figure 1.2. SAR system level block diagram.

In chapter 2, basic principles of SAR imaging are introduced including fast-time imaging and slow-time imaging. After a brief historical perspective, this chapter then delves straight into the Huygens-Fresnel principle and the resulting Green's function. The slant-plane SAR Fourier integral is analyzed from both a mathematics and physics stand point. The mathematical tools offered by *complex analysis* are applied to solve the integral as these tools are known to solve Laplace integrals and some Fourier integrals. This research is followed by asymptotic expansion from Harmonic analysis. It is shown that the differential equation governing SAR wave propagation is an elliptic equation and finite difference methods used to compute such equations are also discussed.

In chapter 3, the outcome of the asymptotic expansion is extended to two-dimensional (2-D) aperture synthesis, and thorough analytical development of SAR imaging with 2-D aperture synthesis is presented. The simulation results of both rectangular and circular apertures are compared to the Fraunhofer diffraction patterns from Fourier optics. Various options for filling in Fourier components are explored next, including beam raster-scanning, multi-pass imaging, sparse array imaging, and circular SAR imaging.

Chapter 4 is the heart of this dissertation where the fast circular synthetic aperture radar (CSAR) algorithm is formulated. Fourier analysis based CSAR imaging involves multidimensional aperture synthesis supplemented by fast-time imaging techniques to fill in Fourier components. This investigation in computationally efficient CSAR methods is a sequel to prior research on multidimensional aperture synthesis. A required condition for asymptotic expansion of 2-D aperture synthesis was earlier investigated that defined a circular support region in the Fourier domain. It has been shown that a circular synthetic

aperture is easily executed by a roll maneuver of an airborne platform carrying a SAR sensor; this is in contrast to challenges in creating alternate aperture shapes encountered both in Fourier optics and array processing. Our study of the Fourier optics discipline revealed results that are equally applicable to SAR imaging; that the point-spread-function (psf) is merely a Fourier transform of the aperture shape. Moreover, sparse array shapes like Very Large Array (VLA) in radio astronomy do not qualify as candidates for 2-D aperture synthesis in SAR imaging because such arrays involve an observation time of several hours to fill in Fourier components.

Linear SAR, in both stripmap and spotlight SAR modalities, typically measures a target SAR signature only over a limited aspect angle. CSAR, on the other hand, is a method of SAR imaging capable of obtaining measurements of up to a full 360° rotation or a partial segment of a circular flight path. The concept of CSAR may also be extended to space borne SAR imaging utilizing the motion of a satellite in an orbit accurately modeled as a circular trajectory. Following are the various techniques that employ slant-plane CSAR imaging.

1. The first ever CSAR processing was outlined using plane wave approximation of spherical wave function titled range-Doppler imaging of rotating objects. The resultant Polar Format Algorithm (PFA) was later used for spotlight imaging modality of SAR.

2. CSAR may also be interpreted as a tomographic reconstruction problem and analyzed using the projection-slice theorem from computer-aided tomography.

$$f(x,y) * *\mathfrak{R}_\theta[\delta(x)1(y)] \leftrightarrow F(u,v)\mathfrak{R}_\theta[1(u)\delta(v)] \tag{1.1}$$

   The signal recorded at each SAR transmission point is modeled as a portion of the Fourier transform of a central projection of the imaged ground area. Reconstruction of an SAR image may then be accomplished using traditional algorithms not based on Doppler shifts.

3. The approximation free, Fourier Analysis based CSAR approach is a recent development based on Fourier decomposition of the multidimensional shift-varying impulse response or slant-plane Green's function. This type of CSAR computes ground-plane CSAR from a projection of the slant-plane CSAR phase history data into a ground-plane phase history for further matched filtering-based target area reconstruction. An approximation to ground-plane CSAR is achieved by taking the hermitian transpose of the near-orthogonal system slant-plane-to-ground plane phase history projection model. The alternate approach involves the computationally expensive pseudo-inverse of the linear shift-varying system.

4. The back-projection CSAR algorithm correlates measured CSAR data with the analytical signature of a unit reflector at each pixel point on the desired spatial reconstruction grid to form the CSAR image of the target area.

Householder transform based processing has recently been shown to have improved error bounds and stability as an underdetermined system solver. This transform may also be applied to ill-conditioned systems with speed unmatched by any other solver. This paper proposes the use of the Householder transform to process Fourier analysis based CSAR data, thus circumventing the need for explicitly computing a pseudo-inverse in CSAR imaging.

Results presented in chapter 5 are a spin-off of our earlier research in SAR 2-D aperture synthesis. This research utilizes the methodology of the SAR 2-D aperture synthesis algorithm, a two dimensional variant of the $\omega - k$ algorithm, to refocus out-of-focus images. Refocusing of images may be necessary in machine vision as a preprocessing step before edge detection or image segmentation in the imaging and manipulation of three dimensional (3-D) objects. The SAR 2-D aperture synthesis algorithm generates a complex amplitude distribution and the corresponding psf in a manner similar to Fraunhofer diffraction distribution model and its psf as seen in Fourier optics. The matched filter utilized in the SAR 2-D aperture synthesis algorithm has a focus-in-altitude interpretation and may be

varied to increase or decrease the radius of out-of-focus blur associated with a particular psf of scatterers of various heights. This research demonstrates focusing of a line object $L = (1 : x = y \ -64 \leq x \leq 63, -64 \leq y \leq 63)$. Although a rectangular aperture is used in the refocusing process, other apertures may also be used such as circular or Gaussian.

In optical imaging, the imaging system is first focused and then data are collected. In SAR imaging, data are first collected and then focused through signal processing. Hence, a SAR signal processing algorithm is necessarily a focusing algorithm. Conventional slant-plane SAR employs two entirely different methodologies for target area image formation: a pulsed fast time imaging technique is used perpendicular to the flight path, and a "Doppler" induced slow time imaging technique is used along the flight path. The use of $\omega - k$ algorithm for slow time signal processing of slant plane SAR data is a new trend. The key concept in the SAR 2-D aperture synthesis algorithm is the extension of the one dimensional slow-time imaging technique based upon $\omega - k$ algorithm to two dimensions. In coherent optics, spherical wave illumination of an aperture produces a complex amplitude distribution proportional to the Fourier transform of the aperture transmittance function, scaled by the wavelength times the convergence distance. This is the most important result reached in the development of Fourier optics. The two dimensional variant of $\omega - k$ algorithm exposes similar complex amplitude Fraunhofer diffraction distributions as seen in Fourier optics. The matched filter has a focus-in-altitude interpretation. This work delves into this inherent focusing ability of matched filter to refocus data to one distance parameter that has been previously focused to another distance parameter. In this sense, the method provides an approach to refocus defocused images.

In machine vision, processing tasks such as edge detection, image segmentation, etc., are easier for focused images than for defocused images of 3-D scenes. However, the image of a camera is not identically focused for all objects in the camera scene. The target object and those objects at the same distance as the target object will be focused. All other objects at distances other than that of the target object will be blurred by different degrees

depending on their distance from the camera. The amount of defocus blur also depends on the camera parameters such as lens position with respect to image detector, focal length of the lens, and diameter of the camera aperture. Two blurred images of the same camera scene are usually used in the refocusing process. Initially, a blur parameter "sigma" is estimated, then one of the two blurred images is deconvolved to recover the focused image. This refocusing may be done with or without the knowledge of the camera psf.

In chapter 6, work done in SAR back-end processing in a terrain mapping application is presented. SAR image classification for late season rural land cover estimation is investigated. A novel, tree structured, nearest neighbor–like classifier is applied to polarimetric SAR intensity image pixel blocks. The novel tree structure, called a σ–tree, is generated by an ordered summation of unweighted template refinements. Computation and memory costs of a σ–tree classifier grow linearly. The reduced costs of σ–tree classifiers are obtained with the trade–off of a guarantee of nearest neighbor mappings. Causal–anti–causal refinement template design methods, combined with causal multiple stage search engine structures, are shown to yield sequential search decisions that are acceptably near neighbor mappings. The performance of a σ–tree classifier is demonstrated for rural land cover estimation with detected polarimetric C–band AirSAR pixel data. Experiments are conducted on various polarization/pixel block size combinations to evaluate the relative utility of spatial–only, polarimetric–only, and combined spatial/polarimetric classifier inputs.

Nearest neighbor classifier implementation costs, in terms of required memory and computational resources, grow in proportion to the number of exemplars available as pattern matching templates. Conventional tree structured nearest neighbor classifiers reduce computation, but increase memory requirements. A novel tree structure called a σ–tree is investigated that simultaneously reduces both computation and memory requirements. This tree structure is derived from a collection of multiple stage successive approximation templates.

Data processing can often be formulated in terms of "successive refinement," "incremental refinement" or "approximate signal processing". A progressive formulation of data processing and data representation allows for the possibility of trading accuracy or optimality of results for the consumption of resources such as system cost and complexity. Successive approximation source codes provide an architectural framework and strategy for image content classification, and are at the heart of the σ–tree concept. The type of successive approximation source code proposed here for data classification is based on direct sum data structures. This template–based classifier search engine uses direct sum structures for building efficient, data–adaptive, reduced–degree–of–freedom digital representations of target class exemplars. The σ–tree classifiers are applied in the pixel space of detected polarimetric SAR images for late season (November in southeastern United States) rural land use estimation.

The primary purpose of this research is to introduce and investigate the utility of the direct sum form of data representation in SAR image classification problems. C–band AirSAR data sets of opportunity (images and ground truth) provide us late season crop classification as the corresponding application–of–opportunity. The earlier work in this area addressed crop classification with polarimetric C–band AirSAR data for crop classification. The image sets used in this work were obtained in the early to mid stage of growth (June). They examined full complexity neural–networks, pruned complexity neural–networks, and maximum likelihood algorithms. Their data analysis show that polarimetrics should be a key discriminator, and they are able to achieve good classification results with field–based (not pixel–based) polarimetric signature classification. Their proven expectation is that polarimetrics is a key discriminator for early to mid season growth stage crops. This is due to crop canopy and ground bounce interactions, especially in cross polarizations. However, in late season classification problems, the crop canopy is usually sparse or absent, so a question addressed in this research is "can a spatial extension of the classifier's input space compensate for lack of polarimetric discriminators in late season land cover estimation?"

Our classifier is a pixel based classifier that runs a sliding window through a polarimetric SAR intensity (detected) pixel image, and extracts multiple layered snippets for classification. The stride of the sliding window is one pixel in both x and y directions. For example, if a block size of 9×9 is used for classification, the sliding window moves just one pixel to the right for the next block (or starts at the head of the next row if the end of a row is reached). This allows the classifier to assign a class label to every pixel. The stride of the sliding window can be increased to reduce the runtime of the σ–tree classifier.

Experiments are conducted for three cases: 1) with combined polarimetric/spatial blocks with 9×9 pixels and HH, VV and VH layers, 2) with polarimetric–only blocks with single pixel spatial extent and HH, VV and VH layers, and 3) with spatial–only blocks with 9×9 pixels of a single AirSAR "total power" (TP) layer. Results show that inclusion of both polarimetric and spatial information gives good classification results for feature classes of 1) unharvested cotton (85% correct), 2) cut corn stubble / picked and cut cotton / plowed areas (90% correct), 3) pasture and dried soybean areas (99% correct), 4) young pine stands (74% correct), 5) mature pine stands (100% correct) and 6) a catch–all–else "other" class. The system is less successful separating unpicked cotton with foliage (79%) from unpicked defoliated cotton (52%), and separating dried soybeans (67%) from pasture (47%). Experiments show that the inclusion of spatial content into the σ–tree classifier's input space is helpful for all classes, and that the inclusion of polarimetric content is useful for small plant ground cover (unharvested cotton and young pine trees).

Finally, a summary of the ideas and results are presented in chapter 7. Topics for further research are also discussed in this concluding chapter.

CHAPTER 2

MATHEMATICAL METHODS FOR SAR DATA FOCUSING

2.1 Origin and History

2.1.1 Slant-plane SAR Imaging

In the remote sensing context, an SAR system makes an image of the Earth's surface from a spaceborne or airborne platform [9]. It does this by pointing a radar beam approximately perpendicular to the sensor's motion vector, transmitting phase-encoded pulses, and recording the radar echoes as they reflect off the Earth's surface. To form a high-resolution image, intensity measurements must be taken in the *slant-plane* along two orthogonal directions [10], [11], [12]. In the SAR context, one dimension is parallel to the radar beam, called *range* or *fast-time*, as the time delay of the received echo is proportional to the distance or range along the beam to the scatterer. By measuring the time delay, the radar places the echo at the correct distance from the sensor, along the image's x-axis. The second dimension of the image, termed *cross-range* or *slow-time*, is given by the travel of the sensor itself. As the sensor moves along in a nominally straight line above the Earth's surface, the radar beam sweeps along the ground at approximately the same speed. The radar system emits pulses of electromagnetic energy, and the echoes received from the pulses are processed and placed in the image's y-axis, according to the sensor's current position, creating an image with geometric coordinates. The y-dimension is also called azimuth or along-track.

2.1.2 Fast-time Imaging

Slant-plane SAR fast-time imaging is most commonly based on a signal processing technique called pulse compression. Pulse compression is a type of spread spectrum method designed to minimize peak power, maximize signal-to-noise ratio, and obtain fine resolution of the sensed object. The pulse is linearly frequency modulated (FM) such that the instantaneous frequency is a linear function of time. In the time domain, an ideal linear FM

(LFM) signal or pulse has a duration of T seconds with a constant amplitude, and K is the LFM rate in Hertz per second (2.1). The phase is a quadratic function of time (2.2) and the frequency is a linear function of time (2.3). The signal bandwidth is defined as the range of frequencies spanned by the significant energy of the chirp or the frequency excursion of the signal and is given by the product of chirp slope and chirp duration (2.4). SAR fast-time imaging is shown in Fig. 2.1.

$$s(t) = rect(\frac{t}{T}) \exp(j\pi K t^2) \tag{2.1}$$

$$\phi(t) = \pi K t^2 \tag{2.2}$$

$$f = Kt \tag{2.3}$$

$$BW = \mid K \mid T \tag{2.4}$$

There are alternate approaches to fast-time imaging. One such approach transmits a band of frequencies and employs matched filtering for target reconstruction. The point spread function then depends on the spectral shape of the radar signal. For instance, when $\mid P(\omega) \mid = 1$ within the radar bandwidth, that is, $\omega \in [\omega_c - \omega_o, \omega_c + \omega_o]$, the point spread function is a sinc:

$$psf_t(t) = \exp(j\omega_c t) sinc(\frac{\omega_o t}{\pi}) \tag{2.5}$$

Discrete phase and frequency codes are useful in special situations such as RCS measurement facilities and low probability of intercept (LPI) applications. Phase codes may be binary codes with only 0 and π radians phase levels or more general polyphase codes. Binary codes include Barker codes and pseudo-random phase codes [13].

2.1.3 Slow-time Imaging

Slow-time imaging, the signal processing technique that SAR employs to achieve fine azimuth or cross-range resolution, is the feature that distinguishes SAR from other imaging radars. Moreover, slow-time imaging is firmly rooted in the concepts of scalar diffraction theory.

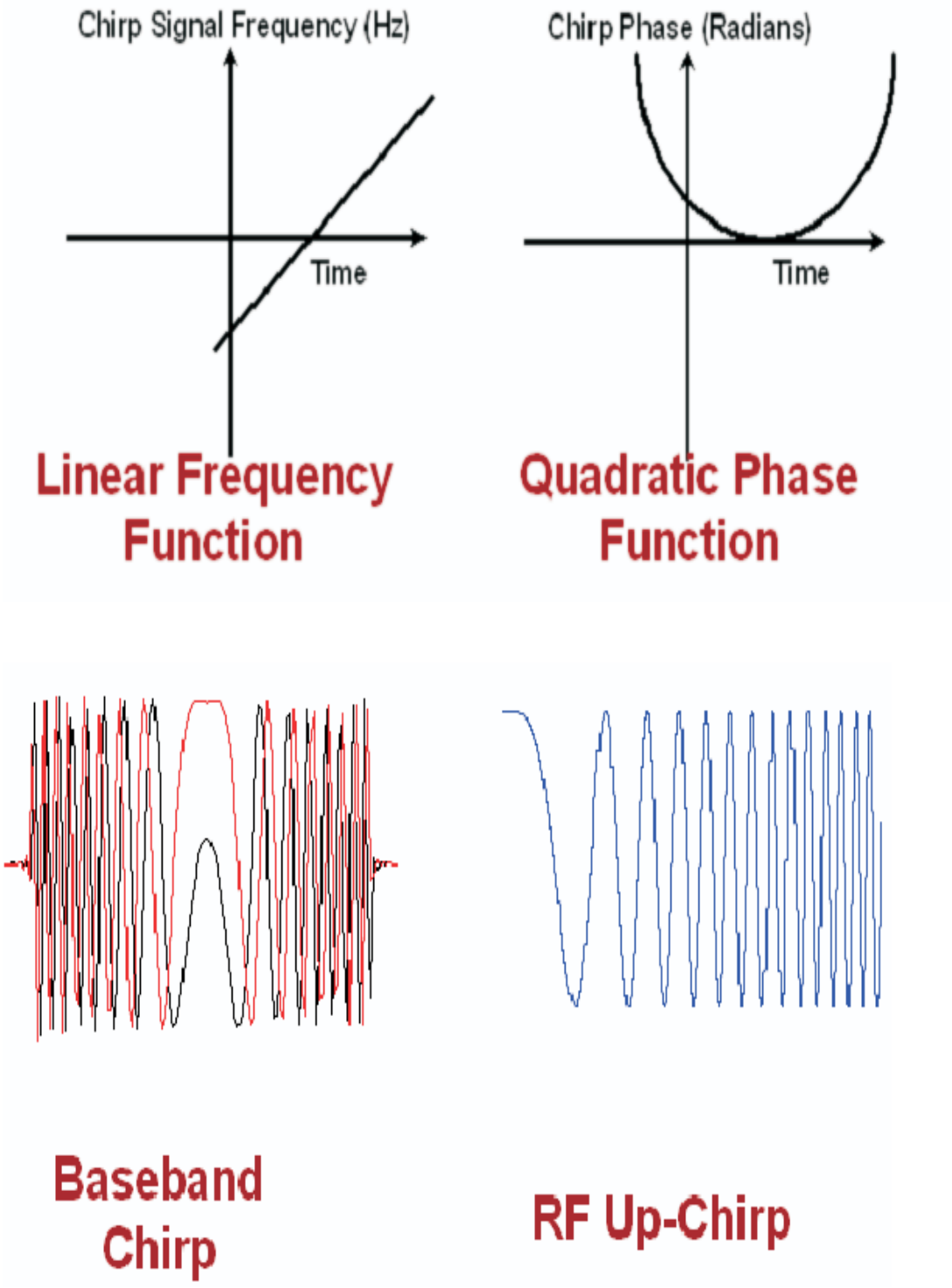

Figure 2.1. SAR fast-time imaging.

2.1.3.1 Scalar Diffraction Theory

Diffraction is the study of the relationship between the complex amplitude distribution of a propagating wave at one plane that the wavefront passes through and the complex amplitude distribution of the same wavefront at a subsequent plane. The terms interference and diffraction refer to the same basic phenomenon. The term interference is usually chosen for the interaction of a finite number of wavefronts such as when the source consists of a finite number of point sources. The term diffraction is preferred for the general situation such as when there is an uncountable infinity of interacting wavefronts. Scalar diffraction theory is a mathematical formulation of diffraction that provides a satisfactory description of the physical phenomenon of diffraction for scalar waves such as acoustic waves. Scalar diffraction theory usually gives satisfactory results even for vector waves, such as electromagnetic waves, especially if the significant dimensions in the problem are large in comparison to a wavelength. There are rare cases, however, where scalar diffraction theory is inadequate and fails to describe the physical phenomenon. Then, a richer theory, known as the vector diffraction theory, must be used. The scalar diffraction theory is precisely described by the Huygens-Fresnel principle, which describes a wavefront, $s(x, y, z)$, on the x, y plane at $z = d$ in terms of that wavefront on a previous x, y plane at $z = 0$.

2.1.3.2 Timeline

In 1678 Christian Huygens wrote on the wave theory of light, expressing the intuitive conviction that if each point on the wavefront of a disturbance at time t were considered to be a new source of a secondary spherical disturbance, then the wavefront at a later instant $t + \Delta t$ could be found by constructing the envelope of the secondary wavelets, as illustrated in Fig. 2.2.

In 1804, Thomas Young strengthened the wave theory of light by introducing the critical concept of *interference*. Later in 1818, Augustin Jean Fresnel was able to calculate the distribution of light in diffraction patterns with excellent accuracy. In 1860 Maxwell identified light as an electromagnetic wave, a step of enormous import. But it was not until 1882 that

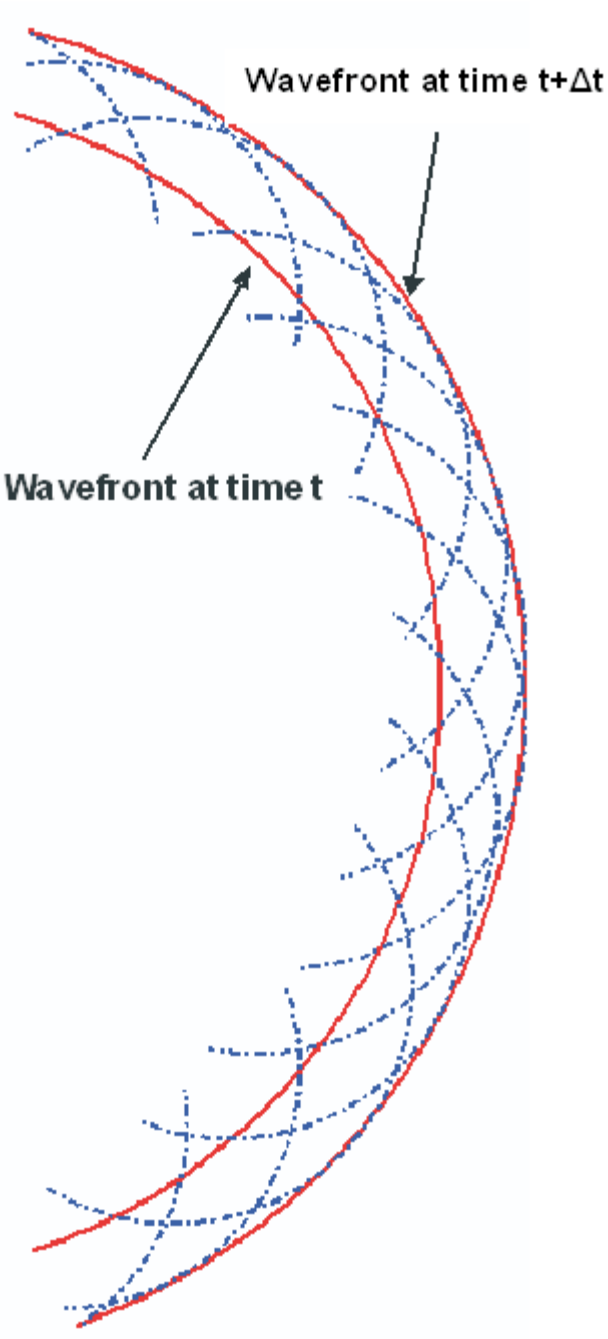

Figure 2.2. Huygens' envelope construction.

Gustav Kirchoff put previous ideas on a firmer mathematical foundation by showing that the amplitudes and phases ascribed to the secondary sources by Fresnel were indeed logical consequences of the wave nature of light. Kirchhoff's theory was based on simplifications and approximations. Most important, light is treated as a scalar phenomenon, neglecting the fundamentally vectorial nature of the electromagnetic fields. However, scalar theory yields accurate results if two conditions are met: (1) the diffracting aperture must be large compared with a wavelength, and (2) the diffracting fields must not be observed too close to the aperture. In principle, the diffraction of electromagnetic waves should be explained directly from Maxwell's equations, which give a complete description of electromagnetic fields. However, there may be mathematical difficulties when starting from first principles because there may be concerns about how to model a given problem or how to specify a consistent and accurate set of boundary conditions. It may be difficult to formulate the boundary conditions at a level of detail needed to apply Maxwell's equations, while the weaker conditions needed for diffraction theory may be readily apparent. This is why the theory of diffraction is formulated as distinct, but subservient to, electromagnetic theory.

In 1948, Dennis Gabor based his wavefront reconstruction theory, also called holography, on the scalar wave theory. This theory is the principal foundation of many imaging systems in optics, geophysics, and diagnostic medicine. Gabor recognized that when a suitable coherent reference wave is present simultaneously with the light diffracted by or scattered from an object, information about both the amplitude and phase of the diffracted or scattered waves can be recorded. In 1962 E. N. Leith and J. Upatnieks modified Gabor's original technique by the offset-reference hologram and applied it to SAR proposed by Carl Wiley in 1951 [14], [15], [16], [17]. However, the lack of fast computing machines and advanced digital signal processing algorithms at that time prevented the development of wavefront reconstruction-based SAR imaging methods. The early SAR systems were based on the optical processing of the measured echoed signal using the Fresnel approximation for image formation. This SAR processor, in the analog form or its digital version

which was introduced for the space borne SAR in the late 1970s, is also known as rang-Doppler imaging (RDI). In the 1970s another SAR imaging method, known as polar format processing (PFA), was introduced for high-resolution spotlight SAR systems. This method was based on plane wave approximation. The first digital signal processing-based methods for SAR image formation via the wavefront reconstruction theory were introduced in the late 1980s to early 1990's.

2.1.3.3 Huygens-Fresnel Principle and Green's Function

The scalar diffraction theory is precisely described by the Huygens-Fresnel principle, which describes a wavefront, $s(x, y, z)$, on the x, y plane at $z = d$ in terms of that wavefront on a previous x, y plane at $z = 0$. Moreover, $h(x, y)$ is known as the Huygens-Fresnel point spread function (2.6) [18]. The signal processing term point spread function may be called a Green's function in the study of wave propagation, though the term Green's function usually refers to the kernel of a three-dimensional convolution rather than that of a two-dimensional convolution [19], [20].

$$s(x, y, d) = h(x, y) * *s(x, y, 0) \tag{2.6}$$

The Green's function satisfies the following differential equation [21] called Helmholtz equation:

$$\frac{\partial^2}{\partial x^2}h(x, y) + \frac{\partial^2}{\partial y^2}h(x, y) + k^2 h(x, y) = -\delta(x, y) \tag{2.7}$$

where k wavenumber is a constant and $\delta(x, y)$ is the impulse input. Equation (2.7) can be written as a linear operator on $h(x, y)$ as follows:

$$[\frac{\partial^2}{\partial x^2} + \frac{\partial^2}{\partial y^2} + k^2]h(x, y) = -\delta(x, y) \tag{2.8}$$

where $\frac{\partial^2}{\partial x^2} + \frac{\partial^2}{\partial y^2} \equiv \nabla^2$ is called the Laplacian operator. The differential equation (2.8) is commonly written in the following form:

$$[\nabla^2 + k^2]h(x, y) = -\delta(x, y) \tag{2.9}$$

Taking the two-dimensional Fourier transform of both sides, we get

$$[-k_x^2 - k_y^2 + k^2]H(k_x, k_y) = -1 \tag{2.10}$$

or equivalently,

$$H(k_x, k_y) = \frac{1}{k_x^2 + k_y^2 - k^2} \tag{2.11}$$

A similar principle also exists for the three-dimensional spatial domain (x, y, z). The impulse response $h(x, y)$ is known as the free-space Green's function. This signal is the radiation pattern of an ideal point source that emits a wave at temporal frequency ω in a homogeneous medium with propagation speed c, and $k = \frac{\omega}{c}$ is called the wavenumber. For two-dimensional geometries, the Green's function is

$$h(x, y) = j\pi H_o(k\sqrt{x^2 + y^2}) = j\pi H_o(kr) \tag{2.12}$$

where $H_o(.)$ is the zero-th order Hankel function of the first kind, and $r = \sqrt{x^2 + y^2}$. It can be shown that

$$lim_{kr\to\infty} H_o(kr) \approx \sqrt{\frac{2}{\pi kr}} e^{-j\frac{\pi}{4}} \exp(jkr) \tag{2.13}$$

The asymptotic expression (2.13) is a valid approximation for the Green's function when $r \gg \lambda \equiv \frac{2\pi}{k}$. The Green's function in the three-dimensional spatial domain for diverging spherical-wave solution to Helmhotz equation is

$$h(x, y, z) = \frac{\exp(jkr)}{r} \tag{2.14}$$

where $r = \sqrt{x^2 + y^2 + z^2}$. In SAR imaging problems, the distances are sufficiently large such that the phase functions of the two-dimensional and three-dimensional Green's functions both behave as $\exp(jkr)$. Moreover, their amplitude functions vary very slowly with respect to their phase functions and do not play an important role in the imaging problem. Therefore, Green's function is identified with the cylindrical phase function $\exp(jk\sqrt{x^2 + y^2})$ and the spherical phase function $\exp(jk\sqrt{x^2 + y^2 + z^2})$.

2.1.3.4 Slant-plane SAR Green's Function

The Green's function for the SAR-specific scenario, for synthetic aperture position u along $y - axis$, may be written as $\exp(jk\sqrt{x^2 + (y-u)^2 + z^2})$. This three-dimensional Green's function is simplified into the two-dimensional slant-plane SAR Green's function by synthesizing the *linear* aperture as follows:

$$\exp(jk\sqrt{x^2 + (y-u)^2 + z^2}) = \exp(jk\sqrt{x_{slant}^2 + (y-u)^2}) \tag{2.15}$$

where $x_{slant}^2 = x^2 + z^2$. The subscript *slant* will not be explicitly mentioned in all future references to slant-plane SAR Green's function. Moreover, if X_c is the scene center along the range dimension, we may rewrite Green's function as $\exp(jk\sqrt{(X_c + x)^2 + (y-u)^2})$.

2.1.3.5 Fresnel Approximation

It is known from fast-time imaging that the instantaneous frequency of a chirp signal is a linear function. Similarly, the Fresnel approximation of SAR's slant-plane Green's function yields a chirp that is quadratic in phase so that the instantaneous spatial frequency is a linear function. This is achieved by a Taylor series expansion, assuming $(y-u) \ll (X_c + x)$, and neglecting the higher order terms to obtain

$$\exp(jk\sqrt{(X_c + x)^2 + (y-u)^2}) \approx \exp[jk(X_c + x) + j\frac{k(y-u)^2}{2X_c}] \tag{2.16}$$

Although implementable via optical analogue signal processing techniques of the time, the Fresnel approximation later proved unsuitable for high-resolution SAR imaging. The Fresnel approximation results in significant phase errors and degradations in the reconstructed SAR image. SAR imaging based on a Fresnel approximation was termed range-Doppler imaging (RDI) and the initial space-based systems employed a Fresnel approximation [22], [23], [24].

2.1.3.6 Plane-wave Approximation

Suppose that the center of the target area is (X_c, Y_c), then

$$\sqrt{(X_c + x)^2 + (Y_c + y - u)^2} \approx \sqrt{X_c^2 + (Y_c - u)^2} + cos\theta_o(u)x + sin\theta_o(u)y \tag{2.17}$$

where $\theta_o(u) = arctan(\frac{Y_c - u}{X_c})$ is the aspect angle of the radar with respect to the center of the target area at the slow-time synthetic aperture position u. The name "polar format processing" given to a plane wave approximation-based reconstruction stems from the fact that the samples of the SAR signal are mapped into polar samples of the target function in the spatial frequency domain. This approximation neglects the wavefront curvature in the spherical PM signal and results in spatially varying smearing and shifting of the targets in the imaging scene. For the validity of this approximation, certain conditions must be met in terms of the size of the target area, the radar frequency, and the extent of the synthetic aperture u. Polar format processing is also used in conjunction with narrow-beam width and narrow-bandwidth approximations

2.1.3.7 Slant-plane SAR Fourier Integral

The purpose of the Fresnel approximation as well as the plane-wave approximation is to solve the following Fourier integral:

$$\int_{-\infty}^{\infty} \sigma_n \exp(-j2k\sqrt{x_n^2 + (y_n - u)^2}) \exp(-jk_u u) du \tag{2.18}$$

where σ_n is the n^{th} target reflectivity and k_u represents the slow-time spatial frequency domain.

2.2 Mathematical Methods

2.2.1 Complex Analysis

Complex analysis is the branch of mathematics investigating functions of complex variables. *Cauchy's residue theorem*, a crucial tool in solving certain indefinite integrals, was explored as a possible solution to the slant-plane SAR Fourier integral.

2.2.1.1 Residue Theory

Let C be a simple closed contour, described in the positive sense. If a function f is analytic inside C except for a finite number of isolated singular points $z_k (k = 1, 2, ..., n)$ inside C,

then [25]

$$\int_C f(z)dz = 2\pi i \sum_{k=1}^{n} Res_{z=z_k} f(z) \tag{2.19}$$

An isolated singular point z_o is the point at which function f fails to be analytic and there is a deleted neighborhood $0 <\mid z - z_o \mid < \varepsilon$ of z_o throughout which f is analytic. The counterclockwise direction is considered positive in the above stated theorem. In turn, Cauchy's residue theorem is based on Cauchy's integral formula. When z_o is an isolated singular point of a function f, there is a positive number δ such that f is analytic at each point z for which $0 <\mid z - z_o \mid < \delta$. Consequently, $f(z)$ is represented by a Laurent series

$$f(z) = \sum_{n=0}^{\infty} a_n (z - z_o)^n + \frac{b_1}{z - z_o} + \frac{b_2}{z - z_o}^2 + ... \tag{2.20}$$

where the coefficients a_n and b_n have certain integral representations for $n = 0, 1, 2....$

$$a_n = \frac{1}{2\pi i} \int_C \frac{f(z)dz}{(z - z_o)^{n+1}} \tag{2.21}$$

$$b_n = \frac{1}{2\pi i} \int_C \frac{f(z)dz}{(z - z_o)^{-n+1}} \tag{2.22}$$

where C is any positively oriented simple closed contour around z_o and lying in the punctured disk $0 <\mid z - z_o \mid < \delta$. When n=1 this expression for b_n can be written as

$$\int_C f(z)dz = 2\pi i b_1 \tag{2.23}$$

The complex number b_1 is called the residue of f at the isolated singular point z_o. The following theorem provides an alternative characterization of poles and another way of finding the corresponding residues. An isolated singular point z_o of a function f is a pole of order m if and only if $f(z)$ can be written in the form

$$f(z)dz = \frac{\phi(z)}{(z - z_o)^m} \tag{2.24}$$

where $\phi(z)$ is analytic and nonzero at z_o. Moreover, $Res_{z=z_o} f(z) = \phi(z_o)$ for m=1. In calculus, the improper integral of a continuous function $f(x)$ over the semi-infinite interval $x \geq 0$ is defined by means of

$$\int_0^{\infty} f(x)dx = lim_{R\to\infty} \int_0^R f(x)dx \tag{2.25}$$

When the limit on the right exists, the improper integral is said to converge to that limit. If $f(x)$ is continuous for all x, its improper integral over the infinite interval $-\infty < x < \infty$ is defined by writing

$$\int_{-\infty}^{\infty} f(x)dx = lim_{R_1\to\infty} \int_{-R_1}^{0} f(x)dx + lim_{R_2\to\infty} \int_{0}^{R_2} f(x)dx \tag{2.26}$$

When both of the limits here exist, the integral converges to their sum. The Cauchy principal value (P.V.) assigned to the above integral is

$$P.V. \int_{-\infty}^{\infty} f(x)dx = lim_{R\to\infty} \int_{-R}^{R} f(x)dx \tag{2.27}$$

2.2.1.2 Laplace Transform

Laplace transforms are important in solving both ordinary and partial differential equations. Suppose that a function F of the complex variable s is analytic throughout the finite s plane except for a finite number of isolated singularities. Then, let L_R denote a vertical line segment from $s = \gamma - iR$ to $s = \gamma + iR$, where the constant γ is positive and large enough that the singularities of F all lie to the left of that segment, as shown in Fig. 2.3. A new function f of the real variable t is defined for positive values of t by means of

$$f(t) = \frac{1}{2\pi i} lim_{R\to\infty} \int_{L_R} e^{st} F(s)ds \qquad (t > 0) \tag{2.28}$$

This expression is usually written as the Bromwich integral as

$$f(t) = \frac{1}{2\pi i} P.V. \int_{\gamma-i\infty}^{\gamma+i\infty} e^{st} F(s)ds \qquad (t > 0) \tag{2.29}$$

The function $f(t)$ is the inverse Laplace transform of $F(s)$ and can be retrieved by means of the above equation. The choice of positive number γ is immaterial as long as the singularities of F all lie to the left of L_R. Applying residue theory, the function $f(t)$ is obtained as follows:

$$f(t) = \sum_{n=1}^{\infty} Res_{s=s_n}[e^{st} F(s)] \qquad (t > 0) \tag{2.30}$$

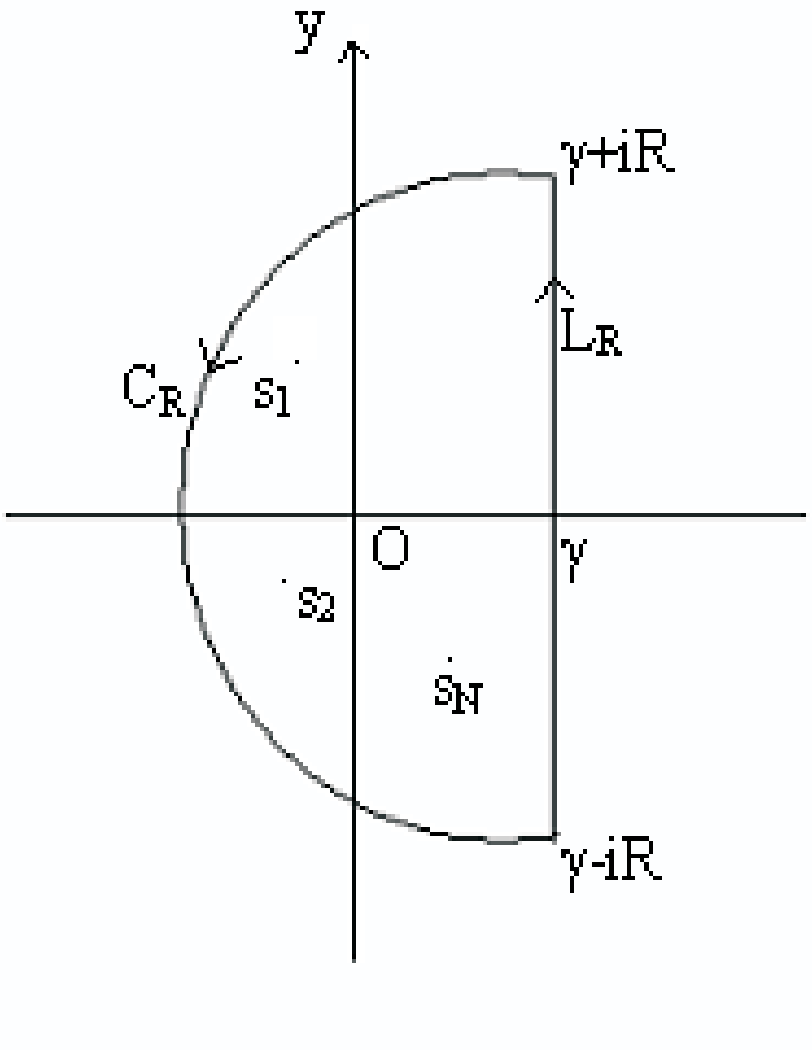

Figure 2.3. Isolated singularities inside closed contour.

2.2.1.3 *Improper Integrals from Fourier Analysis*

Residue theory is useful in evaluating convergent improper integrals of the form

$$\int_{-\infty}^{\infty} f(x)\sin axdx \quad or \quad \int_{-\infty}^{\infty} f(x)\cos axdx \tag{2.31}$$

where a denotes a positive constant, and $f(x) = \frac{p(x)}{q(x)}$, where $p(x)$ and $q(x)$ are polynomials with real coefficients and no factors in common. Integrals of this type occur in theory and application of the Fourier integral:

$$\int_{-R}^{R} f(x)\cos axdx + j\int_{-R}^{R} f(x)\sin axdx = \int_{-R}^{R} f(x)e^{jax}dx \tag{2.32}$$

The modulus $\mid e^{jaz} \mid = \mid e^{ja(x+jy)} \mid = \mid e^{jax}e^{-ay)} \mid = e^{-ay}$ is bounded in the upper half plane $y \geq 0$. Residue theory is successfully used to compute Fresnel integrals of diffraction theory. However, the slant-plane SAR Fourier integral cannot be computed with residue theory, as the integrand function has no singularities and is not *meromorphic*:

$$\int_{-\infty}^{\infty} \sigma_n \exp(-j2k\sqrt{x_n^2 + (y_n - u)^2})\exp(-jk_u u)du \tag{2.33}$$

In fact, all functions of the form e^z are *holomorphic* as they are analytic everywhere and are also termed *entire* functions. This can also be confirmed by Cauchy-Riemann equations

$$u_x(x,y) = v_y(x,y) \qquad u_y(x,y) = -v_x(x,y) \tag{2.34}$$

2.2.2 Harmonic Analysis

Fourier analysis involves the linear operation that transforms a function into the coefficients of sinusoidal basis functions and is rooted in the Huygens-Fresnel principle. The original concept of Fourier analysis has been extended over time to apply to more and more abstract and general situations, and the general field is often known as harmonic analysis. All SAR algorithms involve Fourier analysis, either explicitly or implicitly. In fact the imaging problem in nature in biological organisms is also solved using Fourier analysis by the use of a *lens* that is shown to be a Fourier transformer. The "method of stationary phase" is the central analytical tool used for the asymptotic expansion of Fourier integrals.

2.2.2.1 *Asymptotic Expansion*

The slant-plane SAR Fourier integral may be written as [26]

$$\int_{-\infty}^{\infty} \sigma_n \exp(-j2k\sqrt{x_n^2 + (y_n - u)^2} - jk_u u)du \tag{2.35}$$

The asymptotic expansion as $k_u \to \infty$ of integrals of the form

$$I(k_u) = \int_b^a \exp(jk_u\phi(u))f(u)du \tag{2.36}$$

with ϕ real. The critical or stationary point c may be computed as $\frac{d\phi(u)}{du} = 0$. Then, the asymptotic expansion may be written as

$$I(k_u) \approx \exp(jk_u\phi(c))f(c)\sqrt{\frac{2\pi}{k_u \mid \phi''(c) \mid}}\exp(\frac{\pi j\mu}{4}) \tag{2.37}$$

where $\mu = sgn\phi''(c)$. The result may be written as

$$\sigma_n \frac{\exp(-j\pi/4)}{\sqrt{4k^2 - k_u^2}} \exp(-j\sqrt{4k^2 - k_u^2}x_n - jk_u y_n) \tag{2.38}$$

for $k_u \in [-2k, 2k]$ and zero otherwise. The amplitude does not play an important role in our analysis. For notational simplicity we suppress this amplitude function to give more prominence to the phase term $\exp(-j\sqrt{4k^2 - k_u^2}x - jk_u y)$. The SAR algorithm based on the above development is often called the *range migration* algorithm or $\omega - k$ algorithm [27], [28], [29].

2.2.3 Finite Difference Methods

The field of computational electromagnetics uses finite difference time-domain and finite element frequency-domain methods to determine electric and magnetic fields residing on conducting and dielectric surfaces using integral and differential equations [30]. If we recall following equations from chapter 1

$$\frac{\partial^2}{\partial x^2}h(x, y) + \frac{\partial^2}{\partial y^2}h(x, y) + k^2 h(x, y) = -\delta(x, y) \tag{2.39}$$

where k wavenumber is a constant and $\delta(x, y)$ is the impulse input. Equation (2.39) can be written as a linear operator on $h(x, y)$ as follows:

$$[\frac{\partial^2}{\partial x^2} + \frac{\partial^2}{\partial y^2} + k^2]h(x, y) = -\delta(x, y) \tag{2.40}$$

where $\frac{\partial^2}{\partial x^2} + \frac{\partial^2}{\partial y^2} \equiv \nabla^2$ is called the Laplacian operator. The differential equation (2.40) is commonly written in the following form:

$$[\nabla^2 + k^2]h(x, y) = -\delta(x, y) \tag{2.41}$$

The possibility of solving SAR imaging problem using the above-mentioned second-order partial differential equation (PDE) by employing finite difference time-domain methods was also explored. The PDE governing SAR wave propagation is elliptic. The general form of an elliptic PDE is

$$AU_{xx} + 2BU_{xy} + CU_{yy} = f(x, y, U, U_x, U_y) \tag{2.42}$$

The coefficients A, B and C may be functions of x, y and U provided that $B^2 - AC < 0$. Specifically, this equation may be written as the Poisson equation

$$\nabla^2 U = -f(x, y) \tag{2.43}$$

Firstly, finite difference techniques are used to solve localized problems like heat transfer on a body and secondly, some sort of boundary conditions are also required, Dirichlet or Newmann. SAR is a problem in the far-field and the extent of the SAR imaging scene renders finite difference methods unfeasible. On top of this, the SAR imaging problem has unknown boundary conditions. Moreover, the imaging problem in nature is solved using Fourier transformation as mentioned in section 3.3.4. Nevertheless, finite difference techniques may play a role in the post-processing or image enhancement block of the SAR system depicted in Fig. 1.2. There has been a lot of work in recent years in both finite difference and finite element techniques. This area may prove to be of interest for future research into numerically viable SAR reconstruction techniques. We will have to dive into the knowledge base called *inverse problems*, contributed primarily by physicists and mathematicians, with our understanding of SAR mathematical problem as well as numerical PDE solving techniques.

CHAPTER 3

SAR WITH TWO-DIMENSIONAL (2-D) APERTURE SYNTHESIS [1], [2], [3]

SAR imaging is not just described by a bunch of formulae. Rather it *stands on the shoulders of giants* as any other evolved discipline of our age. SAR imaging shares the Huygens-Fresnel principle along with ultrasonic imaging, seismic imaging, and Fourier optics to name a few. The Green's function for SAR is identified by a cylindrical phase function. Various approximations to this Green's function have been in use, dictated by the processing technology of the time.

The preliminary research, presented in the previous chapter, was based on the slant-plane SAR Fourier integral. This integral was analyzed from both a mathematics and physics perspective. The mathematical tools offered by *complex analysis* were applied to solve the integral, as these tools are known to solve Laplace integrals and some Fourier integrals. This research was followed by asymptotic expansion from Fourier analysis. In this chapter, the outcome of the asymptotic expansion is extended to two-dimensional (2-D) aperture synthesis, and a thorough analytical development for SAR imaging with 2-D aperture synthesis is presented. The simulation results of both rectangular and circular apertures are compared to the Fraunhofer diffraction patterns from Fourier optics. Various options for filling in Fourier components are explored next, including beam raster scanning, multi-pass imaging, sparse array imaging and circular SAR imaging.

3.1 Asymptotic Expansion for 2-D Aperture Synthesis

The preceding results may now be extended to two-dimensional aperture synthesis to compute the dominant term of the asymptotic expansion [31], [32]. The Fourier transform may be written as:

$$\int\int_{-\infty}^{\infty} \sigma_n \exp(-j2k\sqrt{(x_n-u)^2+(y_n-v)^2+z_n^2} - jk_u u - jk_v v)dudv \tag{3.1}$$

where u is the range synthetic aperture and v is the cross-range synthetic aperture. The corresponding asymptotic expansion may be written as:

$$\approx \sigma_n \exp(-jk_u x_n - jk_v y_n - j\sqrt{4k^2 - k_u^2 - k_v^2} z_n) \tag{3.2}$$

for $\sqrt{k_u^2 + k_v^2} \leq 2k$, and zero otherwise; k_u is the range spatial frequency and k_v is the cross-range spatial frequency.

3.2 SAR with 2-D Aperture Synthesis

The analytical development for SAR imaging based on 2-D aperture synthesis is presented next [2]. There are certain SAR signal processing aspects ignored in order to simplify the SAR mathematical model, including losses resulting from free space propagation, antenna radiation pattern, squint imaging issues, and frequency-dependent target reflectivity. Moreover, the mathematical formulation is done for an infinite synthetic aperture so as to present the results with minimum mathematical complexity.

3.2.1 Target Area

Figure 3.1 shows a 2-D target area in the x-y plane of an otherwise 3-D cartesian coordinate system. The stationary point target in this imaging scene is located at $(x_n, y_n, 0)$ and the coordinates of center of target area are at $(X_c, Y_c, 0)$ such that $X_c = Y_c = 0$ for broadside imaging. The ideal target function in the $x - y$ plane may then be defined as

$$f_o(x, y) = \sum_n \sigma_n \delta(x - x_n, y - y_n) \tag{3.3}$$

where σ_n is the radar cross-section or target reflectivity of the n^{th} point target in the imaging scene. The spatial Fourier transform of the ideal target function is

$$F_o(k_x, k_y) = \sum_n \sigma_n \exp(-jk_x x_n - jk_y y_n) \tag{3.4}$$

where k_x and k_y are spatial frequency in the Fourier domain corresponding to x range and y cross-range, respectively.

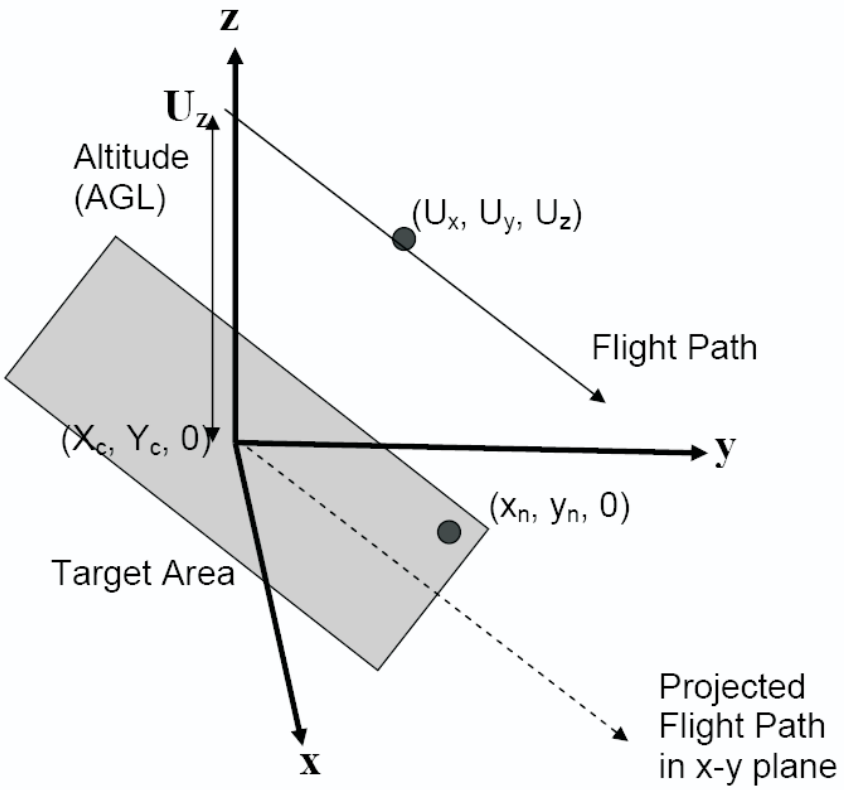

Figure 3.1. SAR 2-D aperture synthesis geometry.

3.2.2 Radar Echo and Baseband Conversion

The transmitted signal $p(t)$ is a single frequency ω such that $p(t) = \exp(j\omega t)$, where t is the fast-time. Let the position of radar at any instant be given by coordinates (U_x, U_y, U_z) [33], [34], where U_z is the position of the SAR along the $z - axis$ and a known parameter. Then, the radar distance from the point target located at $(x_n, y_n, 0)$ is given as

$$R_n(U_x, U_y) = \sqrt{(x_n - U_x)^2 + (y_n - U_y)^2 + U_z^2} \tag{3.5}$$

The received or echoed signal may be written as

$$ss(t, U_x, U_y) = \sum_n \sigma_n p(t - \frac{2}{c}\sqrt{(x_n - U_x)^2 + (y_n - U_y)^2 + U_z^2}) \tag{3.6}$$

where c is speed of light, or

$$ss(t, U_x, U_y) = \exp(j\omega t) \sum_n \sigma_n \exp(-j2k_\omega \sqrt{(x_n - U_x)^2 + (y_n - U_y)^2 + U_z^2}) \tag{3.7}$$

where the wavenumber $k_\omega = \frac{\omega}{c}$. After fast-time baseband conversion implemented in the hardware,

$$S\,s(\omega, U_x, U_y) = \sum_n \sigma_n \exp(-j2k_\omega \sqrt{(x_n - U_x)^2 + (y_n - U_y)^2 + U_z^2}) \tag{3.8}$$

3.2.3 2-D Fourier Transform

The Fourier transform of the baseband converted signal is

$$S\,S\,(\omega, k_{ux}, k_{uy}) = \int \int_{-\infty}^{\infty} S\,s(\omega, U_x, U_y) \exp(-jk_{ux}U_x - jk_{uy}U_y dU_x dU_y \tag{3.9}$$

To evaluate the Fourier transform of the above 2-D phase modulated (PM) signal, the leading or dominant term of this Fourier integral is determined by asymptotic expansion using the method of stationary phase (MSP), to obtain

$$S\,S\,(\omega, k_{ux}, k_{uy}) = \sum_n \sigma_n \exp(-jk_{ux}x_n - jk_{uy}y_n - j\sqrt{4k_\omega^2 - k_{ux}^2 - k_{uy}^2}U_z) \tag{3.10}$$

for $\sqrt{k_{ux}^2 - k_{uy}^2} \leq 2k_\omega$ and zero otherwise. k_{uy} is the range synthetic aperture spatial frequency corresponding to U_x and k_{ux} is the cross-range synthetic aperture spatial frequency

corresponding to U_y. We can rewrite this Fourier transform as

$$SS(\omega, k_{ux}, k_{uy}) = \sum_n \sigma_n \exp(-jk_{ux}x_n - jk_{uy}y_n - jk_{uz}U_z) \tag{3.11}$$

where the 2-D SAR spatial frequency mapping is

$$k_x = k_{ux} \qquad k_y = k_{uy} \tag{3.12}$$

Note that Stolt interpolation is not required for the 2-D target grid in the x-y plane because the spatial frequency domain for range and cross-range is a direct mapping of the spatial frequency domain of the 2-D synthetic aperture. The identity

$$k_z = \sqrt{4k_\omega^2 - k_x^2 - k_y^2} \tag{3.13}$$

is known as Stolt transformation [35], [36]. Finally, we can separate out the target informative part as

$$SS(\omega, k_x, k_y) = \exp(-jk_zU_z) \sum_n \sigma_n \exp(-jk_xx_n - jk_yy_n) \tag{3.14}$$

In practice, the Fourier transform is computed using the fast Fourier transform (FFT) algorithm [37].

3.2.4 Reconstruction by Matched Filtering

The reference signal for the scene-centered matched filter may be written as

$$Ss_o(\omega, U_x, U_y) = \sum_n \sigma_n \exp(-j2k_\omega \sqrt{(X_c - U_x)^2 + (Y_c - U_y)^2 + U_z^2}) \tag{3.15}$$

and the Fourier transform as

$$SS_o(\omega, k_x, k_y) = \sum_n \sigma_n \exp(-jk_xX_c - jk_yY_c - jk_zU_z) \tag{3.16}$$

since the scene center is the origin of the coordinate system in the *broadside* imaging case. Therefore,

$$SS_o(\omega, k_x, k_y) = \sum_n \sigma_n \exp(-jk_zU_z) \tag{3.17}$$

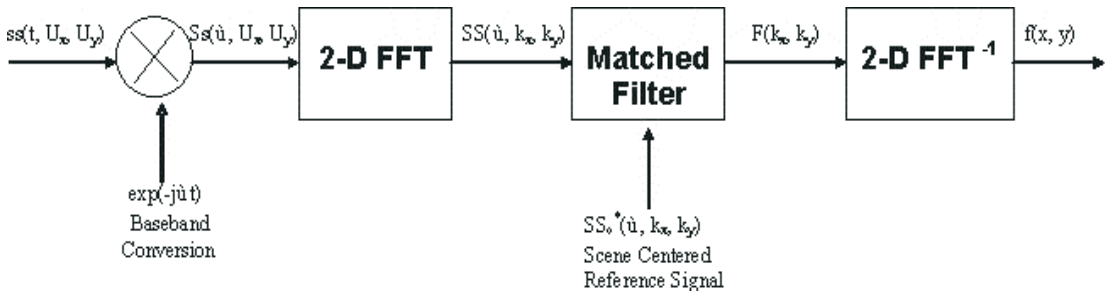

Figure 3.2. Block diagram for SAR 2-D aperture synthesis.

From equations (3.15), (3.16) and (3.17), we obtain

$$SS(\omega, k_x, k_y) = SS_o(\omega, k_x, k_y)F_o(k_x, k_y) \tag{3.18}$$

Hence, the matched filtering

$$F(k_x, k_y) = SS(\omega, k_x, k_y)SS_o^*(\omega, k_x, k_y) \tag{3.19}$$

where $*$ denotes complex conjugate. Finally, we obtain

$$F(k_x, k_y) = \sum_n \sigma_n \exp(-jk_x x_n - jk_y y_n) \tag{3.20}$$

3.2.5 2-D Inverse Fourier Transform

Finally, the inverse Fourier transform is computed for the output of the matched filter as

$$F(k_x, k_y) \overset{F^{-1}}{\rightarrow} f(x, y) \tag{3.21}$$

$$f(x, y) = \frac{1}{(2\pi)^2} \sum_n \sigma_n \int \int_{-\infty}^{\infty} F(k_x, k_y) \exp(jk_x x + jk_y y) dk_x dk_y \tag{3.22}$$

$$f(x, y) = \frac{1}{(2\pi)^2} \int \int_{-\infty}^{\infty} \exp(-jk_x x_n - jk_y y_n) \exp(jk_x x + jk_y y) dk_x dk_y \tag{3.23}$$

Ideally,

$$f(x, y) = \frac{1}{(2\pi)^2} \sum_n \sigma_n \delta(x - x_n)\delta(y - y_n) \tag{3.24}$$

Figure 3.2 is the overall block diagram of the SAR 2-D aperture synthesis technique.

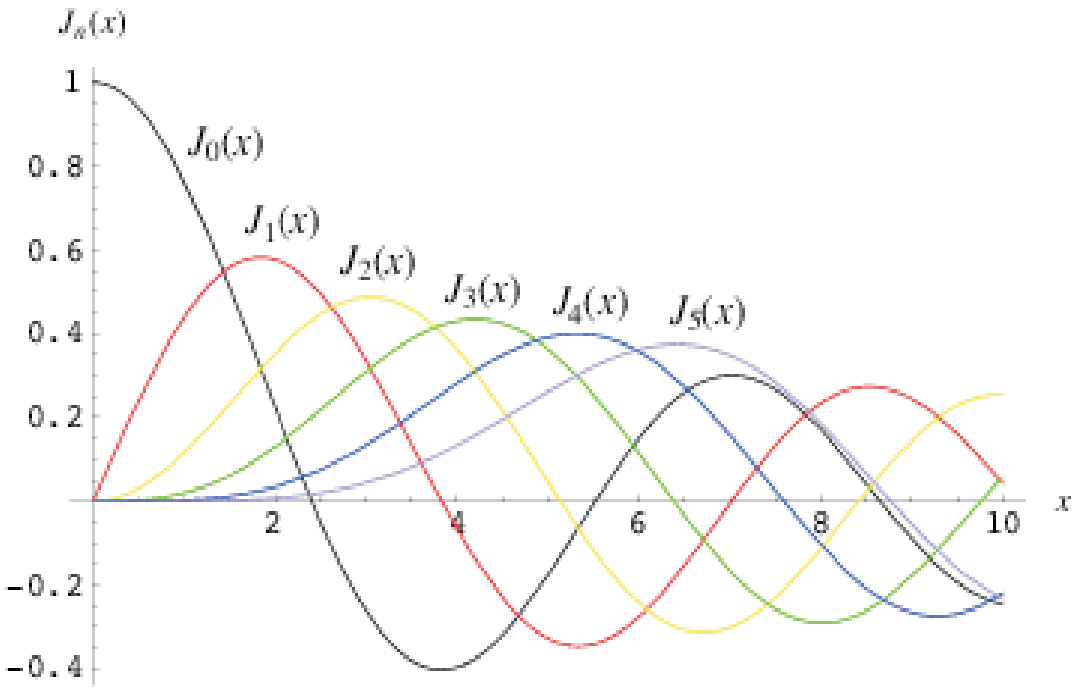

Figure 3.3. Bessel functions of first kind.

3.2.6 Point Spread Function (PSF)

The condition $\sqrt{k_x^2 - k_y^2} \leq 2k_\omega$ and zero otherwise signifies a disk shaped limited spatial Fourier support for k_x and k_y. Therefore, the resulting psf would not be an ideal 2-D separable impulse function. Instead, it would be a composite function of a non-separable first order Bessel function of the first kind J_1 [38] of Fig. 3.3, called *Sombrero* or *Besinc*, depicted in Fig. 3.4.

$$f(x,y) = \sum_n \sigma_n (2k_\omega)^2 \frac{J_1(2k_\omega \sqrt{(x-x_n)^2 + (y-y_n)^2})}{2k_\omega \sqrt{(x-x_n)^2 + (y-y_n)^2}} \tag{3.25}$$

3.2.7 Novel Aspects of SAR 2-D Aperture Synthesis

1. The $\omega - k$ or range migration algorithm (RMA) requires a 1-D interpolation known as Stolt interpolation that compensates the range curvature of all scatterers by an appropriate warping of the wavenumber domain backscatter data. This Stolt interpolation is the most computationally difficult step in the algorithm [39] and an approximation

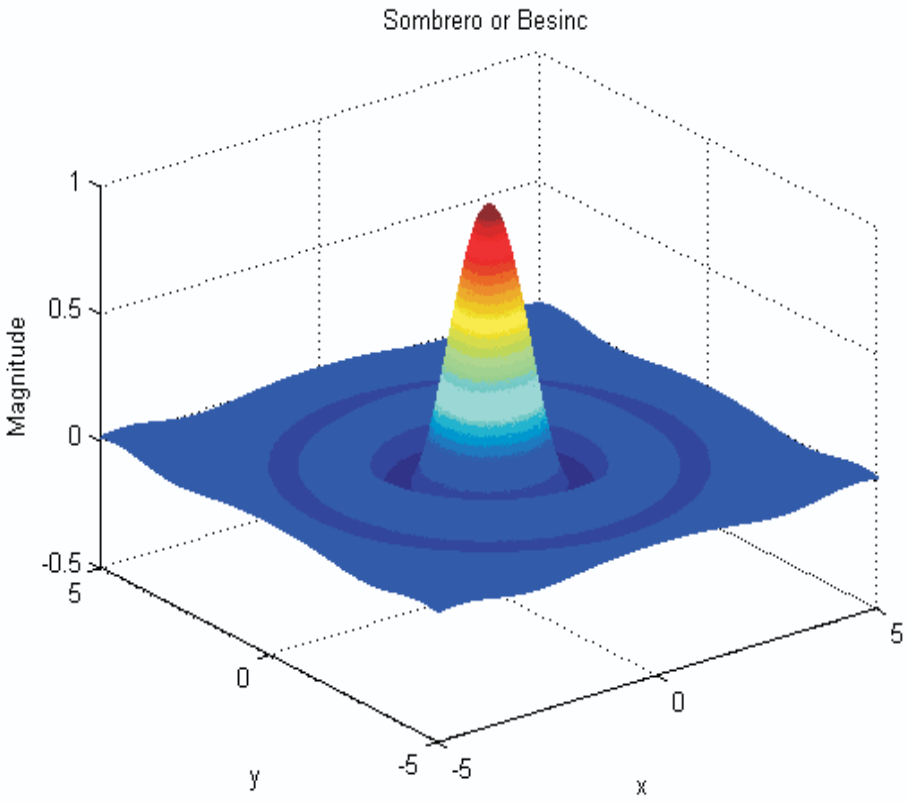

Figure 3.4. Sombrero or besinc point spread function.

called reconstruction by range stacking may be done to avoid it. SAR 2-D aperture synthesis is computationally efficient as it does not involve a numerically intensive Stolt interpolation. The spatial frequency domain for both range and cross-range is a direct mapping of the spatial frequency domain of the 2-D synthetic aperture (3.12).

2. As is evident from the block diagram in Fig. 3.2, after baseband conversion in the hardware, only 2-D FFT, scene-centered matched filtering based on platform altitude, and 2-D IFFT operations are needed for image formation. SAR digital signal processing for 2-D aperture synthesis is merely focusing the target area as per platform altitude, with the avionics providing the requisite height information U_z for this focusing.

3. A single frequency can be used for SAR imaging instead of wide bandwidth LFM or chirp. This laid the foundation for stand-alone passive SAR [2]. Fig. 3.5 shows slow-time or cross-range imaging for single and multiple point targets. As evident from the figure there is no information as to the point-target position along range or cross-track dimension. Therefore, this one-dimensional slow-time imaging needs to be supplemented by a fast-time imaging technique to clearly resolve the point-targets in both along-track and cross-track dimensions. On the other hand, Fig. 3.6 shows reconstructions for single and the multiple point-targets. Fig. 3.7 is the top view of multiple point-targets reconstruction shown in Fig. 3.6.

3.3 Fraunhofer and Fresnel Diffraction Patterns

SAR slow-time processing and imaging stands on the shoulders of giants as any other modern discipline. SAR signal processing is believed to bear a strong resemblance to Fourier array processing and imaging. However, SAR has benefited over the years from a lot of spin-offs resulting from extensive research in optics in general and Fourier optics in particular. Fourier optics-based analog SAR signal processing was used for image formation in Fresnel approximation-based algorithms. Some of the significant optics contributions to

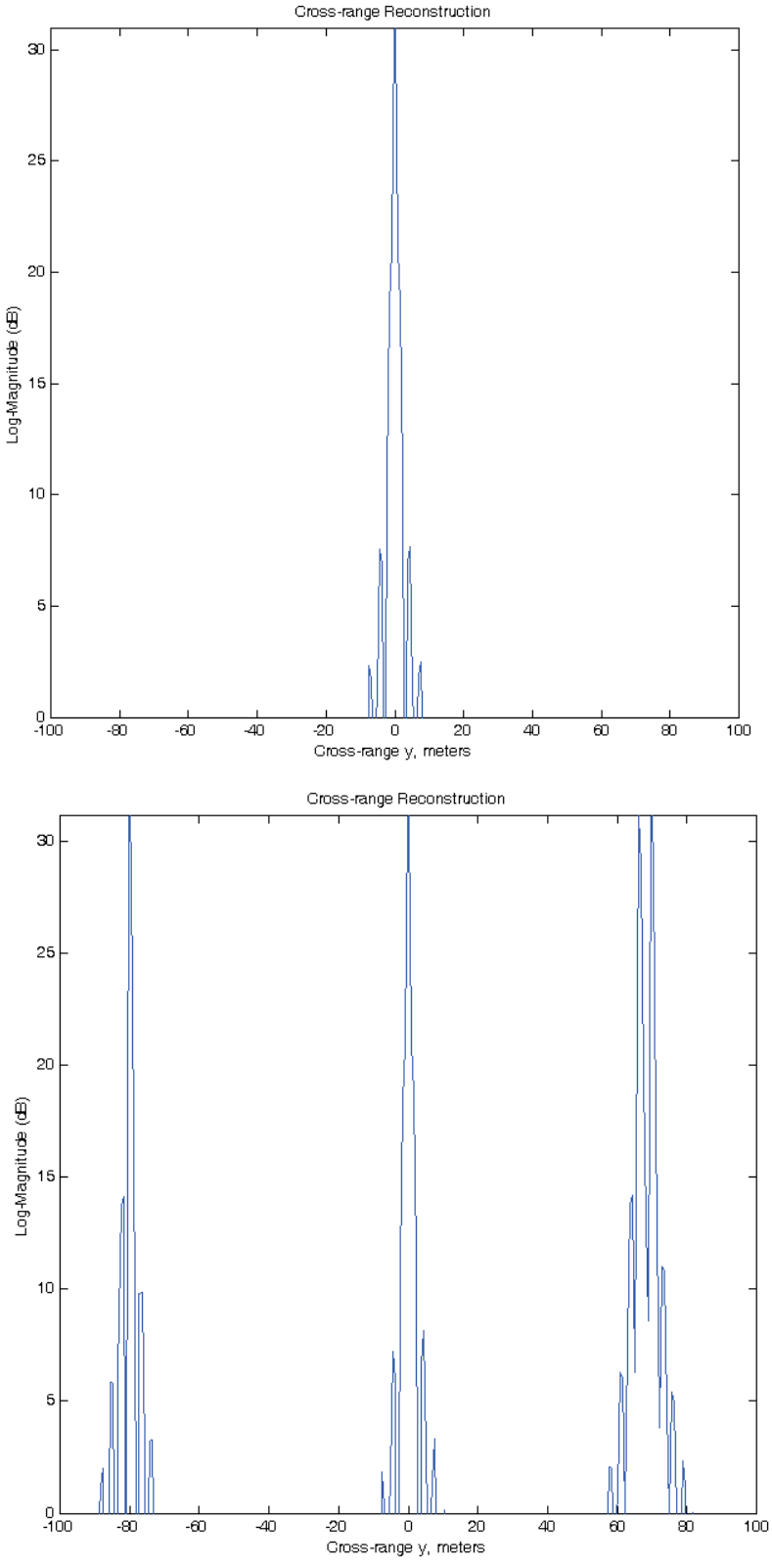

Figure 3.5. Slow-time or cross-range imaging for single and multiple point targets.

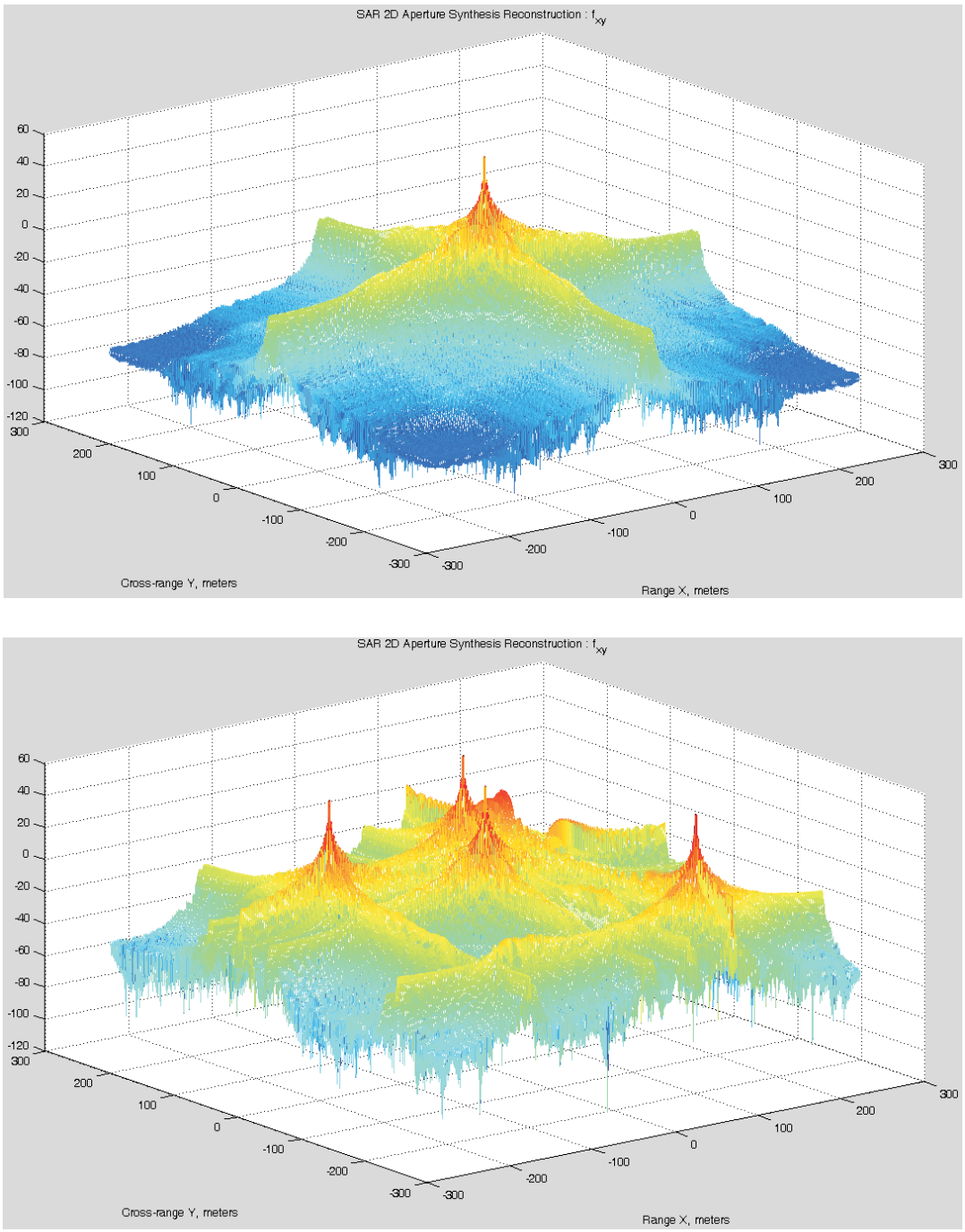

Figure 3.6. 2-D aperture synthesis based reconstruction for single and multiple point targets.

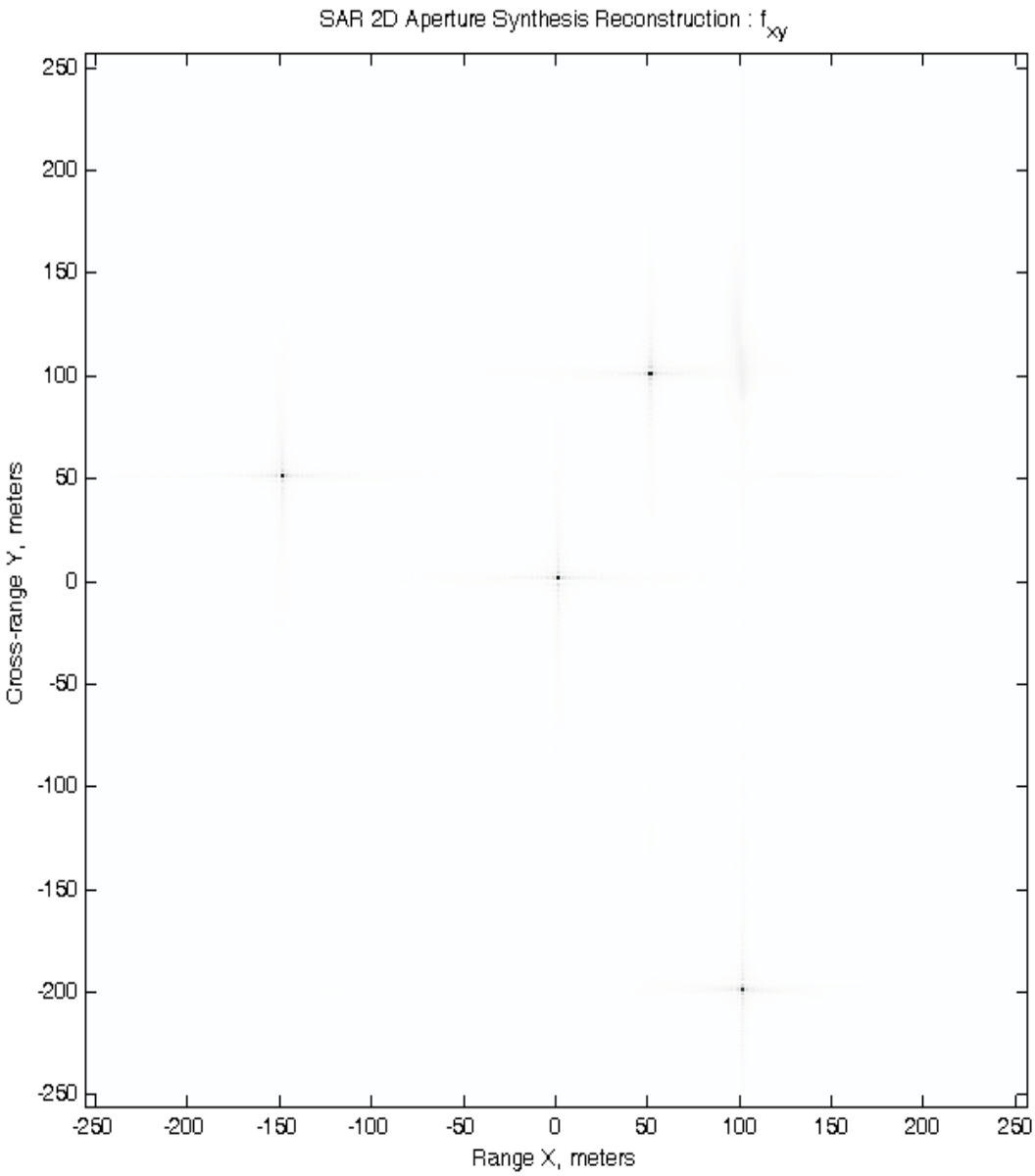

Figure 3.7. Top view of 2-D aperture synthesis based reconstruction for multiple point targets.

the SAR evolution are as follows:

1. Projection-slice theorem used in tomographic formulation of spot-light SAR imaging modality:

$$f(x,y) * *\Re_\theta(\delta(x)1(y)) \leftrightarrow F(u,v)\Re_\theta(1(u),\delta(v)) \tag{3.26}$$

2. Chirp-Z transform that works well for motion compensation or "mocomp" to a point concept in SAR signal processing:

$$((f(x)\exp^{-j\pi x^2}) * \exp^{j\pi x^2})\exp^{-j\pi x^2} = F(x) \tag{3.27}$$

$$((f(x)\exp^{j\pi x^2}) * \exp^{-j\pi x^2})\exp^{j\pi x^2} = \exp^{j\frac{\pi}{4}} F(x) \tag{3.28}$$

3. Fresnel transform, which is a convolution with quadratic phase factors:

$$\hat{f}_\alpha(x) = f(x) * \frac{1}{\sqrt{j\alpha}}\exp^{j\frac{\pi}{4}x^2} \tag{3.29}$$

Simulations with 2-D aperture synthesis has revealed the same Fraunhofer and Fresnel diffraction patterns as seen in Fourier optics [40], [41]. A comparison at this level has not been done earlier. This is because the underlying theoretical principle, namely, the Huygens-Fresnel principle combined with scalar diffraction theory, is commonly shared by SAR imaging and Fourier optics imaging. Therefore, the two imaging phenomena are mathematically analogous. The Huygens-Fresnel point spread function of SAR imaging is merely replaced by the complex amplitude transmittance function of Fourier optics as seen below:

$$s(x,y,d) = h(x,y) * *s(x,y,0) \qquad s(x,y,d) = t(x,y) * *s(x,y,0) \tag{3.30}$$

When an optical wave passes through an aperture, it is in general modified both in magnitude and phase. The complex amplitude transmittance is defined as the ratio of transmitted complex amplitude to incident complex amplitude $t(x,y) = \frac{U_{tran}(x,y)}{U_{inc}(x,y)}$. The complex transmittance function t(x,y) allows us to represent mathematically many commonly used apertures.

For example a square aperture of width w can be represented by $t(x, y) = rect(\frac{x}{w}, \frac{y}{w})$. In optics, the converging spherical wave illumination of an aperture produces, centered on the nominal point of convergence, a complex amplitude distribution proportional to the Fourier transform of the aperture transmittance function, scaled by the wavelength times the convergence distance. This result is one of the most important reached in the development of Fourier optics. It plays a central role in the theory of image formation by spherical lenses, and it also leads to many of the important signal processing applications of optical systems. SAR 2-D aperture synthesis-based imaging offers a unique opportunity to compare SAR signal processing with Fourier optics, as both employ 2-D spatial variables in the Euclidean space and exhibit Fraunhofer and Fresnel diffraction behavior [1].

3.3.1 Rectangular Aperture

The Fraunhofer diffraction pattern for rectangular aperture synthesis is shown in Fig. 3.8. The cylindrical Green's function is clearly seen in the simulated signal. Moreover, the Fourier domain support corresponds to the shape of the aperture. The reconstructed psf is 2-D sinc in this case. A 2-D sinc is mathmatically given by the product of sinc function along x axis times sinc function along y axis.

3.3.2 Circular Aperture

The Fraunhofer diffraction pattern for circular aperture synthesis is shown in Fig. 3.9, followed by Fresnel diffraction patterns in Fig. 3.10 generated by matched filtering with incorrect SAR height U_z. The psf in this case is sombrero or besinc (3.25).

Fig. 3.11 shows image reconstruction for multiple point targets using circular aperture and rectangular aperture and Fig. 3.12 is the top view of these reconstructions.

3.3.3 Optimality of Circular Aperture

It is pertinent to point out the optimality of circular aperture. Earlier, it was mentioned that the condition for 2-D asymptotic expansion is $\sqrt{k_x^2 - k_y^2} \leq 2k_\omega$ and zero otherwise, signifying a disc-shaped spatial Fourier domain support. As seen from the simulations

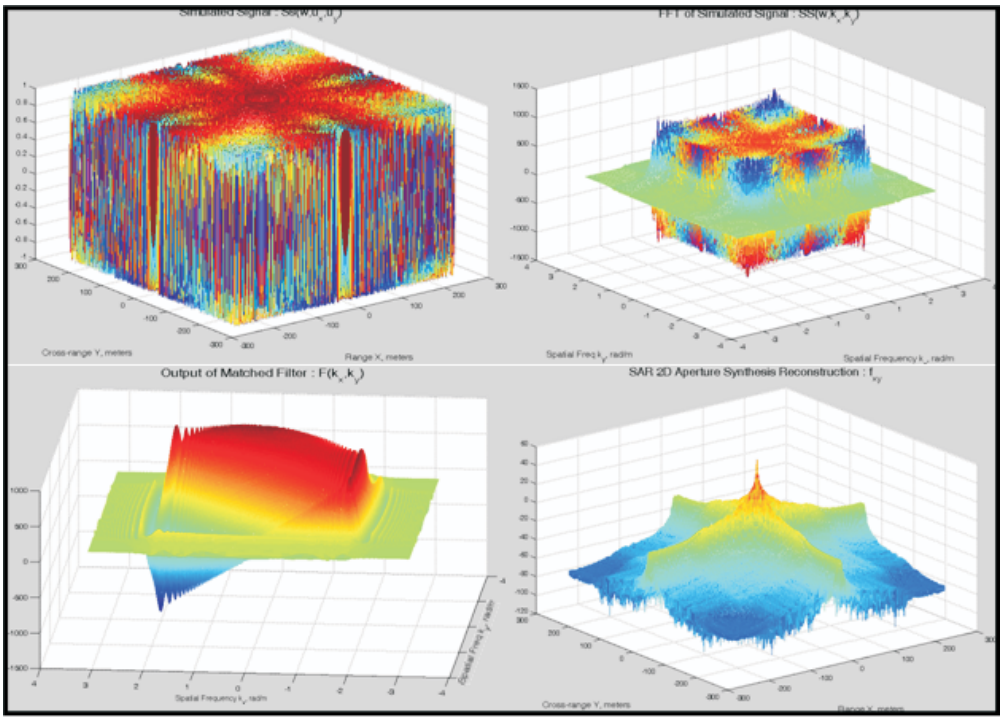

Figure 3.8. Fraunhofer diffraction pattern for rectangular aperture synthesis.

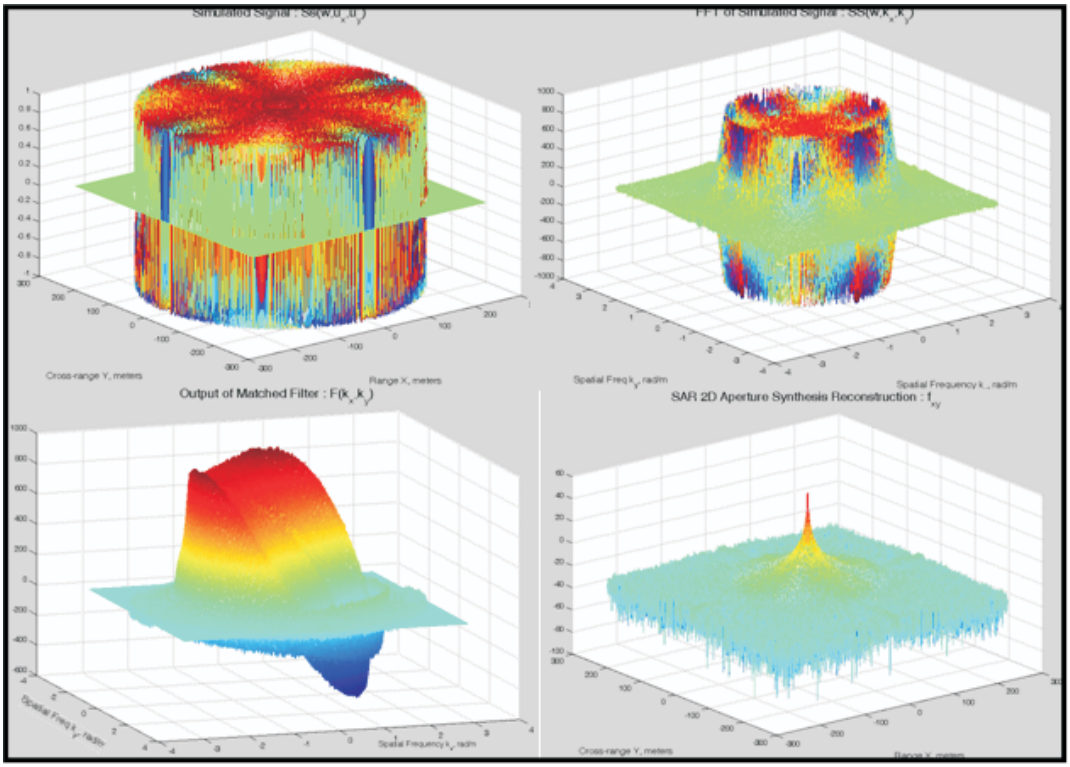

Figure 3.9. Fraunhofer diffraction pattern for circular aperture synthesis.

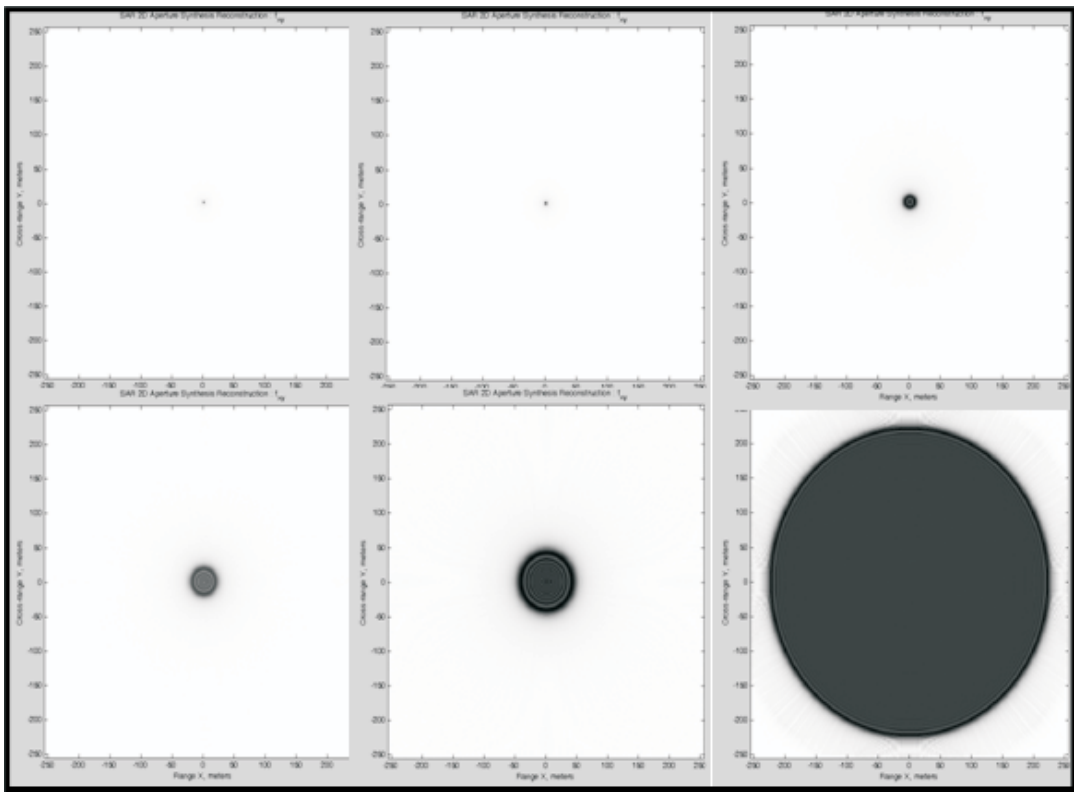

Figure 3.10. Fresnel diffraction pattern for circular aperture synthesis.

of 2-D aperture synthesis for circular aperture, the circular Fourier domain support fully utilizes all available Fourier support region. The same is not true for rectangular aperture as there are unfilled Fourier components in the allowable Fourier support region.

3.3.4 Ophthalmic Optics

The focusing in altitude interpretation of SAR 2-D aperture synthesis algorithm makes it an analogy of Fourier optics in general and ophthalmic optics in particular. The pupil of the human eye is a circular aperture for imaging at optical frequencies and the crystalline lens performs focusing by an accommodation mechanism that, according to Helmholtz theory, adjusts the power of the crystalline lens to allow objects to be in focus on the retina [42]. The difference of course is that the human eye is an incoherent sensor because of a multitude of cones and rods used for photo reception operating in the visible spectrum frequencies, whereas SAR is necessarily a coherent imaging system at radar frequencies. It

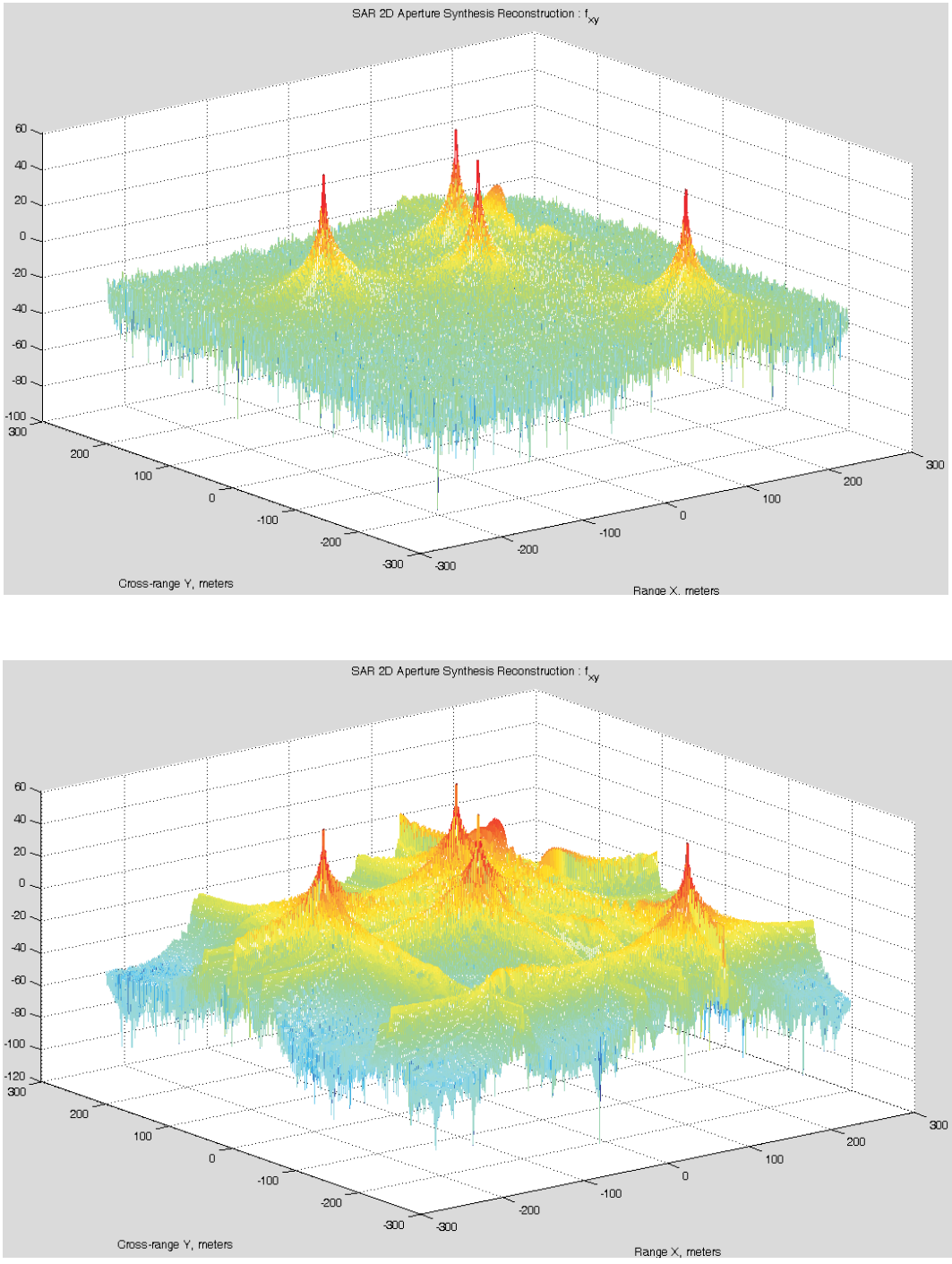

Figure 3.11. Multiple point-target reconstructions for (a) Circular aperture, (b) Rectangular aperture.

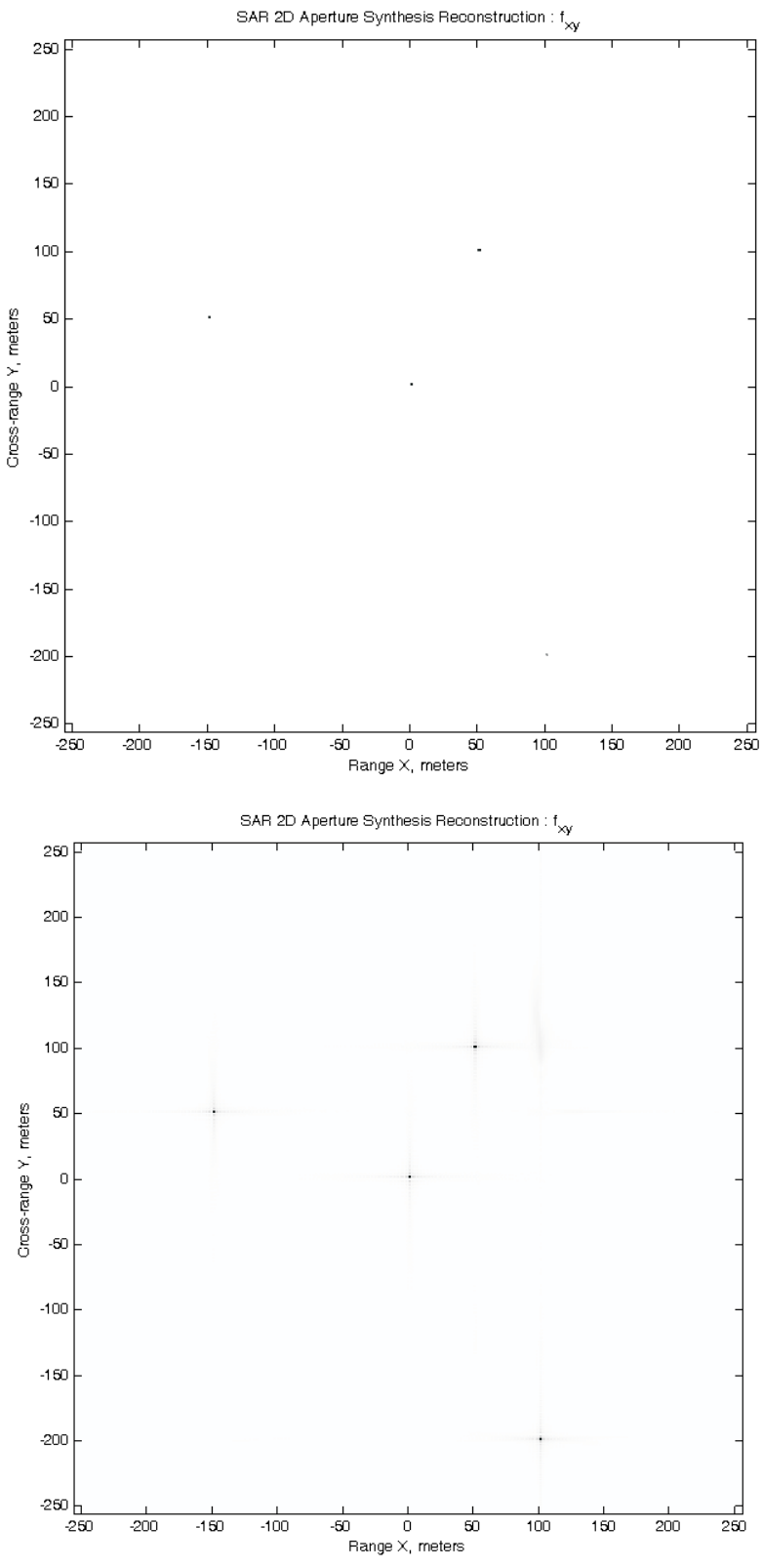

Figure 3.12. Top view of multiple point-target reconstructions for (a) Circular aperture, (b) Rectangular aperture.

is clear from our understanding of the analytical development of SAR 2-D aperture synthesis that the human eye is an optimum sensor as it fully utilizes mathematically allowable Fourier support region.

3.4 Data Collection for 2-D Aperture Synthesis

Various options for filling in Fourier components are explored next and summarized in Table 3.1. In all data collection schemes, SAR is assumed to be flyover.

3.4.1 Beam Raster-scanning Based Imaging

[3] Beam raster-scanning reaps the advancements in antenna beam pointing and scanning technology. Beam raster-scanning is by no means a new concept to radar engineering, as airborne pulse Doppler radars have been using it for a while. Airborne pulse Doppler radar has a narrow antenna beam width so that it can resolve two close airborne targets. Consequently, the narrow antenna beam is made to zig zag for greater spatial coverage during search mode. This type of scanning is commonly referred to as beam raster scanning. The data collection for beam raster-scanning SAR is depicted in Fig. 3.13 [3]. The drawback of scan-SAR imaging modality is that it employs beam scanning to extend the target range swath, thereby degrading azimuth resolution.

3.4.2 Multi-pass Imaging

In some applications, SAR makes multiple passes to image the target area. SAR multi-pass imaging is employed for *coherent change detection (CCD)* [43]. A large number of airborne flyovers would be required for 2-D aperture synthesis, undermining the feasibility of such a technique. However, multi-pass imaging would be feasible for the internal imaging of buildings termed as through-the-wall imaging or for mine detection applications where SAR may be mounted on rails.

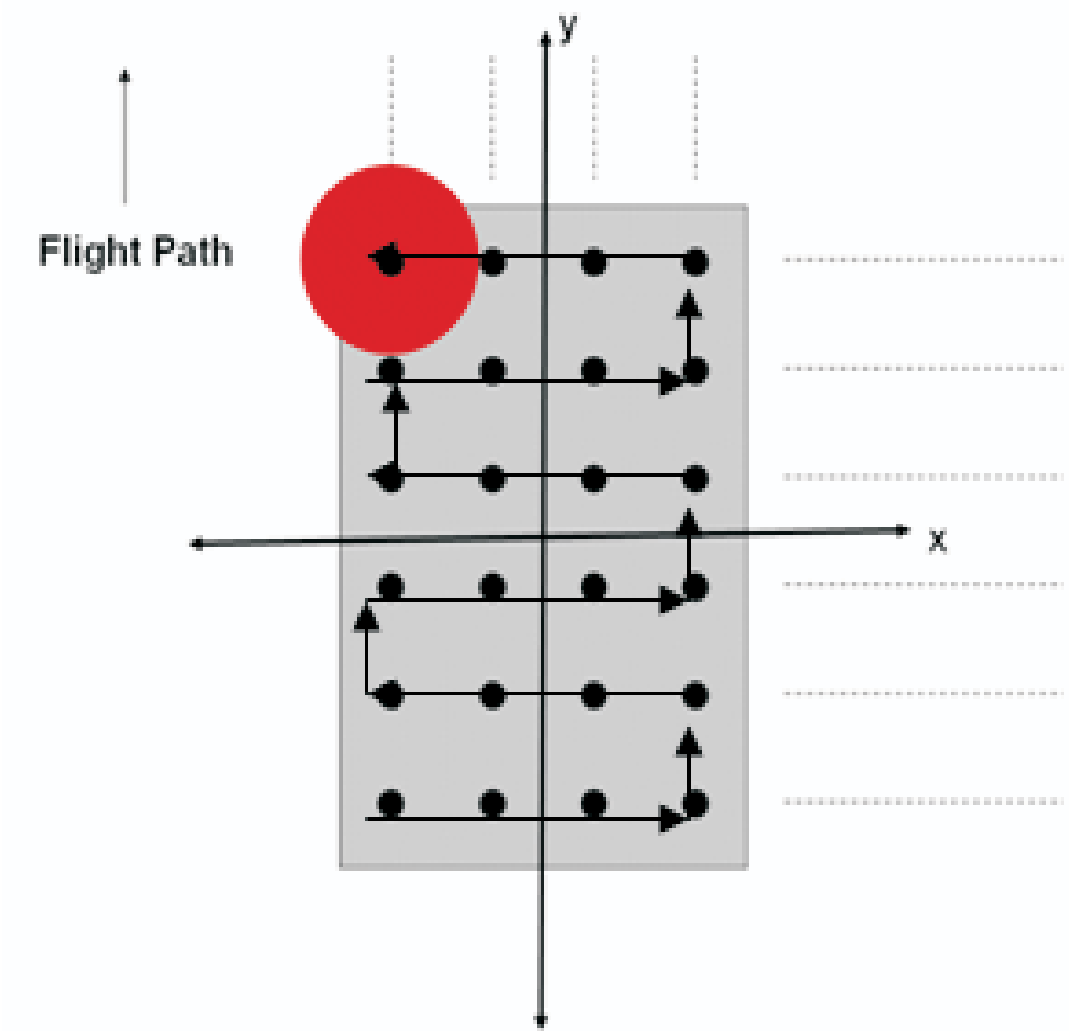

Figure 3.13. Beam raster-scan.

3.4.3 Sparse Array Imaging

Sparse arrays like the very large array (VLA) are used in radio astronomy [44]. The use of a sparse array would reduce the number of passes required for imaging. But sparse array does not qualify as a candidate for 2-D aperture synthesis in SAR imaging, as such an array involves observation time of several hours to fill in the Fourier components [45], as shown in Fig. 3.14.

3.4.4 Circular SAR Imaging

Linear SAR, in both stripmap and spotlight SAR modalities, measures the target SAR signature over a limited aspect angle of ±45°. Circular SAR is a method of imaging from the slant-plane data collected by synthetic aperture radar over the full 360° rotation or a partial segment of a circular flight path. Circular aperture is easily executed by a roll maneuver of airborne platform carrying SAR. The concept of circular SAR may also be extended to spaceborne SAR imaging, utilizing the motion of a satellite in an orbit accurately modeled as a circular trajectory. Following are the various techniques that employ slant-plane circular SAR imaging:

1. The first ever circular SAR processing was outlined using a plane wave approximation of the spherical wave function termed as range-Doppler imaging of rotating objects [46], [47].

2. Circular SAR may also be interpreted as a tomographic reconstruction problem and analyzed using the projection-slice theorem from computer-aided tomography. The signal recorded at each SAR transmission point is modeled as a portion of the Fourier transform of a central projection of the imaged ground area. Reconstruction of a SAR image may then be accomplished using traditional algorithms not based on Doppler shifts [48], [49], [50].

3. The Fourier analysis-based circular SAR approach is a recent development based on the Fourier decomposition of the multidimensional shift-varying impulse response or

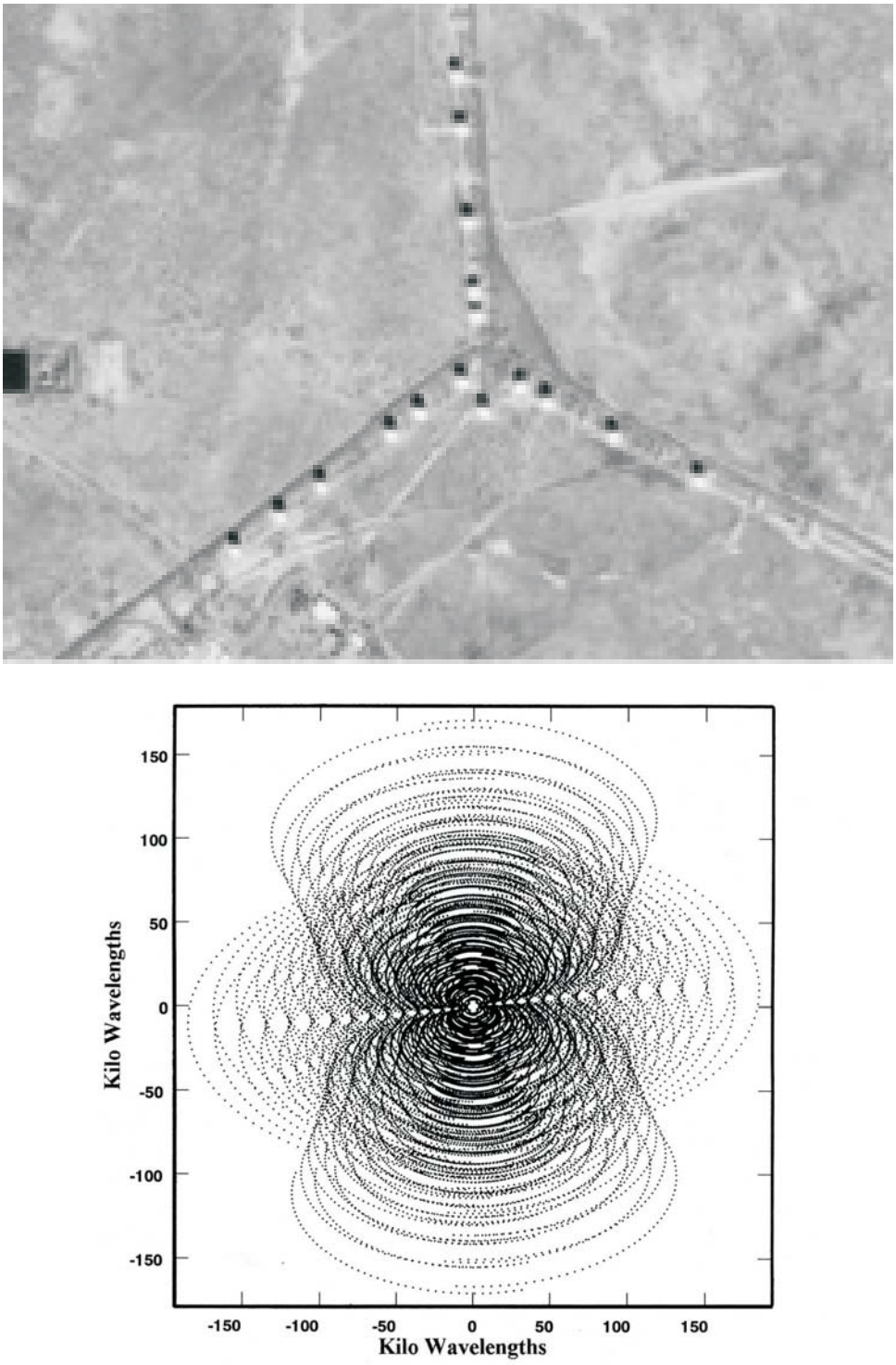

Figure 3.14. VLA and Fourier components for 8 hour tracking period.

Table 3.1. Data Collection Methodology.

Method	Remarks
Beam raster scanning	range resolution limited by beam width
Multi-pass imaging	feasibility undermined by large number of passes
Sparse arrays	unfilled Fourier components, inappropriate psf type
Circular aperture	mathematically optimal, ease of execution by roll manoeuvre

slant-plane Green's function. This type of circular SAR computes the ground-plane circular SAR from the slant-plane circular SAR data for further matched filtering-based target area reconstruction. An approximation to ground-plane circular SAR is achieved by taking the hermitian transpose of the near-orthogonal system model. Mathematically, the pseudo-inverse of the linear shift-varying system needs to be computed [51], [8], [52].

4. The back-projection circular SAR algorithm correlates measured circular SAR data with the analytical signature of a unit reflector at each pixel point on the desired spatial reconstruction grid to form the circular SAR image of the target area.

CHAPTER 4

FAST CIRCULAR SAR (CSAR) IMAGING [4], [5]

Fourier analysis-based CSAR imaging involves multidimensional aperture synthesis supplemented by fast-time imaging techniques to fill in Fourier components. This investigation in computationally efficient CSAR methods is a sequel to prior research on multidimensional aperture synthesis [1], [27], [29], [28], [32]. A required condition for an asymptotic expansion of a two-dimensional aperture synthesis was earlier investigated that defined a circular support region in the Fourier domain [2], [26], [31]. It has been shown that a circular synthetic aperture is easily executed by a roll maneuver of an airborne platform carrying a SAR sensor. This is in contrast to challenges in creating alternate aperture shapes encountered both in Fourier optics and array processing [40], [42], [44]. Our study of the Fourier optics discipline revealed results that are equally applicable to SAR imaging, mainly that the psf is merely a Fourier transform of the aperture shape. Moreover, sparse array shapes like the Very Large Array (VLA) in radio astronomy do not qualify as candidates for 2-D aperture synthesis in SAR imaging because such arrays involve observation time of several hours to fill in Fourier components [45].

Linear SAR, in both stripmap and spotlight SAR modalities, typically measures target SAR signature only over a limited aspect angle. CSAR, on the other hand, is a method of imaging SAR capable of obtaining measurements of up to a full 360° rotation or a partial segment of a circular flight path. The concept of CSAR may also be extended to spaceborne SAR imaging utilizing the motion of a satellite in an orbit accurately modeled as a circular trajectory [52]. Following are the various techniques that employ slant-plane CSAR imaging:

1. The first ever CSAR processing was outlined using a plane wave approximation of the spherical wave function, and was called the range-Doppler imaging of rotating objects [46], [47], [13]. The resultant Polar Format Algorithm (PFA) was later used

for the spotlight imaging modality of SAR shown in Fig. 4.1.

2. CSAR may also be interpreted as a tomographic reconstruction problem and analyzed using the projection-slice theorem from computer-aided tomography

$$f(x,y) * *\Re_\theta[\delta(x)1(y)] \leftrightarrow F(u,v)\Re_\theta[1(u)\delta(v)] \tag{4.1}$$

The signal recorded at each SAR transmission point is modeled as a portion of the Fourier transform of a central projection of the imaged ground area. Reconstruction of a SAR image may then be accomplished using traditional algorithms not based on Doppler shifts [48].

3. The approximation free, Fourier analysis based CSAR approach is a recent development based on a Fourier decomposition of the multidimensional shift-varying impulse response or the slant-plane Green's function as shown in Fig. 4.2. This type of CSAR computes ground-plane CSAR from a projection of the slant-plane CSAR phase history data into a ground-plane phase history for further matched filtering-based target area reconstruction. An approximation to ground-plane CSAR is achieved by taking the hermitian transpose of the near-orthogonal system slant-plane-to-ground plane phase history projection model. The alternate approach involves a computationally expensive pseudo-inverse of the linear shift-varying system [51], [8].

4. The back-projection CSAR algorithm correlates measured CSAR data with the analytical signature of a unit reflector at each pixel point on the desired spatial reconstruction grid to form the CSAR image of the target area [8].

Householder transform-based processing has recently been shown to have improved error bounds and stability as an underdetermined system solver [53]. This transform may also be applied to ill-conditioned systems with speed unmatched by any other solver [54], [55], [56], [57]. This research proposes the use of the Householder transform to process

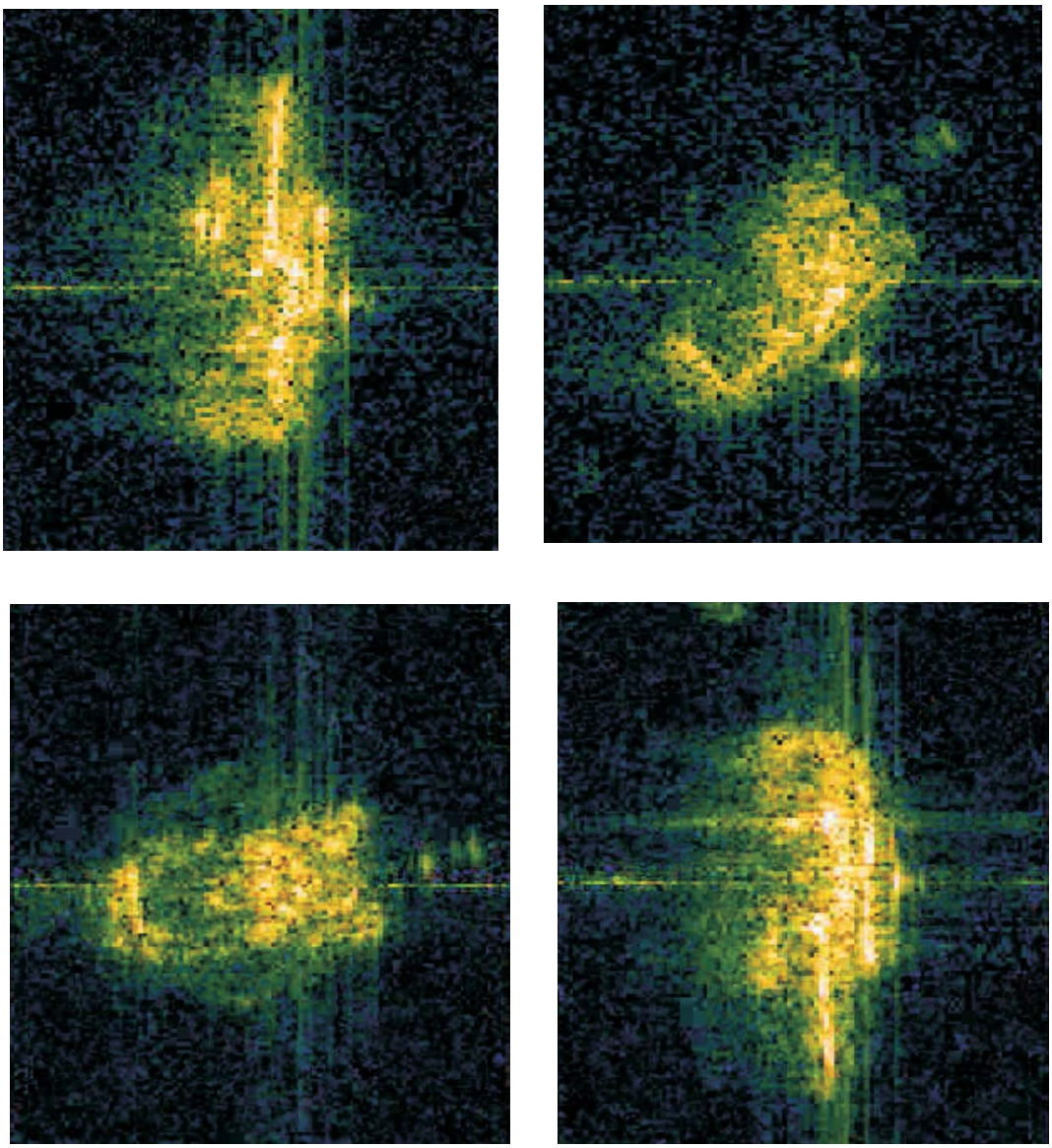

Figure 4.1. T-72 target mapping using Polar Format Algorithm (PFA) [8].

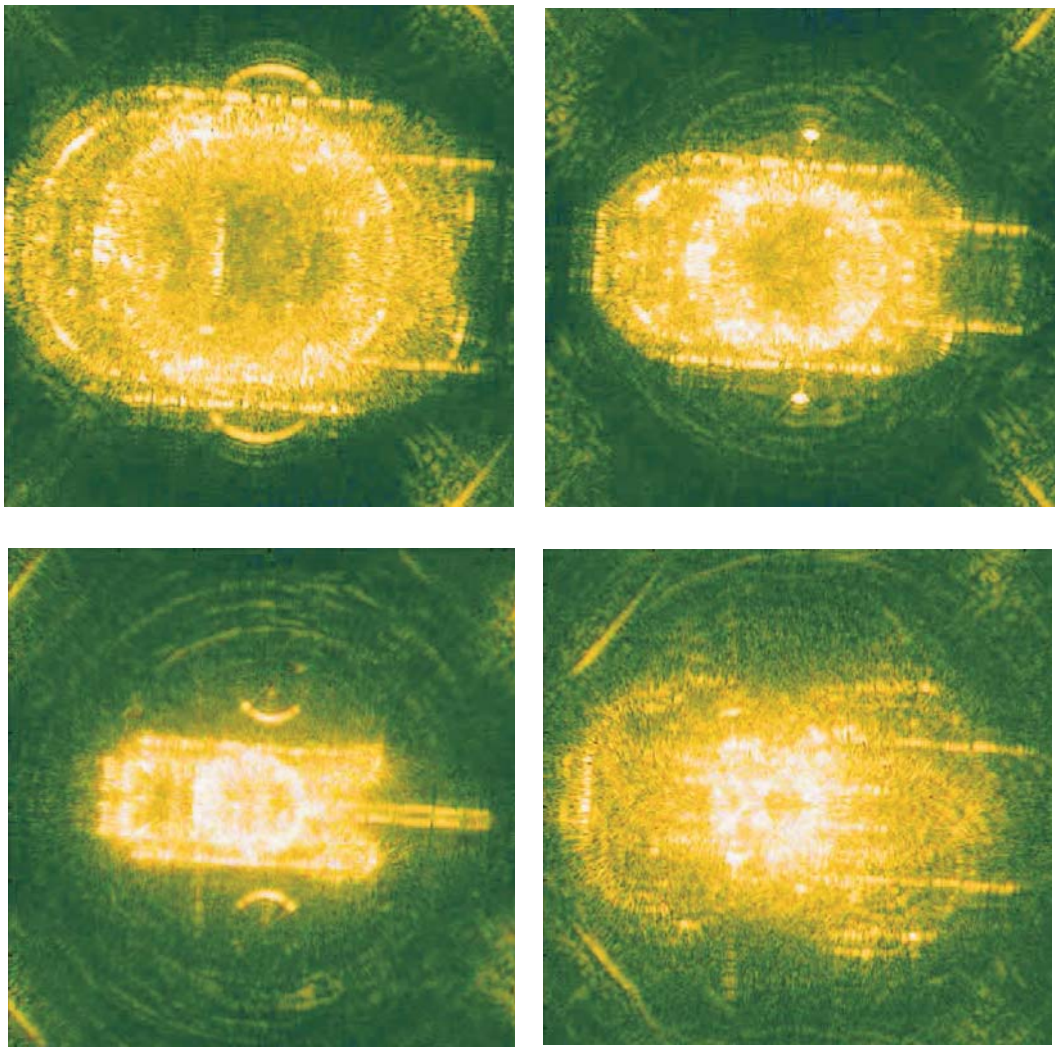

Figure 4.2. T-72 target mapping using Circular SAR (CSAR) Algorithm [8].

Fourier analysis based CSAR data, thus circumventing the need for explicitly computing a pseudo-inverse in CSAR imaging.

4.1 Measurement Model

The top and side views of the imaging system geometry are shown in Fig. 4.3. The radar carrying aircraft moves along a circular flight path with radius R on the plane $z = z_o$ with respect to the ground-plane. The coordinates of the radar in the spatial domain as a function of the slow-time are $(x, y, z) = (R\cos\theta, R\sin\theta, z_o)$, where $\theta \in [-\pi, \pi)$ represents the slow-time domain. As the SAR traverses a circular flight path the radar beam remains spotlighted on a disk of radius X_o; denoted as $D : X_o$, centered at the origin of the spatial (x, y) domain on the ground plane. This $(x, y) \in D : X_o$ and zero otherwise is also called target region's support. The reflectivity function in the target region is denoted by $f(x, y)$. The slant-range R_o, slant-angle θ_z and *along-track* target-angle are defined as:

$$R_o \equiv \sqrt{R^2 + z_o^2} \tag{4.2}$$

$$\theta_z \equiv \tan^{-1}(\frac{z_o}{R}) \tag{4.3}$$

$$\pm\theta_x \equiv \sin^{-1}(\frac{\pm X_o}{R}) \tag{4.4}$$

The along-track target-angle θ_x is defined here for a planar radar aperture and is a decreasing function of fast-time frequency.

4.2 CSAR Mathematical Development

Assuming a transmitted signal $p(t)$ and speed of light c, the measured SAR signal in the slow-time and fast-time domains (θ, t) may be defined as follows:

$$t_\theta = \frac{2\sqrt{(x - R\cos\theta)^2 + (y - R\sin\theta)^2 + z_o^2}}{c} \tag{4.5}$$

$$s(\theta, t) = \int\int f(x, y)p[t - t_\theta]dxdy \tag{4.6}$$

After applying a Fourier transform with respect to fast-time t and matched filtering, we

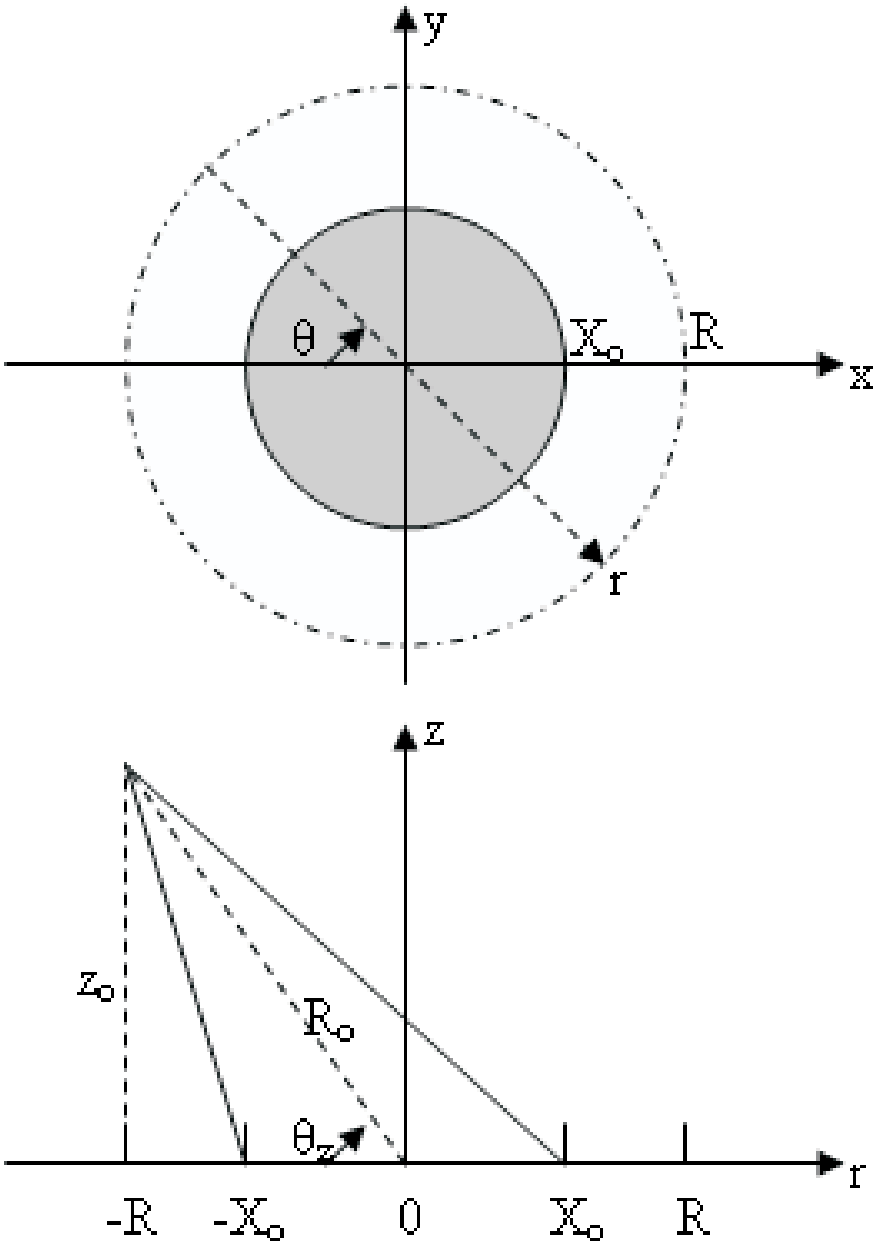

Figure 4.3. CSAR imaging geometry.

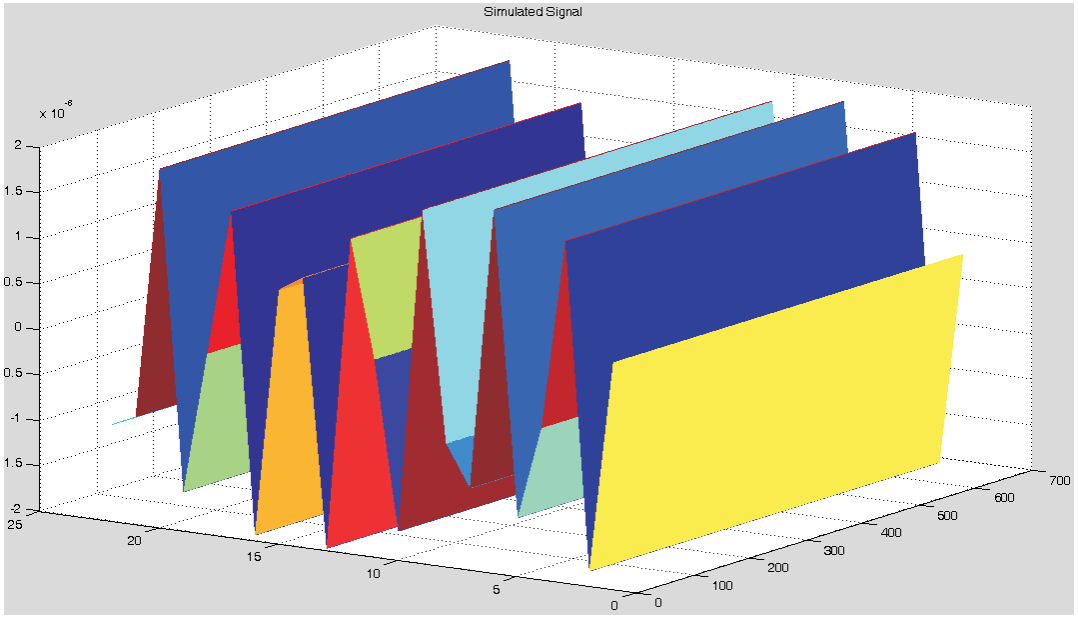

Figure 4.4. CSAR simulated signal $s(\theta, t)$ for point target at center of target area.

obtain

$$s(\theta, \omega) = \int \int f(x, y) g_\theta(x, y, \omega) dx dy \tag{4.7}$$

where the CSAR imaging system's shift varying impulse response $g_\theta(x, y, \omega)$ also called the slant-plane Green's function for slow-time angle θ and fast-time frequency ω, is defined for wavenumber $k = \frac{\omega}{c}$ as

$$g_\theta(x, y, \omega) \equiv \exp[-j2k \sqrt{(x - R\cos\theta)^2 + (y - R\sin\theta)^2 + z_o^2}] \tag{4.8}$$

for $(x, y) \in D : X_o$, and zero otherwise. For notational simplicity, the radar signal's Fourier transform $P(\omega)$, which appears on the right side of equation (4.7), is ignored in subsequent discussion. CSAR image formation processing is based on linear shift-varying system theory. So instead of being able to use convolution integrals, one may use a generalized Parseval's theorem.

4.2.1 Slant-plane CSAR Green's Function

In order to obtain the spatial Fourier transform of slant-plane Green's function we first rewrite equation (4.8) for $\theta = 0$ as

$$g_0(x, y, \omega) \equiv \exp[-j2k\sqrt{(x - R)^2 + y^2 + z_o^2}] \tag{4.9}$$

It is evident from equation (4.9) that the Green's function for $\theta = 0$ is shifted (in $x-$dimension by R) and space-limited (to $D : X_o$) form of

$$h(x, y, \omega) \equiv \exp[-j2k\sqrt{x^2 + y^2 + z_o^2}] \tag{4.10}$$

The 2-D signal in equation (4.10) is a circularly symmetric function in the spatial (x, y) domain. Thus, it can be expressed via the following:

$$h(x, y, \omega) \equiv h_p(r) \tag{4.11}$$

where

$$h_p(r) \equiv \exp[-j2k\sqrt{r^2 + z_o^2}] \tag{4.12}$$

with $r = \sqrt{x^2 + y^2}$.

The 2-D spatial Fourier transform of the signal $h(x, y, \omega)$ is also a circularly symmetric function that may be written as

$$h(k_x, k_y, \omega) \equiv H_p(\rho) \tag{4.13}$$

where

$$H_p(\rho) \equiv \int r h_p(r) H_0(\rho r) dr \tag{4.14}$$

and $H_0(\rho r)$ is a Hankel function.

Substituting $h_p(r)$ in the above equation yields

$$H_p(\rho) = \int r \exp(-j2k\sqrt{r^2 + z_o^2}) H_0(\rho r) dr \tag{4.15}$$

which can be evaluated to produce

$$H_p(\rho) = exp(-j\sqrt{(2k)^2 - \rho^2} z_o) \tag{4.16}$$

with $\rho \equiv \sqrt{k_x^2 + k_y^2}$

Consider $g_0(x, y, \omega)$, shifted in $x-$dimension

$$g_0(x, y, \omega) = h(x - R, y, \omega) \tag{4.17}$$

where the right hand side is the Green's function. Then the spatial Fourier transform of the Green's function at $\theta = 0$ is

$$G_0(k_x, k_y, \omega) = H(k_x, k_y, \omega) \exp(-jk_x R) \tag{4.18}$$

or

$$G_0(k_x, k_y, \omega) = H_\rho(\rho) \exp(-jk_x R) \tag{4.19}$$

We may also rewrite the above equation as

$$G_0(k_x, k_y, \omega) = \exp(-j\sqrt{4k^2 - \rho^2} z_o - jk_x R) \tag{4.20}$$

It is also known that $g_0(x, y, \omega)$, besides being shifted version of free space Green's function $h(x - R, y, \omega)$, is also a space-limited or *windowed* version of Green's function. Since the free space Green's function is also a phase-modulated (PM) signal, using the properties of PM signals we can write the following equation:

$$G_0(k_x, k_y, \omega) = W_0(k_x, k_y, \omega) \exp(-j\sqrt{4k^2 - \rho^2} z_o - jk_x R) \tag{4.21}$$

where $W_0(k_x, k_y, \omega)$ is a window in the spatial-frequency domain corresponding to the window in the spatial domain.

We can also write the phase function as

$$\gamma(x, y, \omega) \equiv 2k\sqrt{(x - R)^2 + y^2 + z_o^2} \tag{4.22}$$

In order to compute window $W_0(k_x, k_y, \omega)$ we need to determine the first partial derivatives of the above mentioned phase function

$$k_x(x, y, \omega) \equiv \frac{\partial \gamma}{\partial x} \tag{4.23}$$

which is obtained as

$$k_x(x, y, \omega) = 2k\frac{x - R}{\sqrt{(x - R)^2 + y^2 + z_o^2}} \tag{4.24}$$

Similarly,

$$k_y(x, y, \omega) \equiv \frac{\partial \gamma}{\partial y} \tag{4.25}$$

is obtained as

$$k_y(x, y, \omega) = 2k\frac{y}{\sqrt{(x - R)^2 + y^2 + z_o^2}} \tag{4.26}$$

The spatial-frequency support band of the Green's function $G_0(k_x, k_y, \omega)$ or $W_0(k_x, k_y, \omega)$ is dictated by the set

$$(k_x, k_y) \in \left[\left(\frac{\partial \gamma}{\partial x}, \frac{\partial \gamma}{\partial y}\right); (x, y) \in \textit{target area}\right] \tag{4.27}$$

As pointed out earlier the target area is limited to the disk of radius X_0 such that $D : X_0$, in the spatial (x,y) domain. Let

$$\phi \equiv \tan^{-1}\frac{k_y}{k_x} \tag{4.28}$$

then the polar spatial-frequency domain (ϕ, ρ) of the Green's function $G_0(k_x, k_y, \omega)$ or $W_0(k_x, k_y, \omega)$ may approximately be written as

$$|\rho - 2k\cos\theta_z| \leq 2k\sin^2\theta_z \sin\theta_x \tag{4.29}$$

$$|\phi| \leq \theta_x \tag{4.30}$$

Thus, in the polar spatial frequency domain (ϕ, ρ), the window function W_0 may be written as

$$W_{0p}(\phi, \rho, \omega) = \begin{cases} 1, & |\rho - 2k\cos\theta_z| \leq 2k\sin^2\theta_z \sin\theta_x \text{ and } |\phi| \leq \theta_x; \\ 0, & \text{otherwise.} \end{cases} \tag{4.31}$$

The window function $W_{0p}(\phi, \rho, \omega)$ can easily be rewritten as a product of two 1-D functions as

$$W_{0p}(\phi, \rho, \omega) = W_1(\phi)W_2(\rho, \omega) \tag{4.32}$$

where

$$W_1(\phi) \equiv \begin{cases} 1, & |\phi| \leq \theta_x; \\ 0, & \text{otherwise.} \end{cases} \tag{4.33}$$

and

$$W_2(\rho, \omega) \equiv \begin{cases} 1, & |\rho - 2k\cos\theta_z| \leq 2k\sin^2\theta_z \sin\theta_x; \\ 0, & \text{otherwise.} \end{cases} \tag{4.34}$$

We know that $g_\theta(x, y, \omega)$ is the $\theta-$rotated version of $g_0(x, y, \omega)$ in the spatial (x, y) domain. Thus, $G_\theta(k_x, k_y, \omega)$ is also the $\theta-$rotated version of $G_0(k_x, k_y, \omega)$ in the spatial-frequency (k_x, k_y) domain. Therefore, we can use the Fourier transform properties to write the Fourier transform of equation (4.8) as

$$G_\theta(k_x, k_y, \omega) = W_\theta(k_x, k_y, \omega).\exp\left[-j\sqrt{4k^2 - \rho^2}z_o - j(k_x\cos\theta + k_y\sin\theta)R\right] \tag{4.35}$$

which simplifies to

$$G_\theta(k_x, k_y, \omega) = W_\theta(k_x, k_y, \omega)\exp\left[-j\sqrt{4k^2 - \rho^2}z_o - j\rho R\cos(\theta - \phi)\right] \tag{4.36}$$

where $W_\theta(k_x, k_y, \omega)$ is the $\theta-$rotated version of $W_0(k_x, k_y, \omega)$ in the spatial-frequency (k_x, k_y) domain. Using equations (4.32), (4.33) and (4.34) the window function W_θ can be rewritten in the polar frequency domain as follows:

$$W_{\theta p}(\phi, \rho, \omega) = \begin{cases} 1, & \text{for } |\rho - 2k\cos\theta_z| \leq 2k\sin^2\theta_z \sin\theta_x \text{ and } |\phi - \theta| \leq \theta_x; \\ 0, & \text{otherwise.} \end{cases} \tag{4.37}$$

Since $W_{\theta p}(\phi, \rho, \omega)$ is the $\theta-$shifted version of $W_{0p}(\phi, \rho, \omega)$ in the $\phi-$domain, we can write

$$W_{\theta p}(\phi, \rho, \omega) = W_{0p}(\phi - \theta, \rho, \omega) \tag{4.38}$$

or

$$W_{\theta p}(\phi, \rho, \omega) = W_{0p}(\theta - \phi, \rho, \omega) \tag{4.39}$$

Finally,

$$W_{\theta p}(\phi, \rho, \omega) = W_1(\theta - \phi) W_2(\rho, \omega) \tag{4.40}$$

The Green's function $G_\theta(k_x, k_y, \omega)$ has a spatial-frequency spread around the circle of radius $\rho = 2k \cos\theta_z$. For the ground-plane case of slant angle $\theta_z = 0$, the only existing waves are evanescent in nature and have no significance to SAR imaging. For slant-angle $\theta_z > 0$ we can write the corresponding resolutions from equation (4.29), (4.30) as follows:

$$\Delta_\rho \equiv \pm 2k \sin^2\theta_z \sin\theta_x \tag{4.41}$$

$$\Delta_\phi \equiv \pm\theta_x \tag{4.42}$$

4.2.2 Slant-plane CSAR Inversion

Next, we utilize the Fourier properties of the slant-plane Green's function to develop an analytical solution for CSAR reconstruction. Consider the CSAR signal model in the ω, θ domain

$$s(\omega, \theta) = \int\int f(x, y) g^*_\theta(x, y, \omega) dx dy \tag{4.43}$$

Using the generalized Parseval's theorem, this CSAR system model can be rewritten via

$$s(\omega, \theta) = \int\int F(-k_x, -k_y) G^*_\theta(k_x, k_y, \omega) dk_x dk_y \tag{4.44}$$

For notational simplicity, we can replace $F(-k_x, -k_y)$ by $F(k_x, k_y)$, which results in a rotation of the target function by π. Making variable transformations from the rectilinear spatial frequency (k_x, k_y) domain to the polar spatial frequency (π, ρ) domain in equation (4.44) we get

$$s(\omega, \theta) = \int\int \rho F_p(\rho, \phi) G^*_{\theta p}(\rho, \phi, \omega) d\rho d\phi \tag{4.45}$$

where the subscript p denotes polar spatial coordinates.

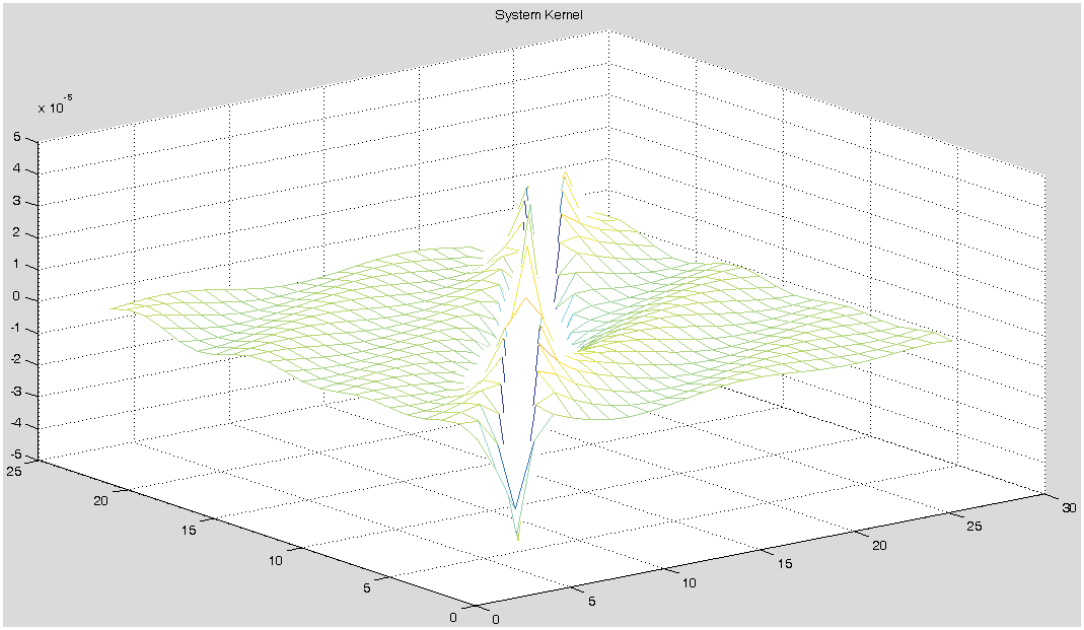

Figure 4.5. System kernel $\Lambda(\omega, \omega_g)$ (real part).

Using the analytical expression for the slant-plane Green's function in the above model yields

$$s(\omega,\theta) = \int\int \rho F_p(\rho,\phi) W_1(\theta-\phi) W_2(\rho,\omega) \exp\left[-j\sqrt{4k^2-\rho^2}z_o - j\rho R\cos(\theta-\phi)\right] d\rho d\phi \tag{4.46}$$

Finally, the system model is written as [51], [8]

$$s(\theta,\omega) = \int \Lambda(\omega,\omega_g)\Gamma(\theta,\rho) d\rho \tag{4.47}$$

where

$$\Lambda(\omega,\omega_g) \equiv W_2(\rho,\omega)\exp(-j\sqrt{4k^2-\rho^2}z_o) \tag{4.48}$$

The function $\Lambda(\omega, \omega_g)$, called the system kernel, is a 2-D windowed phase modulated signal in the ω spatial domain as depicted in Fig. 4.5.

Also

$$\Gamma(\theta,\rho) \equiv \rho \int F_p(\phi,\rho) W_1(\theta-\phi)\exp\left[-j\rho R\cos(\theta-\phi)\right] d\phi \tag{4.49}$$

In discrete form, this system model may also be expressed as linear model

$$S_\theta = \Lambda\Gamma_\theta \tag{4.50}$$

where Γ_θ is the discrete version of $s_g(\theta, \omega_g)$. The inverse of this linear model provides means for computing the ground-plane CSAR phase history Γ_θ from slant-plane CSAR signal-space phase history S_θ. Hence, the inverse of the system kernel Λ^{-1} may be written as

$$\Gamma_\theta = \Lambda^{-1} S_\theta \tag{4.51}$$

An approximate method for solving the above linear system transfer function assumes Λ to be near-orthogonal, hence the inverse is approximated by the hermitian transpose

$$\Lambda^{-1} \approx \Lambda^H \tag{4.52}$$

A Fourier domain CSAR image formation algorithm requires formation of the ground-plane CSAR signal phase history Γ_θ to obtain the target function's phase history. The relationship between the slant-plane CSAR signal-space phase history $S_\theta = s(\theta, \omega)$ and the ground plane CSAR signal phase history $s_g(\theta, \omega_g)$ as a linear shift-varying filter is shown in Fig. 4.6. In the digital implementation of a Fourier based CSAR image formation algorithm, the inverse system kernel $\Lambda^{-1}(\omega_g, \omega)$ as depicted in Fig. 4.7 is computed numerically via the pseudo-inverse of the system kernel. Subsequently presented work utilizes a Householder transform to compute the ground-plane CSAR phase history from the slant-plane CSAR phase history, as will be described in the following sections.

$$\Lambda\Gamma_\theta = S_\theta \quad \textit{then} \quad \Gamma_\theta = \Lambda^\dagger S_\theta \tag{4.53}$$

4.3 Underdetermined Behavior

The detailed analysis of $\Lambda \in C^{m \times n}$ dense matrix in equation (4.50) revealed the underdetermined nature of this system of equations. The inequality $m < n$ was predominantly true in the entire operating regimen of CSAR. The five variables that contribute to the dimensions of this matrix are the carrier frequency f_c, signal bandwidth f_0, radius of target area X_0,

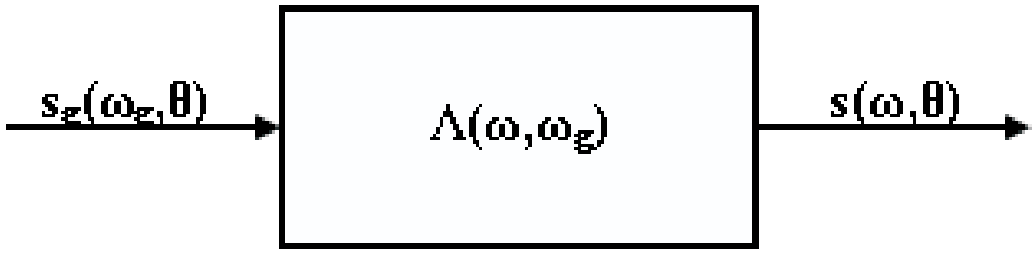

Figure 4.6. Block diagram of linear shift-varying system for generating slant-plane CSAR signal from ground-plane CSAR signal.

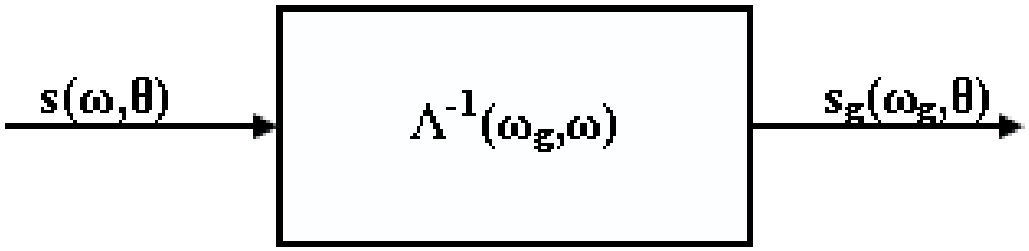

Figure 4.7. Block diagram of inverse linear shift-varying system for generating ground-plane CSAR signal from slant-plane CSAR signal.

slant range to the center of target area R_0, and elevation angle θ_z. These five parameters were varied and the difference between number of columns and number of rows $n - m$ was plotted in Fig. 4.8.

1. The carrier frequency f_c was varied from 0.5 to 20.5 GHz. The system model was underdetermined for the entire range of f_c as $n - m > 0$. Moreover, m was constant and n increased linearly resulting in $n - m$ also increasing linearly with increase in f_c.

2. The signal bandwidth f_0 was varied from 100 to 600 MHz. The system model was underdetermined for the entire range of f_0 as $n - m > 0$. Additionally, both n and m increased linearly and the difference $n - m$ remained constant with increasing f_0.

3. The radius of target area X_0 was increased from 5 to 105 m. The system model was underdetermined for the entire range of practical values of X_0 as $n - m > 0$. It was observed that the size of Λ matrix and difference $n-m$ rapidly increased with increase

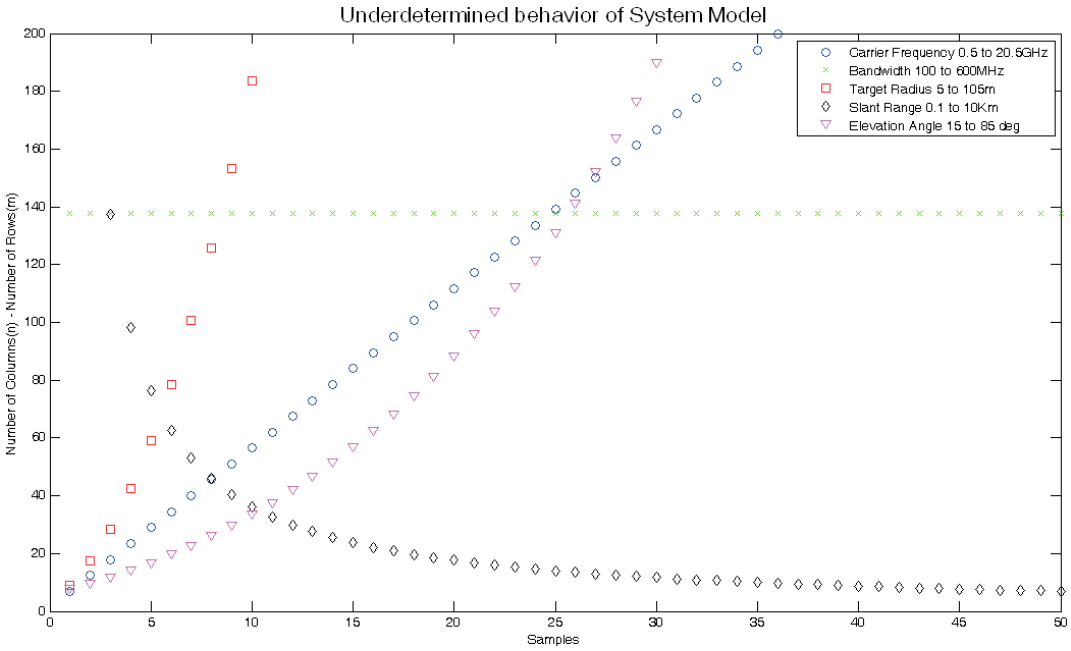

Figure 4.8. Underdetermined behavior of system model.

in X_0.

4. The slant-range to the center of target area R_0 was varied from 0.1 to 10 Km. The system model was again underdetermined for the entire range of practical values of R_0 as $n - m > 0$. However, the difference $n - m$ showed a decreasing trend asymptotically approaching zero.

5. The elevation angle θ_z was varied from 15° to 85°. The system model remained underdetermined for the entire range of θ_z. The difference $n - m$ increased rapidly because m decreased and n increased with increase in θ_z.

4.4 Pseudo-inverse as Minimum Norm Solution

The problem of computing a minimum norm solution Γ_θ to an underdetermined system of m linear equations $\Lambda\Gamma_\theta = S_\theta$ for Λ m-by-n complex dense matrix with $m \leq n$ occurs as a sub-problem in optimization algorithms. An underdetermined system either has no solution or has an infinity of solutions. This suggests that we strive to minimize $\| \Lambda S_\theta - \Gamma_\theta \|_p$ for some suitable choice of p. Different norms render different optimum solutions. Minimization in

the norm-1 and norm-∞ is complicated by the fact that the function $f(\Gamma_\theta) = \| \Lambda S_\theta - \Gamma_\theta \|_p$ is not differentiable for these values of p. In contrast to general norm-p solution, the least squares (LS) problem $\| \Lambda S_\theta - \Gamma_\theta \|_2$ is more tractable for following reasons:

- $\phi(\Gamma_\theta) = \frac{1}{2} \| \Lambda S_\theta - \Gamma_\theta \|_2^2$ is a differentiable function and so the minimizers of ϕ satisfy the gradient equation $\nabla\phi(\Gamma_\theta) = 0$. This turns out to be an easily constructed symmetric linear system which is positive definite if Λ has full column rank. The method of normal equations is based on this concept. However, the method of normal equations breaks down for ill-conditioned Λ.

- The norm-2 is preserved under orthogonal transformation. This means that we may determine an orthogonal Q such that the equivalent problem of minimizing $\| (Q^H\Lambda)S_\theta - (Q^H\Gamma_\theta) \|_2$ is easier to solve. Householder transformation is based on this approach.

The pseudo-inverse is a useful mathematical concept, but one would not usually incur the complexity to compute the pseudo-inverse explicitly in the process of searching for a solution to a least-squares problem. A classical method for solving the normal equations is based on the Cholesky decomposition.

4.5 Householder Transform

As an efficient computational approach to obtaining a pseudo inverse, the Householder transform has the numerical stability characteristic of orthogonal transforms. A Householder transform generates a matrix of the form $P = I - 2uu^H$ where Householder vector u has unity norm-2. It is easy to see that matrix P generated by Householder transform is symmetric: $P = P^H$ and orthogonal: $PP^H = I$. Px reflects an arbitrary vector x in the plane through the origin perpendicular to vector u. This transformation can be viewed geometrically as a reflection in $(m-1)$-dimensional subspace, S, orthogonal to the vector u. Given a vector x, a Householder transform may be determined such that $Px = [c, 0, 0, \ldots, 0]^H = ce_1$ for any complex constant c, where $e_1, e_2, e_3, \ldots, e_n$ are the

canonical basis for n-dimensional space. Thus u is a linear combination of x and e_1:

$$u = \frac{1}{2u^H x}(x - ce_1) \tag{4.54}$$

Such a vector u must be parallel to the vector

$$\tilde{u} = x \pm \| x \|_2 \, e_1 \quad so\ that \quad u = \frac{\tilde{u}}{\| u \|_2} \tag{4.55}$$

In vector form,

$$\begin{bmatrix} x_1 + sign(x_1) \| x \|_2 \\ x_2 \\ x_3 \\ . \\ . \\ x_m \end{bmatrix}$$

where, $sign(x_1) = \frac{x_1}{|x_1|}$ is defined for complex number x_1. As an example, the Householder transform of a hermitian transposed system model $\Lambda \in C^{m \times n}$ for $m = 4$ and $n = 5$ may be computed as shown in the next section.

4.6 Householder Transformation of System Model

Applying Householder Transform to $\Lambda \in C^{m \times n}$ for $m = 4$ and $n = 5$, where

$$\Lambda^H = \begin{bmatrix} x_{11} & x_{12} & x_{13} & x_{14} \\ x_{21} & x_{22} & x_{23} & x_{24} \\ x_{31} & x_{32} & x_{33} & x_{34} \\ x_{41} & x_{42} & x_{43} & x_{44} \\ x_{51} & x_{52} & x_{53} & x_{54} \end{bmatrix}$$

we obtain

$$x_1 = \begin{bmatrix} x_{11} \\ x_{21} \\ x_{31} \\ x_{41} \\ x_{51} \end{bmatrix}, \quad \tilde{u}_1 = \begin{bmatrix} x_{11} + sign(x_{11}) \parallel x_1 \parallel_2 \\ x_{21} \\ x_{31} \\ x_{41} \\ x_{51} \end{bmatrix}$$

Computing $u_1 = \frac{\tilde{u}_1}{\|\tilde{u}_1\|_2}$, choose $P_1 = I - 2u_1u_1^H$ so that

$$\Lambda_1 \equiv P_1\Lambda^H = \begin{bmatrix} x_{11} & x_{12} & x_{13} & x_{14} \\ 0 & x_{22} & x_{23} & x_{24} \\ 0 & x_{32} & x_{33} & x_{34} \\ 0 & x_{42} & x_{43} & x_{44} \\ 0 & x_{52} & x_{53} & x_{54} \end{bmatrix}$$

Now,

$$x_2 = \begin{bmatrix} x_{22} \\ x_{32} \\ x_{42} \\ x_{52} \end{bmatrix}, \quad \tilde{u}_2 = \begin{bmatrix} x_{22} + sign(x_{22}) \parallel x_2 \parallel_2 \\ x_{32} \\ x_{42} \\ x_{52} \end{bmatrix}$$

Computing $u_2 = \frac{\tilde{u}_2}{\|\tilde{u}_2\|_2}$, and $P_2^{'} = I - 2u_2u_2^H$, we then choose

$$P_2 = \begin{bmatrix} 1 & 0 \\ 0 & P_2' \end{bmatrix}$$

so that

$$\Lambda_2 \equiv P_2\Lambda_1 = \begin{bmatrix} x_{11} & x_{12} & x_{13} & x_{14} \\ 0 & x_{22} & x_{23} & x_{24} \\ 0 & 0 & x_{33} & x_{34} \\ 0 & 0 & x_{43} & x_{44} \\ 0 & 0 & x_{53} & x_{54} \end{bmatrix}$$

and

$$x_3 = \begin{bmatrix} x_{33} \\ x_{43} \\ x_{53} \end{bmatrix}, \quad \tilde{u}_3 = \begin{bmatrix} x_{33} + sign(x_{33}) \parallel x_3 \parallel_2 \\ x_{43} \\ x_{53} \end{bmatrix}$$

Computing $u_3 = \frac{\tilde{u}_3}{\|\tilde{u}_3\|_2}$, and $P_3' = I - 2u_3u_3^H$, we then choose

$$P_3 = \begin{bmatrix} 1 & 0 & 0 \\ 0 & 1 & 0 \\ 0 & 0 & P_3' \end{bmatrix}$$

so that

$$\Lambda_3 \equiv P_3\Lambda_2 = \begin{bmatrix} x_{11} & x_{12} & x_{13} & x_{14} \\ 0 & x_{22} & x_{23} & x_{24} \\ 0 & 0 & x_{33} & x_{34} \\ 0 & 0 & 0 & x_{44} \\ 0 & 0 & 0 & x_{54} \end{bmatrix}$$

Finally,

$$x_4 = \begin{bmatrix} x_{44} \\ x_{54} \end{bmatrix}, \quad \tilde{u}_4 = \begin{bmatrix} x_{44} + sign(x_{44}) \parallel x_4 \parallel_2 \\ x_{54} \end{bmatrix}$$

Computing $u_4 = \frac{\tilde{u}_4}{\|\tilde{u}_4\|_2}$, and $P_4^{'} = I - 2u_4u_4^H$, we choose

$$P_4 = \begin{bmatrix} 1 & 0 & 0 & 0 \\ 0 & 1 & 0 & 0 \\ 0 & 0 & 1 & 0 \\ 0 & 0 & 0 & P_4^{'} \end{bmatrix}$$

so that

$$\Lambda_4 \equiv P_4\Lambda_3 = \begin{bmatrix} x_{11} & x_{12} & x_{13} & x_{14} \\ 0 & x_{22} & x_{23} & x_{24} \\ 0 & 0 & x_{33} & x_{34} \\ 0 & 0 & 0 & x_{44} \\ 0 & 0 & 0 & 0 \end{bmatrix}$$

The iterative product of Householder matrices $P_1 P_2 P_3 P_4 \ldots$ for the CSAR system model is depicted in Fig. 4.9. It is interesting to see the main diagonal's diffusion over the iterations. Fig. 4.10 shows the corresponding iterative transformation of the system model. Finally, Fig. 4.11 shows the inverted system kernel.

4.6.1 Computational Cost

The cost of computing the Householder transform is $2n^2m - \frac{2}{3}n^3$, where m is the length of the vector and n is the number of vectors in the matrix undergoing Householder transform. The subsequent cost of back-substitution is $O(mn)$. The normal equations are twice as fast in computing the pseudo-inverse but are numerically unstable for an ill-conditioned system model Λ. A singular value decomposition (SVD) based pseudo-inverse technique has a higher computational load than the Householder transform based pseudo-inverse.

4.6.2 Q-Method

Once the Householder transform is computed, for further processing assume that $\Lambda \in C^{m \times n}$ with $m \leq n$ has full rank. Then,

$$\Lambda^H = Q \begin{bmatrix} R \\ 0 \end{bmatrix}$$

where $Q \in C^{n \times n}$ is orthogonal and $R \in C^{m \times m}$ is upper triangular. We have

$$S_\theta = \Lambda \Gamma_\theta = [R^H 0] Q^H \Gamma_\theta = R^H y_1 \tag{4.70}$$

where

$$y = \begin{bmatrix} y_1 \\ y_2 \end{bmatrix} = Q^H \Gamma_\theta$$

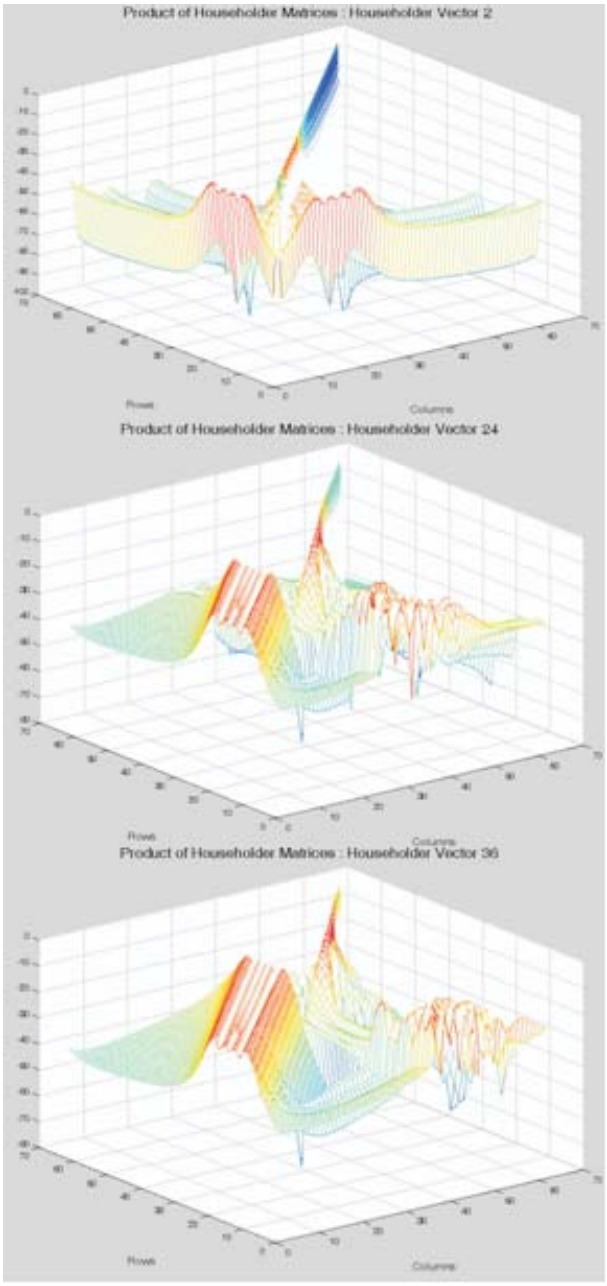

Figure 4.9. Iterative product of Householder matrices $P_1P_2P_3P_4\ldots$ shows a diffusing main diagonal.

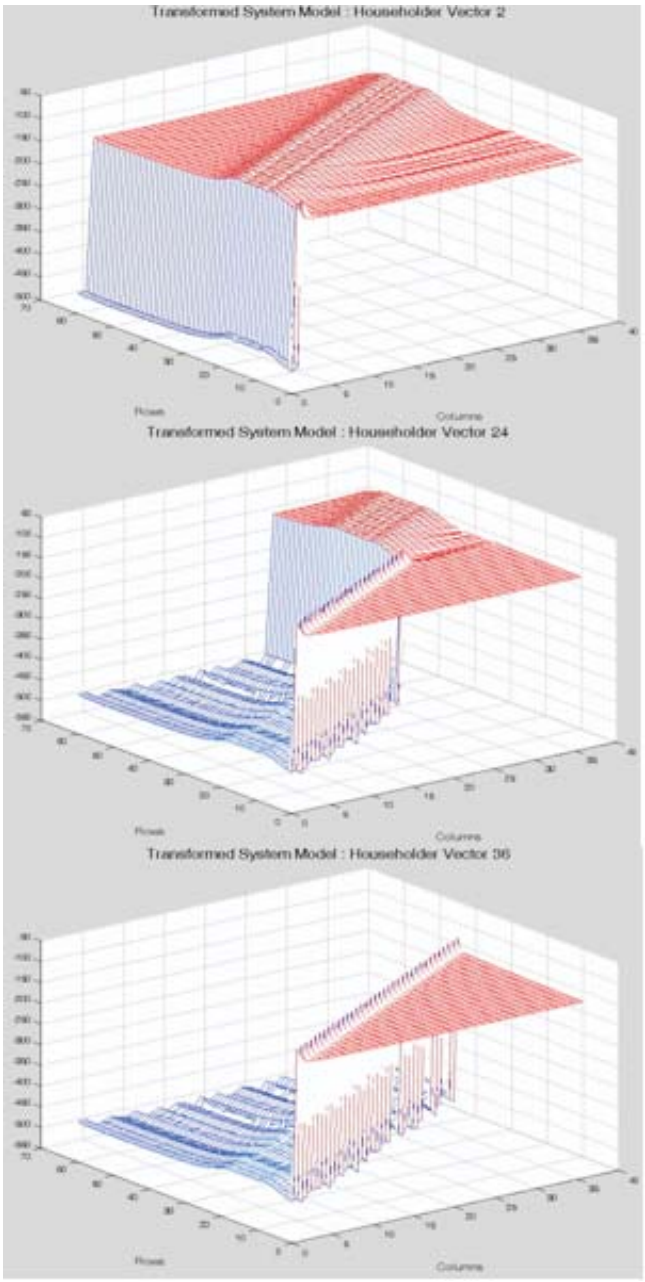

Figure 4.10. Transformed system model during the iterative process.

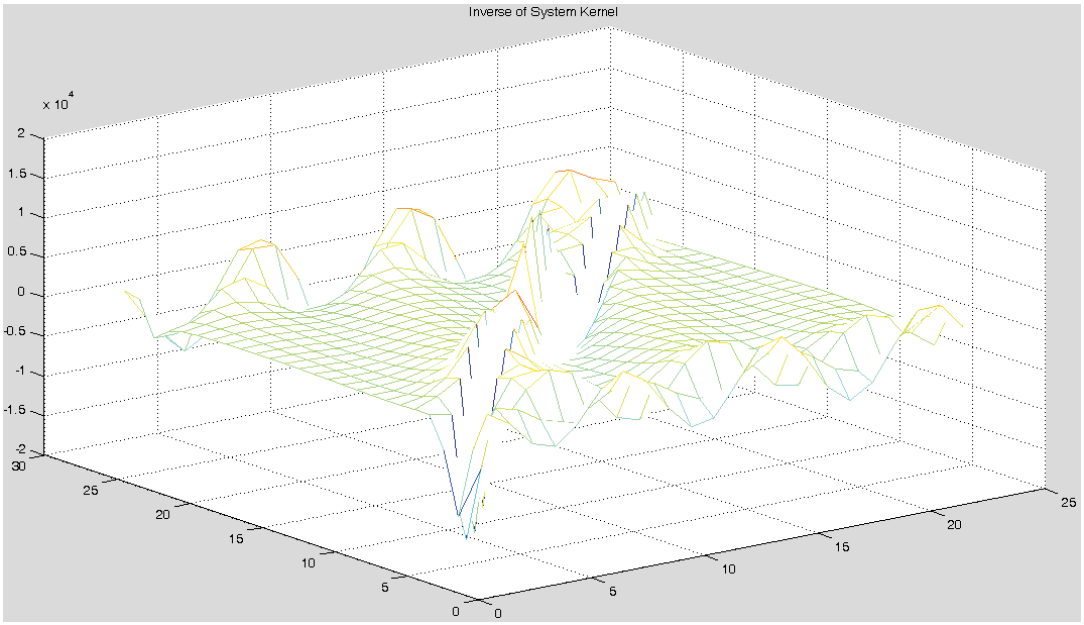

Figure 4.11. Inverse system kernel $\Lambda^{-1}(\omega, \omega_g)$ (real part).

If Λ has full rank then $y_1 = R^{-H} S_\theta$ is uniquely determined and all solutions of $S_\theta = \Lambda \Gamma_\theta$ are given by

$$\Gamma_\theta = Q \begin{bmatrix} y_1 \\ y_2 \end{bmatrix}$$

$$y_2 \in C^{n-m}$$

The unique solution $\Gamma_{\theta LS}$ that minimizes $\| \Gamma_\theta \|_2$ is obtained by setting $y_2 = 0$. This yields

$$\Gamma_{\theta LS} = Q \begin{bmatrix} R^{-H} S_\theta \\ 0 \end{bmatrix}$$

Hence,

$$\Gamma_{\theta LS} = QRR^{-1}R^{-H}S_{\theta} = QR(R^{H}R)^{-1}S_{\theta} \tag{4.74}$$

Substituting $\Lambda^{H} = QR$, for an orthogonal matrix Q: $QQ^{H} = I$ we get

$$\Gamma_{\theta LS} = \Lambda^{H}(\Lambda\Lambda^{H})^{-1}S_{\theta} = \Lambda^{\dagger}S_{\theta} \tag{4.75}$$

It follows that when Λ has full rank the pseudo-inverse of Λ solving an underdetermined system is given by

$$(\Lambda)^{\dagger} = QR^{-H} \tag{4.76}$$

The orthogonal matrix Q is the first four columns of the product $P_1P_2P_3P_4$ and the upper triangular matrix R is the first 4 rows of Λ_4, in the example presented in section 4.5.

It is pointed out that the systematic use of orthogonal transformations to reduce matrices to simpler form was initiated by Givens [58] and Householder [59]. The application to the linear least squares problem is due to Golub [60].

4.6.3 Further Processing

The further processing steps in CSAR reconstruction are matched filtering in the ground-plane followed by interpolation. The target function is reconstructed from the CSAR ground-plane signal via the following matched filtering in the frequency domain of θ, designated here as ξ:

$$F_{\rho}(\rho, \xi) = S_{g}(\omega_g, \xi)S^{*}_{g0}(\omega_g, \xi) \tag{4.77}$$

for $| \xi | \leq \rho R_0(\omega)$, where the asterisk signifies the complex conjugate operation. The subsequent target spectrum in the polar spatial frequency domain is formed by an inverse Fourier transform with respect to ξ. Finally, the target function in the rectilinear spatial frequency domain is obtained by interpolation defined as follows:

$$k_x(\omega, \theta) = \rho\cos\theta \tag{4.78}$$

$$k_y(\omega, \theta) = \rho\sin\theta \tag{4.79}$$

The two-dimensional inverse Fourier transform of this signal is the desired target image $f(x, y)$.

4.6.4 Error Bounds and Stability

The method used for obtaining the ground-plane CSAR signal using a Householder transform is referred to as the "Q-method". It computes a minimal norm-2 solution to an underdetermined system of type $Ax = b$ of full rank. It has been shown that the computed solution $\hat{x}$ from the Q-method satisfies

$$\frac{\| \hat{x} - x \|_2}{\| x \|_2} \leq c_1 u \kappa_2(A) + O(u^2) \tag{4.80}$$

for a condition number $\kappa_2(A) = \| A^{\dagger} A \|_2$. c_1 denotes a modest constant depending on matrix dimensions m and n, and u is the unit roundoff. For instance the unit roundoff for Matlab is $u \approx 2.2 \times 10^{-16}$. This result was shown to further strengthen significantly by employing component wise analysis. Existing error analysis shows that the norm-wise error is bounded to first order by $c\kappa_2(A)u$. These error bounds can be strengthened by replacing $\kappa_2(A)$ by the potentially much smaller quantity $cond_2(A) = \| | A^{\dagger} | \, | A | \|_2$ which is invariant under row scaling of A. This form of condition number reflects the sensitivity of the minimum norm solution x to row-wise relative perturbations in the data A and b. The Householder Transform based processing has guaranteed stability. The Q-method is forward stable in the row-wise sense and "almost" row-wise backward stable.

4.6.5 Simulation and Results

The intermediate results of the Householder transformation were already presented in Fig. 4.9 and Fig. 4.10. Fig. 4.12 shows reconstruction using Householder transform for an omni-directional reflector located in the center of the target area $(x_n, y_n) = (0, 0)$. Fig. 4.12 consists of three images where the first image is the Fourier domain support or CSAR spectrum $F_n(k_x, k_y)$. The CSAR spectrum signal is a constant within the ring-shaped band.

The second image is the corresponding psf determined by the equation:

$$f_n(x,y) = \rho_{max}\frac{J_1(r\rho_{max})}{r} - \rho_{min}\frac{J_1(r\rho_{min})}{r} \tag{4.81}$$

where $r = \sqrt{x^2+y^2}$, J_1 is the Bessel function of the first kind, first order [38], and

$$\rho_{max} = 2k_{max}\cos\theta_z \;\; and \;\; \rho_{min} = 2k_{min}\cos\theta_z \tag{4.82}$$

The third image is just the top view of the second image.

Fig. 4.13 presents an out-of-focus reconstruction brought about by taking a hermitian transpose during the Householder transformation. The hermitian transpose introduces a phase error in CSAR phase history data analogous to an altitude mismatch between the CSAR signal and the matched filter signal. The out-of-focus reconstruction underscores the three dimensional character of CSAR imaging.

4.7 Conclusion

The CSAR signal was processed using a Householder transform. The ground-plane CSAR signal was computed from slant-plane CSAR data collected from an omni-directional reflector located in the center of the target area. Each column vector of the system model was reflected in the plane through the origin perpendicular to the vector u. Later, the Q-method was applied to transformed matrices to obtain the ground-plane CSAR signal. The computational cost of the Householder transform was shown to be $2n^2m - \frac{2}{3}n^3$, where m is the length of the vector and n are the number of vectors. The Q-method was also shown to have improved error bounds and stability.

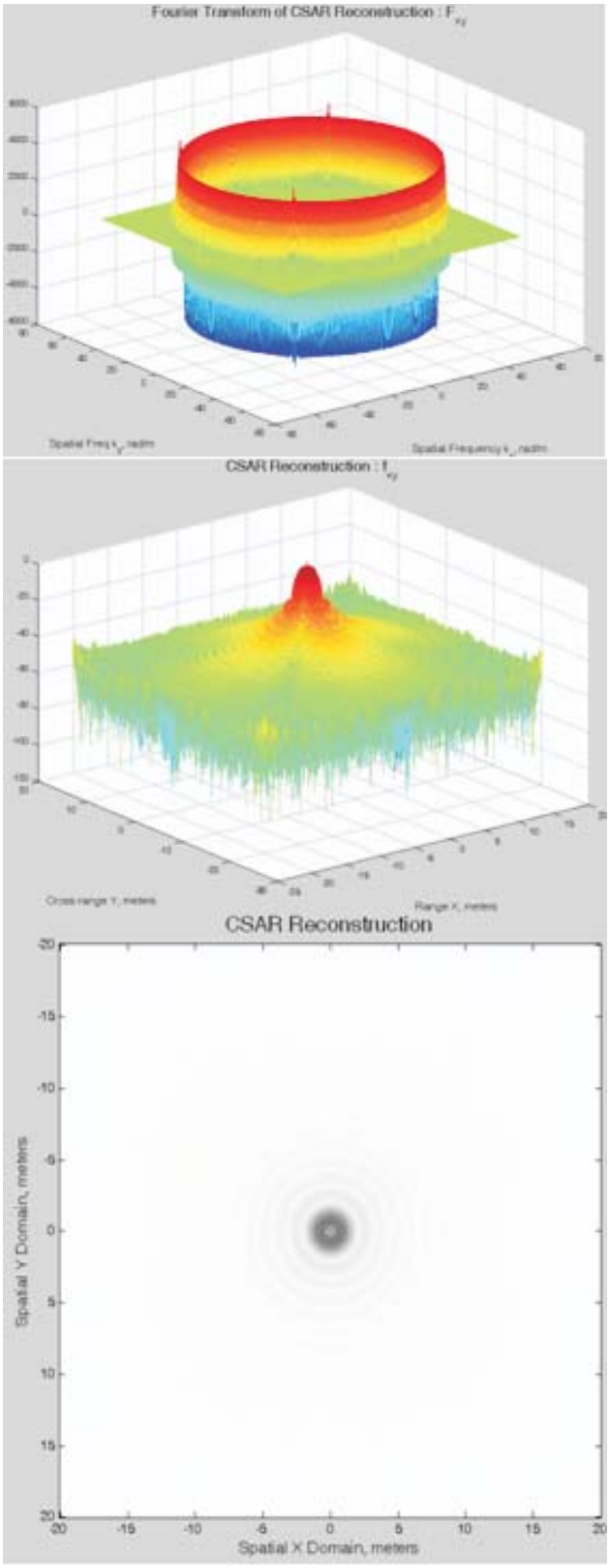

Figure 4.12. Ring-shaped Fourier domain support and target reconstruction.

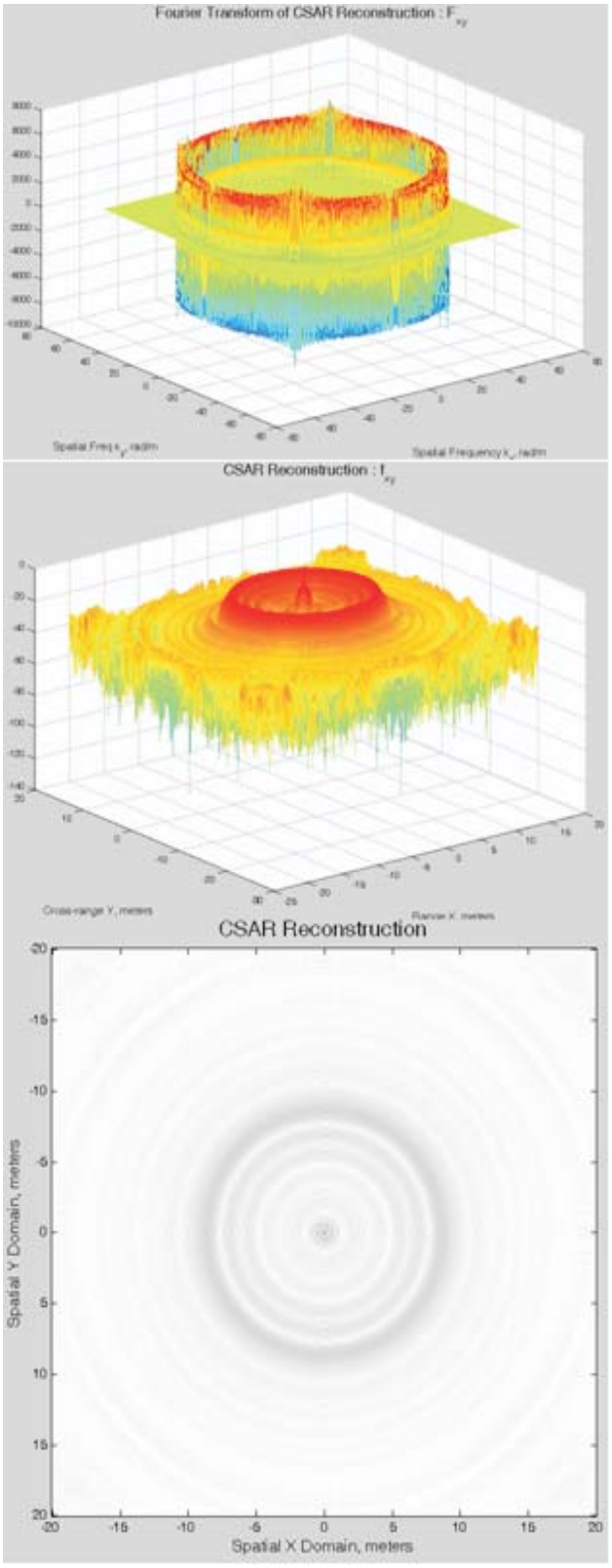

Figure 4.13. Out-of-focus ring-shaped Fourier domain support and target reconstruction.

CHAPTER 5

REFOCUSING OF DEFOCUSED IMAGES [6]

This research utilizes the methodology of the SAR 2-D aperture synthesis algorithm, a two dimensional variant of the $\omega - k$ algorithm, to refocus out-of-focus images. Refocusing of images may be necessary in machine vision as a preprocessing step before edge detection or image segmentation in the imaging and manipulation of 3-D objects. The SAR 2-D aperture synthesis algorithm generates a complex amplitude distribution and the corresponding point spread function in a manner similar to Fraunhofer diffraction distribution model and its psf as seen in Fourier optics. The matched filter utilized in the SAR 2-D aperture synthesis algorithm has a focus-in-altitude interpretation and may be varied to increase or decrease the radius of out-of-focus blur associated with a particular psf of scatterers of various heights. This paper demonstrates focusing of a simple line object $L = (1 : x = y \ -64 \leq x \leq 63, -64 \leq y \leq 63)$. Although a rectangular aperture is used in the refocusing process, other apertures may also be used such as circular or Gaussian.

In optical imaging, the imaging system is first focused and then data are collected. In SAR imaging data are first collected and then focused through signal processing as depicted in Figures 5.1, 5.2 and 5.3 using a back-projection focusing algorithm. Hence, SAR signal processing algorithm is necessarily a focusing algorithm. Conventional slant-plane SAR employs two entirely different methodologies for target area image formation: a pulsed fast time imaging technique is used perpendicular to the flight path, and a "Doppler" induced slow-time imaging technique is used along the flight path. The use of $\omega - k$ algorithm for slow time signal processing of slant plane SAR data is a new trend [29], [28], [8], [15], [16], [17], [39], [32], [13], [51]. The key concept in the SAR 2-D aperture synthesis algorithm is the extension of the one dimensional slow time imaging technique based upon $\omega - k$ algorithm to two dimensions [2], [1], [26], [31], [52], [38]. In coherent optics, spherical wave illumination of an aperture produces a complex amplitude distribution proportional to

the Fourier transform of the aperture transmittance function, scaled by the wavelength times the convergence distance. This is the most important result reached in the development of Fourier optics [40], [18]. The two dimensional variant of $\omega - k$ algorithm, exposes similar complex amplitude Fraunhofer diffraction distributions as seen in Fourier optics. The matched filter has a focus-in-altitude interpretation. This work delves into this inherent focusing ability of the matched filter to refocus data to one distance parameter that has been previously focused to another distance parameter. In this sense, the method provides an approach to refocus defocused images.

In machine vision, processing tasks such as edge detection, image segmentation, etc., are easier for focused images than for defocused images of 3-D scenes. However, the image of a camera is not identically focused for all objects in the camera scene. The target object and those objects at the same distance as the target object will be focused. All other objects at distances other than that of the target object will be blurred by different degrees depending on their distance from the camera. The amount of defocus blur also depends on the camera parameters such as lens position with respect to image detector, focal length of the lens, and diameter of the camera aperture. Two blurred images of the same camera scene are usually used in the refocusing process [61]. Initially, a blur parameter "sigma" is estimated then one of the two blurred images is deconvolved to recover the focused image. This refocusing may be done with or without the knowledge of the camera psf.

5.1 SAR with 2-D Aperture Synthesis

The SAR with 2-D aperture synthesis algorithm is a two dimensional variant of the conventional 1-D slant-plane SAR and, as the name signifies, involves two dimensional aperture synthesis. The shape of the aperture may be rectangular, circular, etc. The analytical development of SAR with 2-D aperture synthesis is based on 3-D Cartesian coordinate system with distance to n^{th} point target located at $(x_n, y_n, 0)$ in the x-y plane expressed as follows:

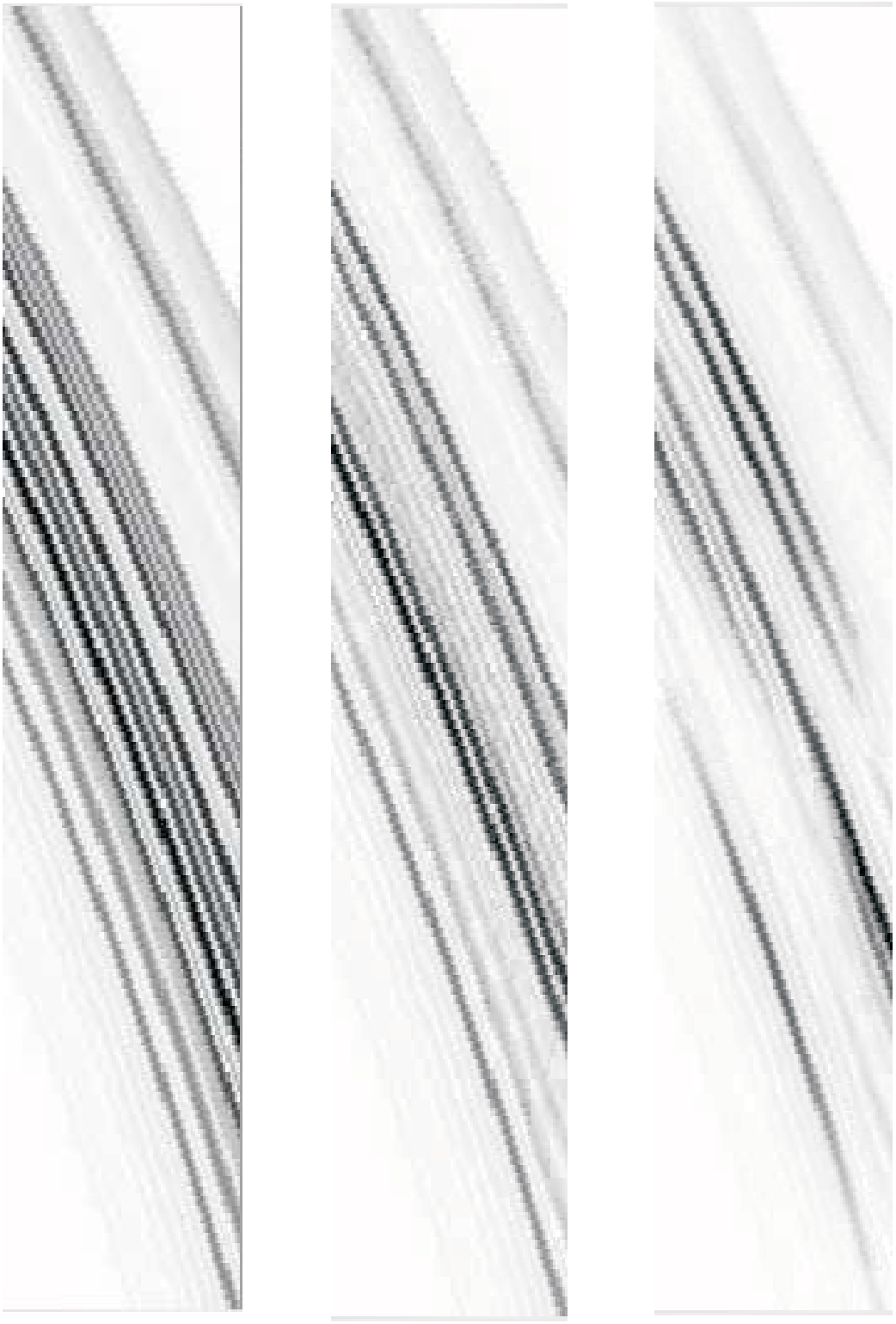

Figure 5.1. Refocusing of SAR data for 5 point targets : snapshots 1, 2 and 3.

Figure 5.2. Refocusing of SAR data for 5 point targets : snapshots 4, 5 and 6.

Figure 5.3. Refocusing of SAR data for 5 point targets : snapshots 7, 8 and 9.

$$R_n(U_x, U_y) = \sqrt{(x_n - U_x)^2 + (y_n - U_y)^2 + U_z^2} \tag{5.1}$$

The distance measure of conventional linear SAR is given as follows for quick comparison:

$$R_n(U_y) = \sqrt{(x_n - U_x)^2 + U_y^2} \tag{5.2}$$

The position of the radar at any instant is given by coordinates (U_x, U_y, U_z), with U_z =constant as the height of the SAR in meters and a known parameter. The received echo after base-band conversion $S\,s(\omega, U_x, U_y)$ is a function of transmitted frequency ω in radians, radar position on $x-$axis U_x, and radar position on $y-$axis U_y, as shown in Fig. 5.4(a). A rectangular sampling grid was used from the signal-processing stand point. A two-dimensional Fourier transform of $S\,s(\omega, U_x, U_y)$ is computed to obtain $S\,s(\omega, ku_x, ku_y)$, where ku_x and ku_y are the Fourier domain variables corresponding to U_x and U_y, respectively, depicted in Fig. 5.4(b).

The matched filtering in the 2-D Aperture Synthesis algorithm has a focusing-in-height interpretation that extracts the target informative part of the phase history for inverse Fourier processing. The output of a matched filter $F(k_x, k_y)$ is shown in Fig. 5.4(c). The simulation height was kept at $1000\,m$. The 2-D aperture aynthesis algorithm is interpolation free as Fourier domain variables can be equated as $ku_x = k_x$ and $ku_y = k_y$ [35]. Finally, the target area reconstruction f_{xy} is achieved by an inverse Fourier transform of the matched filter output shown in Fig. 5.4(d). The psf in this case is called a *besinc* function, and is also called *sombrero* function. The psf function is determined by the aperture shape (circular was used in these simulations).

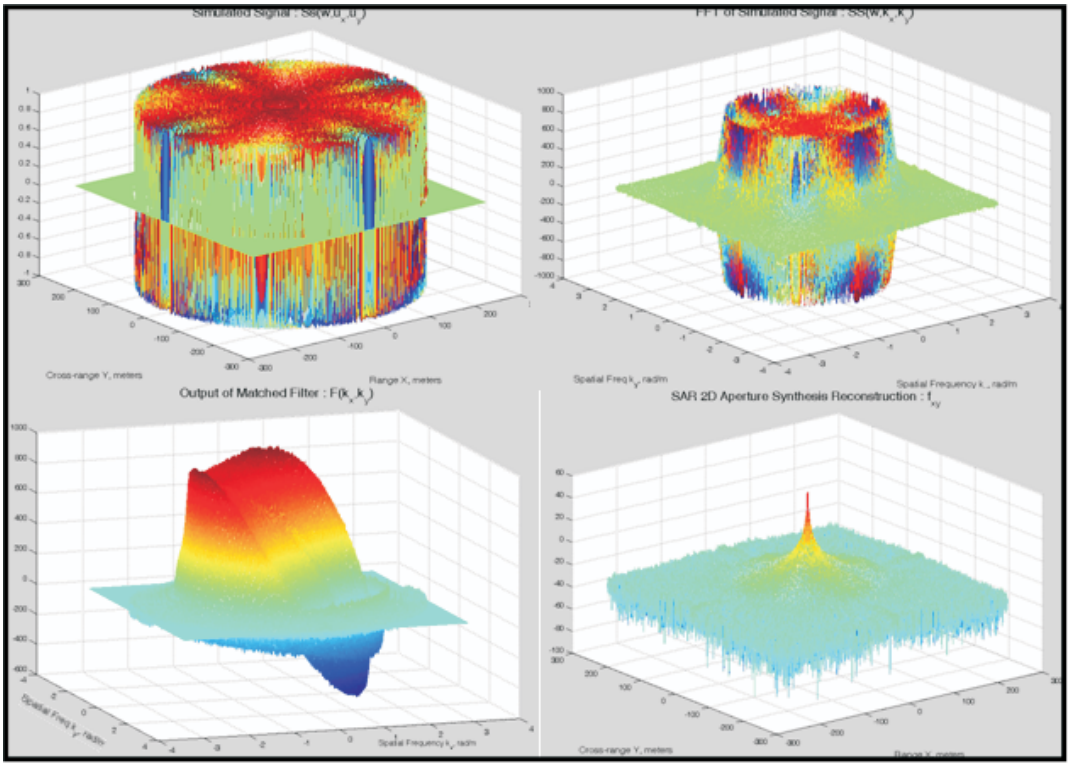

Figure 5.4. (a) Simulated echoed signal $S\,s(\omega, U_x, U_y)$, (b) Simulated echoed signal $S\,s(\omega, ku_x, ku_y)$, (c) Matched filter output $F(k_x, k_y)$, (d) Reconstruction f_{xy}.

5.1.1 Matched Filtering with Incorrect Altitude

An analysis of the 2-D aperture aynthesis algorithm when used for refocusing is performed next by matched filtering with incorrect altitudes to see out-of-focus target area reconstructions. The simulation altitude is 1000 m. Fig. 5.5(a) shows the reconstruction where the focusing filter is also matched to 1000 m. Fig. 5.5(b) shows the reconstruction for an error in altitude of ± 10 m in the matched filter. Fig. 5.5(c) shows the reconstruction for an error in altitude of ± 50 m. Fig. 5.5(d) shows the reconstruction for an error in altitude of ± 100 m. Fig. 5.5(e) shows the reconstruction for an error in altitude of ± 200 m. Finally, Fig. 5.5(f) shows the reconstruction for an error in altitude of ± 900 m. The radius of the blur circle increases with the extent of height-mismatch in the focusing filter. The blur function shape corresponds to the aperture shape, which was circular in this case. Concentric side lobe rings are apparent in all the defocused psfs, as characteristic of *besinc* or *sombrero* function. The intensity of such a complex amplitude distribution is called an *Airy*

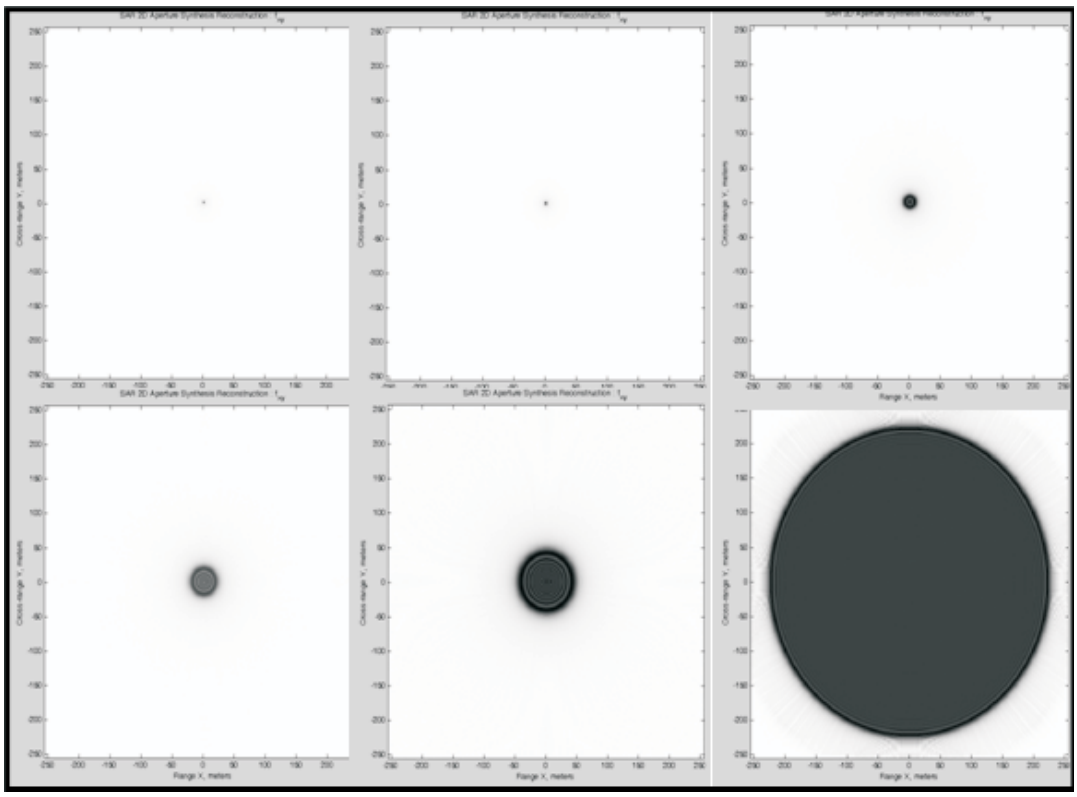

Figure 5.5. (a) Matched filter at 1000 *m*, **(b) Error of** ±10 *m*, **(c) Error of** ±50 *m*, **(d) Error of** ±100 *m*, **(e) Error of** ±200 *m*, **(f) Error of** ±900 *m*.

disk in Fourier optics.

5.1.2 Fourier Optics Analogy

In optics, converging spherical wave illumination of an aperture produces a complex amplitude distribution proportional to the Fourier transform of the aperture transmittance function. This distribution is centered on the nominal point of convergence and is scaled by the wavelength times the convergence distance. This is a pivotal result in Fourier optics: it plays a central role in the theory of image formation by spherical lenses and leads to many of the important signal processing applications of optical systems. CSAR and 2-D aperture synthesis imaging algorithms offer a unique opportunity of comparing SAR signal processing with Fourier optics as both sets of algorithms employ 2-D spatial variables in Euclidean space and exhibit Fraunhofer diffraction behavior. SAR has benefited from contributions from optics, and optical signal processing has been used for SAR image formation prior

to the advent of digital signal processing. But a comparison at the level of Fraunhofer diffraction patterns has never been done prior to this work.

5.1.3 Defocused Image

Well focused images contain more information (detail) than defocused images. Perceived sharpness of an image enables a human observer to determine if an image is in focus. If one observes the frequency components when the image is blurred, then their amount will increase as the image is near in focus. This phenomenon can be understood theoretically by considering simple image formation example shown in Fig. 5.6. In this figure, f is the focal length, d_o is the distance between object-plane and the lens, and d_i is the distance between the lens and the image-plane. Variations in any of these three parameters will impact the image formation in this simple lens imaging system. In Fig. 5.6 since the object P is focused in front of the image plane, the resultant image will be out-of-focus or blurred. According to Fourier optics, the image of point object P has the same shape as the lens aperture. If a lens is ideal, its ability to produce an ideal point source is limited only by diffraction. The response of the camera lens system to an ideal point source is then called the psf, analogous to the impulse response in linear system theory. The psf of an ideal lens is defined as

$$h_{ideal}(x,y) = h_{ideal}(r) = \begin{cases} \frac{1}{\pi R^2}, & \text{if } r < R; \\ 0, & \text{otherwise.} \end{cases} \tag{5.3}$$

where $r^2 = x^2 + y^2$. R is the radius of the blur circle. The optical transfer function corresponding to the preceding point spread function is

$$H_{ideal}(u,v) = H_{ideal}(\rho) = 2\frac{J_1(R\rho)}{R\rho} \tag{5.4}$$

where the radial spatial-frequency $\rho^2 = u^2 + v^2$ and J_1 is the first-order Bessel function of the first kind. The optical transfer function is simply the Fourier transform of the psf and

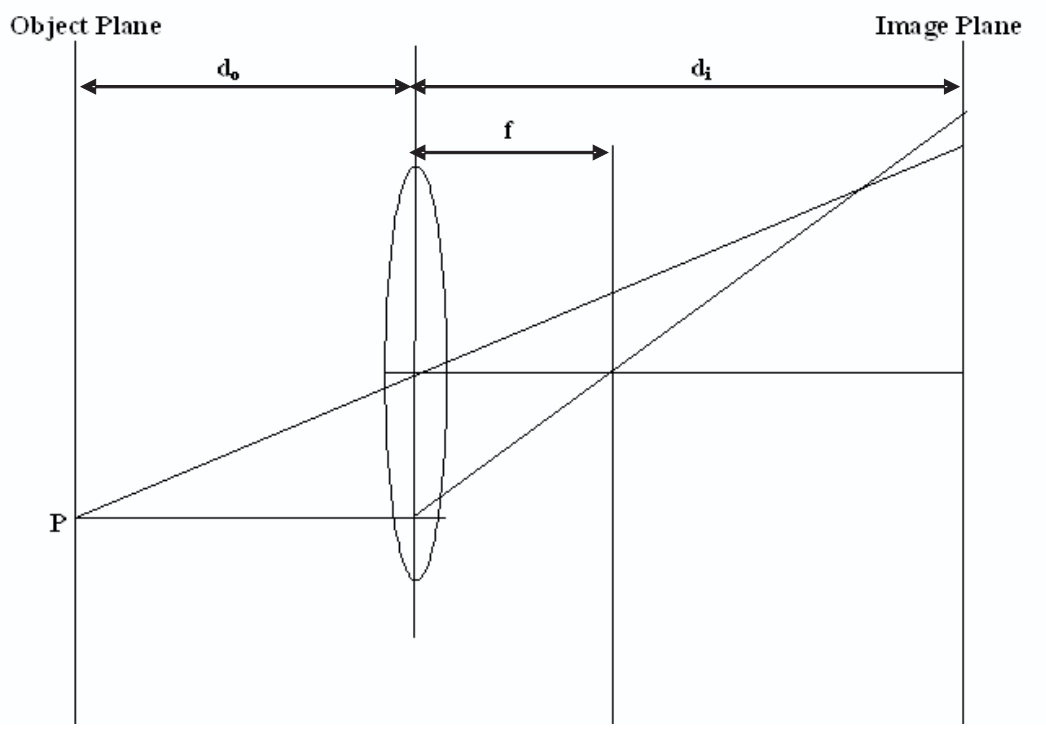

Figure 5.6. Lens imaging.

provides information on how an electro-optical system affects the spatial frequency amplitudes and phases. Fig. 5.7 shows cross sections of the optical transfer function $H_{ideal}(\rho)$ for various values of R.

The psf of non-ideal multiple lens systems can be modeled as

$$h_{effective}(x,y) = h_1(x,y) \times h_2(x,y) \times h_3(x,y) \times \cdots \times h_n(x,y) \tag{5.5}$$

Since it is challenging to determine the psf of each of the individual elements of the lens system, the generalized psf of the camera system will be assumed to be Gaussian. The Gaussian psf is defined as

$$h_{Gaussian}(r) = \frac{1}{\sqrt{2\pi}\sigma} \exp(-\frac{r^2}{2\sigma^2}) \tag{5.6}$$

where σ is the blur parameter and is the standard deviation of the distribution of the psf, and therefore is the only parameter that needs to be determined for this simple model. Moreover, σ is proportional to R in both circularly symmetric and Gaussian psfs

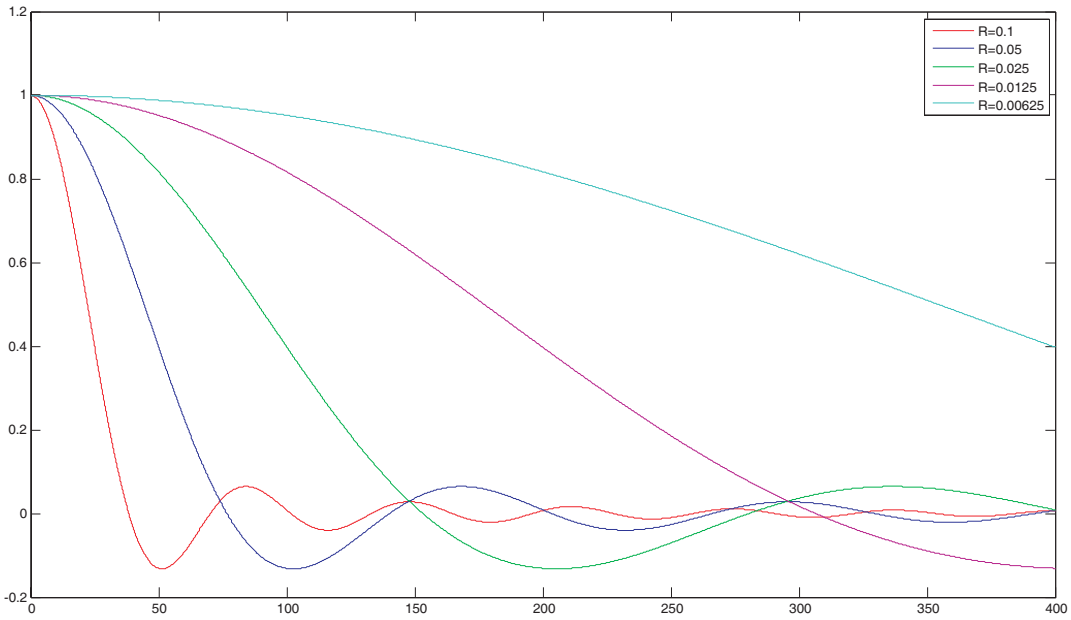

Figure 5.7. The cross sections of $H_{ideal}(\rho)$.

$$\sigma = kR \tag{5.7}$$

where k is proportionality constant which is approximately equal to $\frac{1}{\sqrt{2}}$ for circularly symmetric psf and equal to 1 for Gaussian psf. The optical transfer function is again computed by Fourier transforming $h_{Gaussian}(r)$ and is also Gaussian as shown in Fig. 5.8.

$$H_{Gaussian}(\rho) = \exp(-\frac{R^2\rho^2}{4}) \tag{5.8}$$

The defocusing operation of a lens may be interpreted as the low pass filtering of the scene data with a variable cutoff frequency. The cutoff frequency is highest when the lens is in the focused position and decreases as the lens goes into a defocused position. The main difference between the two optical transfer functions $H_{ideal}(\rho)$ and $H_{Gaussian}(\rho)$ is that there are no side lobes associated with the Gaussian optical transfer function.

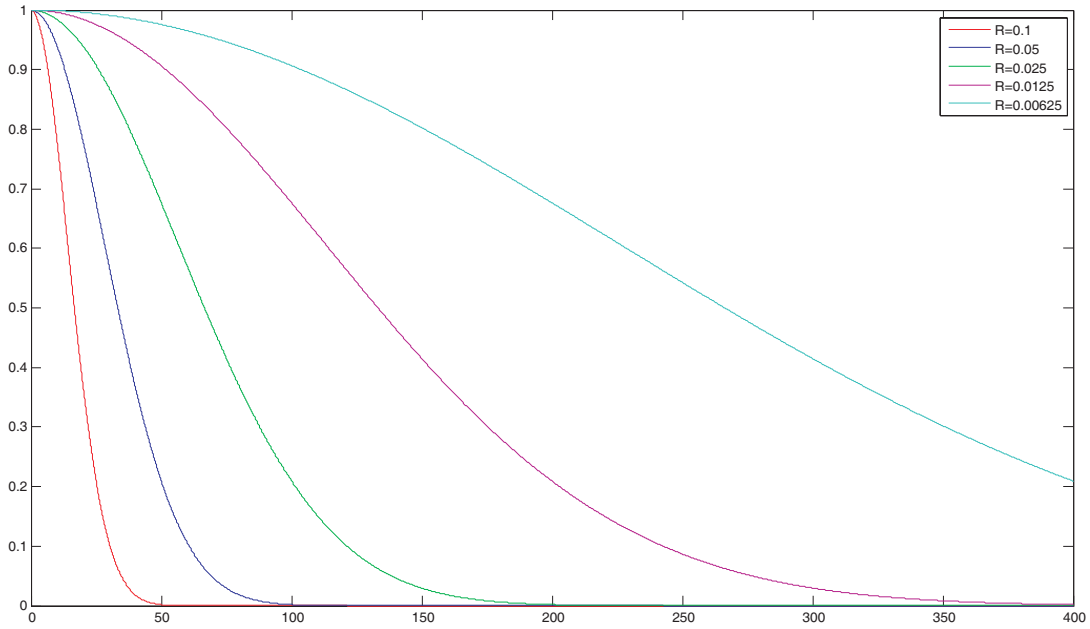

Figure 5.8. The cross sections of $H_{Gaussian}(\rho)$.

5.1.4 Image Focusing using SAR 2-D Aperture Synthesis Algorithm

The 2-D aperture synthesis algorithm has the ability to produce two dimensional distributions similar to Fourier optics. The 2-D aperture synthesis algorithm also performs controlled defocusing of the psf. Moreover, the 2-D aperture synthesis algorithm being an invertible or bidirectional algorithm, defocused psf can be refocused.

5.1.5 Aperture Shape

As mentioned earlier, various aperture shapes may be employed in the refocusing process including circular, rectangular, ring or Gaussian. It is pointed out that a commonly used model for the generalized psf of the camera system is Gaussian. This research uses rectangular aperture in the refocusing process. In practice, the refocusing aperture shape needs to match the data acquisition aperture.

5.1.6 Autofocus Measures

Since high frequency components determine the sharpness of the object image, the image gradient equation (5.9) may be employed for a measure of focus [62]. Image gradients

are based on the first partial derivatives and therefore they have high pass filter properties. Among many spatial gradient operations, Robert's gradient is most common. The Sobel gradient is a slightly more complicated gradient operation. The focus measure which utilizes the Sobel gradient is commonly referred to as the Tenengrad function [63]. The mathematical Laplacian is also used for focus measure equation (5.11). Besides partial derivative based focus measures, the image energy may also be used for a focus measure per Parseval's theorem equation (5.13). Let $g(x, y)$ is the $N \times N$ grey scale image. We shall use $\frac{1}{N \times N} \sum_x \sum_y |g(x, y)|$ in our focus measure. This measure suffices the recovery of the simplistic image of line $L = (1 : x = y \ -64 \leq x \leq 63, -64 \leq y \leq 63)$.

$$FM_{grad} = \sum_x \sum_y (\nabla g(x, y))^2 = \sum_x \sum_y (G_x^2 + G_y^2) \tag{5.9}$$

where,

$$\nabla g(x, y) = \begin{bmatrix} G_x & G_y \end{bmatrix}^T = \begin{bmatrix} \frac{\partial g}{\partial x} & \frac{\partial g}{\partial y} \end{bmatrix}^T \tag{5.10}$$

and,

$$FM_{Lap} = \sum_x \sum_y (\nabla^2 g(x, y))^2 = \sum_x \sum_y (\begin{bmatrix} \frac{\partial^2 g}{\partial x^2} & \frac{\partial^2 g}{\partial y^2} \end{bmatrix}^T)^2 \tag{5.11}$$

where,

$$\nabla^2 g(x, y) = \begin{bmatrix} \frac{\partial^2 g}{\partial x^2} & \frac{\partial^2 g}{\partial y^2} \end{bmatrix}^T \tag{5.12}$$

and,

$$FM_{energy} = \sum_x \sum_y |\nabla g(x, y)|^2 \tag{5.13}$$

5.2 Implementation of Refocusing Algorithm and Simulations

5.2.1 Blurred Image for Simulations

The blurred $N \times N$ image $g(x, y)$ required for simulations was obtained by randomly defocusing the line object $L = (1 : x = y \ -64 \leq x \leq 63, -64 \leq y \leq 63)$ with the rectangular aperture 2-D aperture synthesis algorithm, and taking the absolute value of the result. This blur height is unknown to the 2-D aperture synthesis algorithm performing subsequent refocusing.

5.2.2 $T : \mathbb{R}^2 \rightarrow \mathbb{C}^2$ Mapping of $g(x, y)$

The SAR 2-D aperture synthesis algorithm works on complex data in the unitary space $\mathbb{C}^2$. This requires attaching phase history information to real images in $\mathbb{R}^2$ space for mapping into $\mathbb{C}^2$ space. Let $g(x, y)$ be the $N \times N$ defocused image such that $g(x, y) = 0$. Then, there exists a complex amplitude distribution $a + jb$ corresponding to $N \times N$ arbitrarily defocused unit amplitude point targets such that $|a + jb| = 1$ processed through the SAR 2-D aperture synthesis algorithm. $T : \mathbb{R}^2 \rightarrow \mathbb{C}^2$ mapping of $g(x, y)$ is simply the element by element product as given below:

$$Tg(x, y) = g(x, y)\,[a + jb] \tag{5.14}$$

5.2.3 Convergence of Refocusing Algorithm

The convergence of the refocusing algorithm may be written as in equation (5.15), where FM_μ is the focus measure at some matched filter variation μ and FM_0 is the focus measure of a fully focused image. It is also pointed out that the matched filter variation μ is in fact the error in the matched filter varying the blur circle. The convergence of the refocusing algorithm is depicted in Fig. 5.9(a) and (b). Fig. 5.9(c) is the refocused image of line object $L = (1 : x = y \ -64 \leq x \leq 63, -64 \leq y \leq 63)$. The convergence curve is presented in Fig. 5.10.

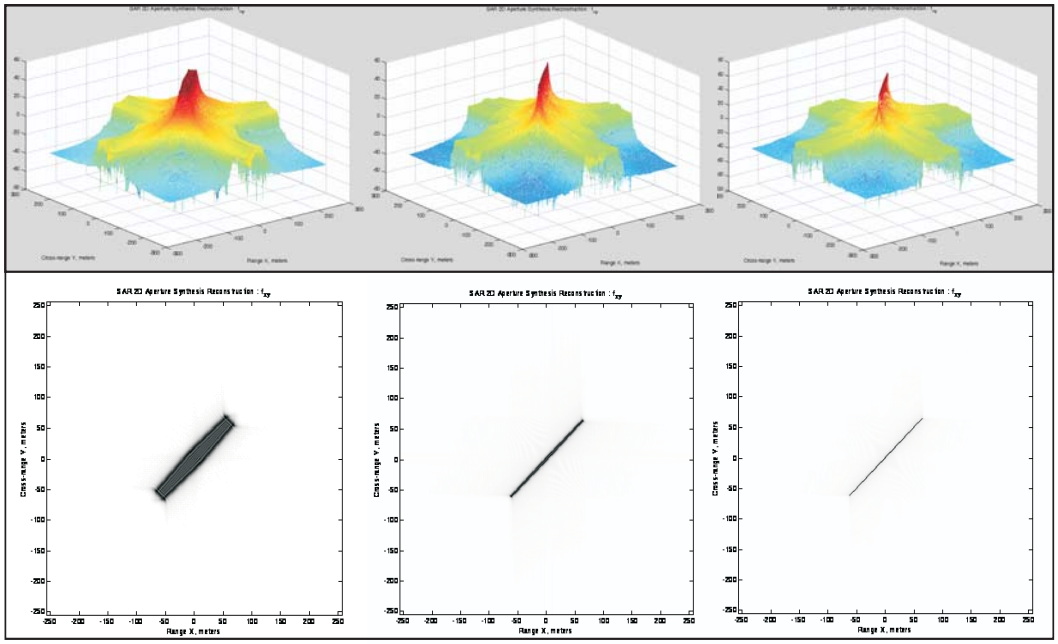

Figure 5.9. (a) Convergence at μ_1, (b) Convergence at μ_2, (c) Refocused image.

$$\left\| FM_{\mu} - FM_0 \right\| \rightarrow 0 \quad as \quad \mu \rightarrow 0 \tag{5.15}$$

5.2.4 Refocusing Algorithm

1. Choose μ_1 and μ_2 defocus parameters.
2. $T_{\mu 1} : \mathbb{R}^2 \rightarrow \mathbb{C}^2$ mapping of $g(x, y)$.
3. $T_{\mu 2} : \mathbb{R}^2 \rightarrow \mathbb{C}^2$ mapping of $g(x, y)$.
4. 2-D aperture synthesis processing.
5. Compute focus measures $FM_{\mu 1}$ and $FM_{\mu 2}$.
6. Determine direction of convergence based upon comparison of $FM_{\mu 1}$ and $FM_{\mu 2}$.
7. Increment defocus parameter μ in the direction of convergence.
8. $T_{\mu} : \mathbb{R}^2 \rightarrow \mathbb{C}^2$ mapping of $g(x, y)$.

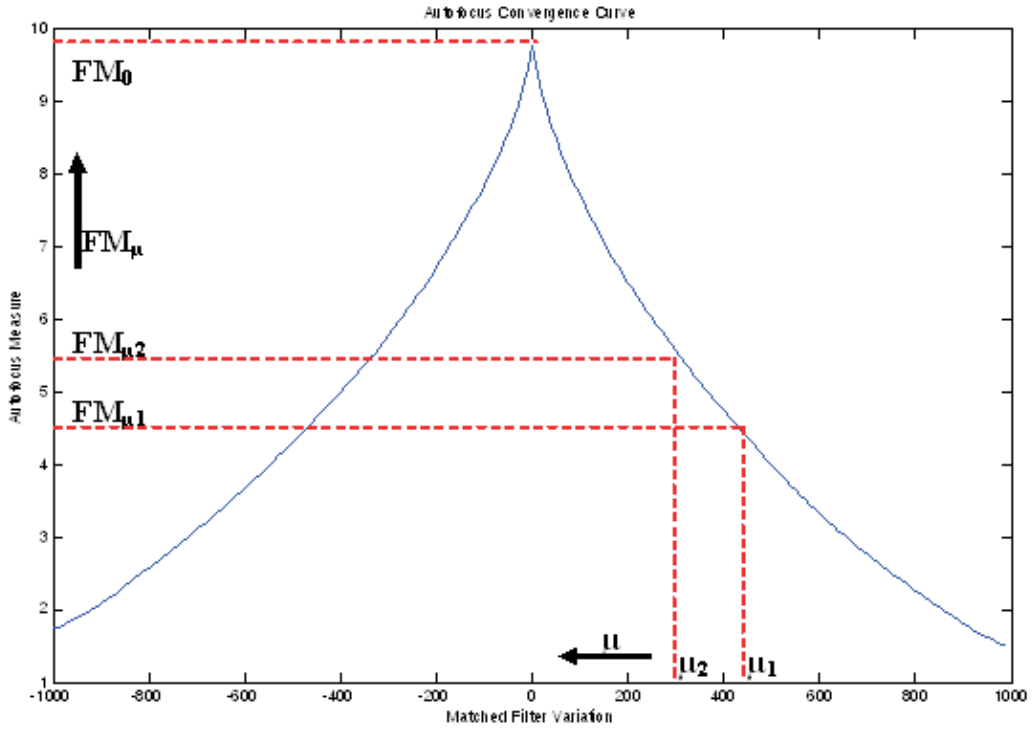

Figure 5.10. Convergence curve for refocusing algorithm.

9. 2-D aperture synthesis processing.

10. Compute focus measure FM_{μ}.

11. End if image is focused otherwise loop back to step 7.

5.2.5 Gaussian Aperture

The circular and rectangular apertures create suboptimal diffraction patterns in optical imaging. Scattered light in a telescope and the diffraction pattern of the telescope's aperture limit the contrast. The Gaussian aperture shown in Fig. 5.11 is considered to be a good candidate for high contrast telescopic imaging in astronomical planetary search [64]. It is considered to be in a class of *apodized* apertures. This is coupled with the fact that a commonly used model for the generalized psf of the camera system is Gaussian. It would be interesting to explore refocusing of defocused images employing a Gaussian aperture with the SAR 2-D aperture synthesis algorithm and may be undertaken as future work. It is also pointed out that camera psf cannot be characterized with adequate accuracy using simple

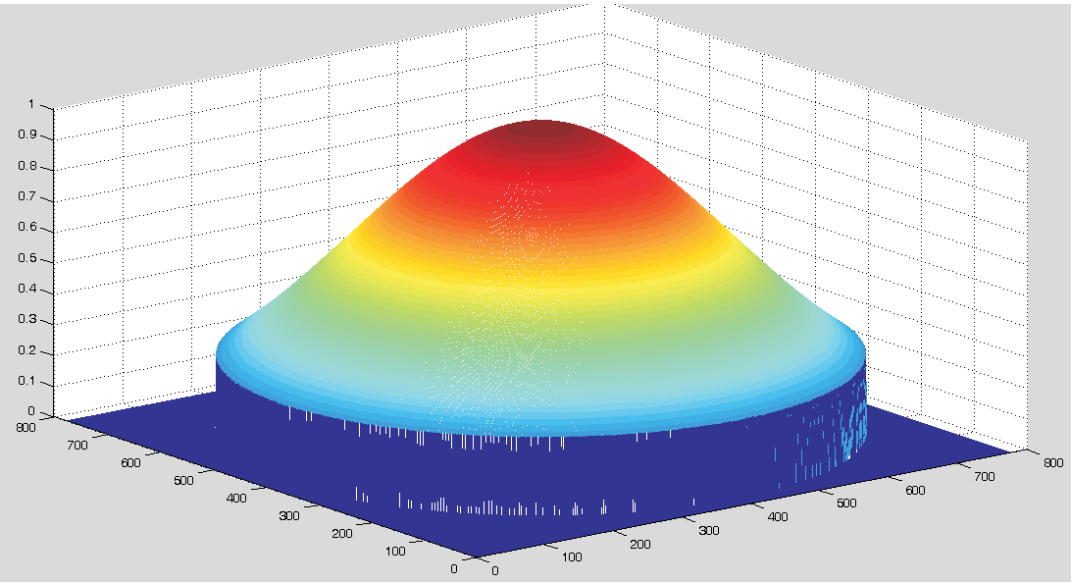

Figure 5.11. Gaussian aperture for R=0.00625.

mathematical models such as Gaussian or cylindrical functions. A better technique would be to measure experimentally the actual psf of the camera for different degrees of image blur using the measured data and then model this psf in the SAR 2-D aperture synthesis signal processing.

5.3 Conclusion

This research work utilized the inherent focusing ability of the SAR 2-D aperture synthesis algorithm, a two-dimensional variant of the $\omega - k$ algorithm, to refocus out-of-focus optical images. Refocusing of images may be necessary in machine vision as a preprocessing step before edge detection or image segmentation. The SAR 2-D aperture synthesis algorithm generates a complex amplitude distribution and psf similar to Fraunhofer diffraction distribution and psf as seen in Fourier optics. The matched filter in the SAR 2-D aperture synthesis algorithm has a focus-in-altitude interpretation and may be varied to increase or decrease the radius of blur associated with a particular psf. This paper demonstrated focusing of a simple line object $L = (1 : x = y - 64 \leq x \leq 63, -64 \leq y \leq 63)$. Although a rectangular aperture was used in the refocusing process, other apertures may also

be used such as circular or Gaussian. Moreover, actual psf of a camera system may also be accurately modeled in the refocusing algorithm.

CHAPTER 6

LATE SEASON RURAL LAND COVER ESTIMATION WITH POLARIMETRIC SAR INTENSITY PIXEL BLOCKS AND σ-TREE STRUCTURED NEAR NEIGHBOR CLASSIFIERS [7]

6.1 Introduction

SAR image classification for late season rural land cover estimation is investigated. A novel, tree structured, nearest neighbor–like classifier is applied to polarimetric SAR intensity image pixel blocks. The novel tree structure, called a σ–tree, is generated by an ordered summation of unweighted template refinements. Computation and memory costs of a σ–tree classifier grow linearly. The reduced costs of σ–tree classifiers are obtained with the trade–off of a guarantee of nearest neighbor mappings. Causal–anti–causal refinement template design methods, combined with causal multiple stage search engine structures, are shown to yield sequential search decisions that are acceptably near neighbor mappings. The performance of a σ–tree classifier is demonstrated for rural land cover estimation with detected polarimetric C–band AirSAR pixel data. Experiments are conducted on various polarization/pixel block size combinations to evaluate the relative utility of spatial–only, polarimetric–only, and combined spatial/polarimetric classifier inputs.

Nearest neighbor classifier implementation costs, in term of required memory and computational resources, grow in proportion to the number of exemplars available as pattern matching templates. Conventional tree structured nearest neighbor classifiers reduce computation, but increase memory requirements. This research investigates a novel tree structure called a σ–tree that simultaneously reduces both computation and memory requirements. This tree structure is derived from a collection of multiple stage successive approximation templates.

Data processing can often be formulated in terms of "successive refinement," "incremental refinement" or "approximate signal processing" [65]. A progressive formulation

of data processing and data representation allows for the possibility of trading accuracy or optimality of results for the consumption of resources such as system cost and complexity [66]. Successive approximation source codes provide an architectural framework and strategy for image content classification [67], and is at the heart of the σ–tree concept. The type of successive approximation source code proposed here for data classification is based on direct sum data structures [68]. This template–based classifier search engine uses direct sum structures for building efficient, data–adaptive, reduced–degree–of–freedom digital representations of target class exemplars. In this research, σ–tree classifiers are applied in the pixel space of detected polarimetric synthetic radar images for late season (November in southeastern United States) rural land use estimation.

The primary purpose of this research is to introduce and investigate the utility of the direct sum form of data representation in SAR image classification problems. C–band AirSAR data sets of opportunity (images and ground truth) provide us late season crop classification as the corresponding application–of–opportunity. The work of Frate, *et al.* [69] addresses crop classification with polarimetric C–band AirSAR data for crop classification. Their image sets were obtained in the early to mid stage of growth (June). They examined full complexity neural–networks, pruned complexity neural–networks, and maximum likelihood algorithms. Their data analysis show that polarimetrics should be a key discriminator, and they are able to achieve good classification results with field–based (not pixel–based) polarimetric signature classification. Their proven expectation is that polarimetrics is a key discriminator for early to mid season growth stage crops. This is due to crop canopy and ground bounce interactions, especially in cross polarizations. However, in late season classification problems, the crop canopy is usually sparse or absent, so a question addressed in this research is can spatial extension of the classifier's input space compensate for lack of polarimetric discriminators in late season land cover estimation?

Our classifier is a pixel based classifier that runs a sliding window through a polarimetric SAR intensity (detected) pixel image, and extracts multiple layered snippets for

classification. The stride of the sliding window is one pixel in both x and y directions. For example, if a block size of 9×9 is used for classification, the sliding window moves just one pixel to the right for the next block (or starts at the head of the next row if the end of a row is reached). This allows the classifier to assign a class label to every pixel. The stride of the sliding window can be increased to reduce the runtime of the σ–tree classifier.

Experiments are conducted for three cases: 1) with combined polarimetric/spatial blocks with 9×9 pixels and HH, VV and VH layers, 2) with polarimetric–only blocks with single pixel spatial extent and HH, VV and VH layers, and 3) with spatial–only blocks with 9×9 pixels of a single AirSAR "total power" (TP) layer. Results show that inclusion of both polarimetric and spatial information gives good classification results for feature classes of 1) unharvested cotton (85% correct), 2) cut corn stubble / picked and cut cotton / plowed areas (90% correct), 3) pasture and dried soybean areas (99% correct), 4) young pine stands (74% correct), 5) mature pine stands (100% correct) and 6) a catch–all–else "other" class. The system is less successful separating unpicked cotton with foliage (79%) from unpicked defoliated cotton (52%), and separating dried soybeans (67%) from pasture (47%). Experiments show that the inclusion of spatial content into the σ–tree classifier's input space is helpful for all classes, and that the inclusion of polarimetric content is useful for small plant ground cover (unharvested cotton and young pine trees).

The rest of this chapter is outlined as follows. Section 6.2 introduces the mathematical structure of σ–tree classifiers. Section 6.3 describes the σ–tree classification decision rules. Section 6.4 discusses the Parzen–window like structure of σ–tree classifiers. Section 6.5 describes the SAR experiments. Section 6.6 presents conclusions, and Section 6.7 is an appendix that gives a σ–tree design algorithm.

6.2 σ-Tree Near Neighbor Classifiers

Let $\mathbf{x_0}$ represent a subblock or tile of a possibly multilayered SAR image that contains n pixels. Let $\{\mathbf{x}_0(l), l = 1, 2, \ldots, L\}$ be a collection of SAR image tiles that contain examples

of a land cover type of interest. Conceptually, the elements of $\{\mathbf{x}_0(l)\}$ can serve as exemplars in a nearest neighbor classifier with the asymptotic risk of the classifier never being worst than twice the Bayes risk as L becomes large [70]. Practically, this approach is not feasible for large n because the memory and computational capacity required to utilize $\{\mathbf{x}_0(l)\}$ as a set of nearest neighbor exemplars grows with L.

This research uses a set $\{\hat{\mathbf{x}}_0(\mathbf{i})\}$ of structured examplars formed from direct summations [68] that approximate the $\{\mathbf{x}_0(l)\}$ in a novel type of "near" (not necessarily "nearest") neighbor classifier [67]. The set of directly summed templates $\{\hat{\mathbf{x}}_0(\mathbf{i})\}$ is not stored statically, but its elements are built, as required, "on-the-fly" from additive refinement or residual template sets. A tree structure called a "σ–tree" can be associated with each ordered permutation of the collection of residual template sets [71]. Hence the name: σ–tree classifier ("σ" indicates "summation") [72].

A σ–tree classifier consists of a collection of *residual template sets* $\{\mathbf{y}_p(i_p)\}$, with the *level* or *stage index* $p \in \{1, \cdots, P\}$ and the *stage template index* $i_p \in Z_M = \{0, 1, \ldots, M-1\}$. An algorithm for generating residual template sets is described in the appendix of this chapter. Using a local nearest neighbor rule at each stage, the σ–tree near neighbor classifier searches the sets of residual templates $\{\mathbf{y}_p(i_p)\}$ in a sequential manner ($p = 1, 2, \ldots, P$) and successively adds the selected stage refinement template, on–the–fly, to form a *direct sum template*

$$\hat{\mathbf{x}}_0(\mathbf{i}_P) = \sum_{p=1}^{P} \mathbf{y}_p(i_p) \tag{6.1}$$

where i_p is the index of the selected nearest neighbor template at the pth stage, and where a composite P–tuple index $\mathbf{i}_P = (i_1 i_2 \cdots i_P)$ indicates the selected terminating node $\hat{\mathbf{x}}_0(\mathbf{i}_P)$ of the σ–tree. The composite P–tuple index $\mathbf{i}_P$ belongs to the P–element cartesian product of M–ary index sets,

$$\mathbf{i}_P \in \underbrace{Z_M \times Z_M \times \cdots \times Z_M}_{P \text{ elements}} = Z_M^P \tag{6.2}$$

Tree structured nearest neighbor classifiers are a standard approach in nonparametric

decision systems. Standard tree structures reduce computation costs at the expense of an increase in memory costs. The advantage of σ–tree structures over conventional tree structures is that *both* memory and computation are reduced. The baseline implementation costs of an n–dimensional σ–tree classifier is specified by two parameters, M (the number of branches at each node of the σ–tree = the number of stage templates) and P (the number of levels in the σ–tree = the number of stage residual sets). Since the descendant nodes that branch from each node at a given level of the σ–tree are constructed by additive template refinements, each selected from a common, level–specific, residual refinement template set, the computation and memory required for σ–tree template storage and template search is proportional to

$$n \times M \times P \tag{6.3}$$

This cost function indicates that computation and memory grow linearly with classifier dimensionality n, grow linearly with branch multiplicity M, and grow linearly with the number of tree levels P. Compare this low rate of growth in costs to the exponential rate of growth of the number of σ–tree terminating nodes

$$\hat{L} = M^P \tag{6.4}$$

Each of these is a possible outcome in a near neighbor search in the σ–tree classifier. Practically, there can be many ($\hat{L} \gg L$) terminating nodes in the σ–tree structure, where one or more $\{\hat{\mathbf{x}}_0(\mathbf{i})\}$ are near neighbors of each $\{\mathbf{x}_0(l)\}$.

6.2.1 Comparison with Basis Function Representations

The direct sum template formulation

$$\hat{\mathbf{x}}_0(\mathbf{i}_P) = \sum_{p=1}^{P} \mathbf{y}_p(i_p) \tag{6.5}$$

is similar to a standard basis function synthesis system:

$$\hat{\mathbf{x}}_0(\mathbf{\Gamma}_n) = \sum_{j=1}^{n} \gamma_j \phi_j \tag{6.6}$$

where $\Gamma_n = (\gamma_1, \ldots, \gamma_n)$ is a vector of basis weights. The differences between the two systems is the direct sum template system is nonlinear, i.e., a functional form $\mathbf{y}_p(i_p)$ instead of a linear form $i_p\mathbf{y}_p$, and P is not upper bounded by the dimensionality of the $\mathbf{x}_0$. Thus, (6.5) gives a single mathematical structure for data representations that may be under–determined ($P < n$), critically determined ($P = n$), or over–determined ($P > n$). This span from under, critical and over is all within a common block data representation architecture, and is a key factor in the ability to form successive approximations within and across feature subspaces, and does not force a system to acquire successive approximations by only adding basis from orthogonal subspaces. The direct sum formulation also differs from basis function synthesis system in that $i_p \in Z_M$ (compared with $\gamma_n \in \Re^n$) – this is one source of implementation efficiency.

6.2.2 Comparisons with other Classifiers

A σ–tree classifier essentially performs an unsupervised clustering of training data, and uses the dominant label of the training data within each cluster to assign labels to new data blocks. This is a standard approach in pattern recognition. For a recent example, Kersten, *et al*. [73] explore the use of different distance metrics in both fuzzy clustering and expectation maximum clustering algorithms for SAR images. Their work explores the use of both complex pixel and intensity pixel information, and they show that l_p norms may be less effective in clustering because an l_p norm will allocate new clusters by splitting up high–energy clusters. The risk of having clusters inappropriately "split" is due in part to the use of relatively small number of cluster centers–which is not a concern with large (many stage) σ–tree cluster sets under a l_2 norm. A high number of cluster centers is possible in practice with σ–trees because of the computational and memory efficiency of imposed structural constraint. Unlike support vector machines, which seek to populate a decision space with a few vectors near decision boundaries [74], a σ–tree classifier populates the decision space with many cluster centroids. These centroids are dense in probable regions and sparse in less probable regions of the decision space [75]. Furthermore, the practical achievement of

high dimensionality in the σ–tree classifier allows the asymptotic equipartition property of high dimension [76] to mitigate the constraints on cluster exemplar placement imposed by the structure of the σ–tree.

6.2.3 σ-Tree Nearest Neighbor Decisions

The functional operation of a P–stage, sequential search, σ–tree classifier is indicated by $\sigma_P(\mathbf{x}_0) = \hat{\mathbf{x}}_0(\mathbf{i}_P)$. The pth stage intermediate decision of the σ–tree sequential search engine is $\sigma_p(\mathbf{x}_p) = \hat{\mathbf{x}}_0(\mathbf{i}_p)$, where the input to the pth stage nearest neighbor search engine is the pth stage *causal residual*

$$\begin{aligned} \mathbf{x}_p &= \mathbf{x}_0 - \sigma_{p-1}(\mathbf{x}_{p-1}) \\ &= \mathbf{x}_0 - \hat{\mathbf{x}}_0(\mathbf{i}_{p-1}) \\ &= \mathbf{x}_0 - \sum_{\rho=1}^{p-1} \mathbf{y}_\rho(i_\rho) \end{aligned} \tag{6.7}$$

for $p \in \{2, \ldots, P\}$ and where $\mathbf{i}_{p-1}$ is a partial P–tuple index.

The σ–tree near–neighbor search engine mapping $\sigma(\cdot)$ can be functionally decomposed into an *indexing* function $I(\cdot)$ and a *template lookup* function $T(\cdot)$, such that $\sigma(\cdot) = T(I(\cdot))$. The sequence of σ–tree search engines is embedded in that the composite indices output by the stage search engines are nested in this way

$$\begin{aligned} \mathbf{i}_1 &= (I_1(\mathbf{x}_0)) \\ \mathbf{i}_2 &= (I_2(\mathbf{x}_1), \mathbf{i}_1) \\ &\vdots \\ \mathbf{i}_P &= (I_P(\mathbf{x}_{P-1}), \mathbf{i}_{P-1}) \end{aligned} \tag{6.8}$$

A successive refinement sequence is formed by the corresponding template lookup functions

$$\begin{aligned} T_1(\mathbf{i}_1) &= T_1(i_1) \\ T_2(\mathbf{i}_2) &= T_1(i_1) + T_2(i_2) \\ &\vdots \\ T_p\left(\mathbf{i}_p\right) &= T_1(i_1) + T_2(i_2) + \cdots + T_P(i_P) \\ &= \mathbf{y}_1(i_1) + \mathbf{y}_2(i_2) + \cdots + \mathbf{y}_P(i_P) \end{aligned} \tag{6.9}$$

thus yielding the direct sum of (6.1).

Given a distance metric $d(\cdot)$, such as squared error, each stage search engine makes a local nearest neighbor decision between the causal residual input $\mathbf{x}_p$ and its stage's residual template set:

$$\sigma_p(\mathbf{x}_p) = \hat{\mathbf{x}}_0(i_p, \mathbf{i}_{p-1}) \text{ iff } d\left(\mathbf{x}_p, y_p(i_p)\right) \leq d\left(\mathbf{x}_p, y_p(j_p)\right) \tag{6.10}$$

for all $j_p \in Z_M$, and where an arbitrary rule may be used in case of ties. Although a nearest neighbor rule is used locally at each stage to identify the best i_p, there is no guarantee with this classification rule that the collective decisions represented by $\mathbf{i}_p = (i_p, \mathbf{i}_{p-1})$ provide the nearest possible $\hat{\mathbf{x}}_0(\mathbf{i}_p)$ for a given $\mathbf{x}_0$. Hence, the description of this system as a "near" neighbor classifier, not a "nearest" neighbor classifier. That is, even if (6.10) is satisfied for all p for a given $\mathbf{x}_0$, it does not necessarily follow that

$$d\left(\mathbf{x}_0, \hat{\mathbf{x}}_0(\mathbf{i}_P)\right) \leq d\left(\mathbf{x}_0, \hat{\mathbf{x}}_0(\mathbf{j}_P)\right) \tag{6.11}$$

for all $\mathbf{j}_P \in Z_M^P$.

6.2.4 σ-Tree Residual Template Design

A collection of SAR image tiles $\{\mathbf{x}_0(l)\}$ is used as a training set to design the classifier's stage residual template sets $\{\mathbf{y}_p(i_p)\}$, and by association, the set $\{\hat{\mathbf{x}}_0(\mathbf{i}_P)\}$. The design objective is to minimize the overall empirical training set distortion

$$\sum_l d\left(\mathbf{x}_0(l), \hat{\mathbf{x}}_0(\mathbf{i}_P)\right) = \sum_l d\left(\mathbf{x}_0(l), \sigma(\mathbf{x}_0(l))\right)) \tag{6.12}$$

where enough training samples are used to provide a good approximation of source statistics to allow the template set to approach the overall objective of minimization of the expected distortion

$$E\left\{d\left(\mathbf{x}_0, \sigma_P(\mathbf{x}_0)\right)\right\} \tag{6.13}$$

for the underlying data source distribution $f(\mathbf{x}_0)$ of the SAR block pixel intensities, which is assumed to be stationary and ergodic. Details of the residual template design process are given in appendix at the end of this chapter.

6.2.5 Template Design Algorithm

Using methods presented in [77] for designing residual template sets for multiple stage vector quantizers, the empirical training set distortion (6.12) can be made as small as desired by increasing the number of stages produced by the design process. A design objective obtained by the methods of [77] is that the sequence of reconstructions provides

$$E\left\{d\left(\mathbf{x}_0, \sigma_p(\mathbf{x}_p)\right)\right\} < E\left\{d\left(\mathbf{x}_0, \sigma_{p-1}(\mathbf{x}_{p-1})\right)\right\} \tag{6.14}$$

for $p = 2, \ldots, P$. Thus the sequence of template functions provide a successive refinement with respect to expected source distortion, given sufficiently large training sets. Note there is no guarantee that deterministic successive approximation will be achieved, i.e., it does not follow from (6.14) that the following is satisfied:

$$d\left(\mathbf{x}_0, \sigma_p(\mathbf{x}_p)\right) < d\left(\mathbf{x}_0, \sigma_{p-1}(\mathbf{x}_{p-1})\right) \tag{6.15}$$

for each and every member of $\{\mathbf{x}_0(l)\}$. That is, successive refinement is only achieved in a stochastic sense.

6.2.6 Curse of Dimensionality and Overtraining

The efficiencies of σ–trees allow classifiers of SAR image blocks with many pixels to be practically implemented. Our SAR pixel classification experiments use fused negative and positive versions of polarimetric SAR image blocks of 6 layers (positive HH, VV, HV; and

negative HH, VV, HV), and a spatial block size of up to 9×9 pixels. Hence, the largest σ–tree classifier feature space dimensionality tested in this paper is 486 dimensions.

Two problems often plague classifiers with high dimensionality [78]:

1. Challenge of generating a large number of templates with clustering algorithms with limited training data.

2. Challenge of classifier robustness when data are encountered that are not well represented by a limited amount of high–dimensional training data.

6.2.6.1 The Curse of Dimensionality in the Design Phase

The template generation design phase problem is related to the degrees–of–freedom that must be dealt with when training a classifier. Often, the number of degrees–of–freedom expands exponentially as the dimensionality of the classifier increases. This is where σ–trees have an advantage, the number of terminating nodes in the σ–tree grow as $\hat{L} = M^P$, but the number of degrees–of–freedom of each stage of the σ–tree structure grows only linearly as nM.

Conventional nearest neighbor classification systems require minimum training set sizes on the order of 10–100 training vectors for every template [79], [80]. The use of multiple stages of small sets of templates reduces the amount of training data required to generate templates for high dimensional feature vectors. The design process of [77] requires that only one stage of the direct sum templates be generated (or improved) at a time – thus, the entire training set need only be partitioned between the small number of additive successive refinement basis functions that exist at a single stage (a number that typically ranges from 2 to 16 in our research). Thus, to design a σ–tree with 16 stage residual templates (16 branches at each tree node), the rule of thumb would require about 100×16 training examples. A training set size of 17,681 SAR blocks is used in the experiments of this chapter.

6.2.6.2 *The Curse of Dimensionality in the Run Phase*

There are limits to how much information can be gleaned for a classification process from limited training data, even if the design phase version of the curse of high dimension is avoided via multiple stage structure. A potential problem with a σ–tree structure is that not all of the combinatoric direct sum exemplars may be utilized in the classification process, especially if large numbers of refinement stages are generated. This is related to the over–training problem. This problem can be dealt with by limiting the number of σ–tree levels that are used during classification processing. A stage depth decision rule restricts the search for near distance decisions over a subset of σ–tree stages. That is, instead of searches over the stages indexed by p with $p \in \{1, \ldots, P\}$, the search is performed over only a subset of stages $p \in \{P_{min}, \ldots, P_{max}\}$ with $1 \leq P_{min}$ and $P_{max} \leq P$. This restriction appears useful for reducing false alarm rates, and allows control over classifications with over–trained templates (those stages deep in the multiple stage system). In this research the number of allowed stages starts at stage one, and is limited to no more than eight stages. The sequential search process may terminate before the eighth stage if no stage templates of the next stage provide a refined representation of the input SAR block. That is, failure to satisfy (6.15) is used as a "stop searching" criteria.

6.3 σ-Tree Classifier Decision Rules

Two σ–tree decision rules are employed. First, a minimum distance (near neighbor) rules for template similarity comparisons; and second, a Parzen window–like maximum posterior probability rule for land cover class assignments.

6.3.1 Near Neighbor Normalized Distance Decision Rules

A normalized mean–squared distance measure called a *signal–to–mismatch–noise ratio* (indicated by SNR_{mm}) is used to quantify "nearness." This metric is defined as

$$SNR_{mm} = 10 \log \left(\frac{\sum_{j=1}^{n} \left(x_j - \hat{x}_j(\mathbf{i}) \right)^2}{\sum_{j=1}^{n} x_j^2} \right) \tag{6.16}$$

where x_j is the jth element of the n–tuple data vectors. There are two different conceptual approaches for σ–tree classification systems. The first uses multiple σ–trees, the other uses only one.

6.3.1.1 Multiple σ-Tree Systems

A supervised, labeled set of training data are separated into multiple sub–training sets, where each sub–training set is used to design a σ–tree specifically for that class label. The classification system searches each σ–tree to find it's best near neighbor mapping and it's associated minimum distance. One possible classification decision rule is to choose the class label of the decision tree that gives overall minimum distance.

6.3.1.2 Single σ-Tree System

A mixed, labeled training set is used to design a single σ–tree. The labels of the best near neighbor mappings are used for posterior probability estimation and class label assignments. This is analogous to a conventional nearest neighbor or k–nearest neighbor, tree–structured classification system.

There is a drawback with the single σ–tree approach–increased implementation costs. Since labels of the terminating nodes are used in the single σ–tree system, the implementation costs of the σ–tree classifier are proportional to the training set size. (but not dependent on the dimensionality of the classifier). Thus this approach looses the linear cost growth characteristic, but does not require the design of post near neighbor mapping classification decision logic sometimes required to fuse a decision from multiple σ–tree classifiers. The second approach is utilized in this research.

6.3.2 Bayesian Decision Rules

Let $p(\omega_j|\mathbf{x}_0)$ be the posterior probability of class ω_j given observation of a data block $\mathbf{x}_0$. Some nearest neighbor classifiers would find the training set exemplar $\mathbf{x}_0(l)$ that $\mathbf{x}_0$ is closest to and use either the label of $\mathbf{x}_0(l)$ for a classification decision, or for Bayesian estimation would use a stored value $p(\mathbf{x}_0(l)|\omega_j)$ and a prior probability estimate $p(\mathbf{x}_0)$ to estimate the

posterior $p(\omega_j|\mathbf{x}_0)$.

The σ–tree classifier of this research uses a variation on this theme. A near neighbor $\hat{\mathbf{x}}_0(\mathbf{i}_p)$ of $\mathbf{x}_0(l)$ is first discovered by the σ–tree sequential search engine. The class label's relative frequency counts of the subset of $\mathbf{x}_0(l)$ mapped to $\hat{\mathbf{x}}_0(\mathbf{i}_p)$ by the σ–tree design process are used to generate posterior estimates $p(\omega_j|\hat{\mathbf{x}}_0(\mathbf{i}_p))$, and the class with the largest posterior probability is assigned. For example, let $p(\omega_j|\mathbf{i}_p) = p(\omega_j|\hat{\mathbf{x}}_0(\mathbf{i}_p))$ be the posterior probability of class ω_j within the near neighbor region of $\hat{\mathbf{x}}(\mathbf{i}_p)$ where ω_j is the class label $j \in \{1, \ldots, J\}$ and $\mathbf{i}_p$ is the partial p–tuple index of a particular partial σ–tree exemplar $\hat{\mathbf{x}}_p$. The word "partial" is used in this context to emphasize that p may be less than P. (The posterior probabilities are not necessarily monotonically increasing with p.)

The σ–tree maximum posterior decision rule is to choose the class label ω_j^* and σ–tree depth p^* that maximizes

$$p\left(\omega_j^*|\mathbf{i}_{p^*}\right) = \arg\left\{\max_{(p,\omega_j)} \frac{p(\mathbf{i}_p|\omega_j)P(\omega_j)}{\sum_{j=1}^{J} p(\mathbf{i}_p|\omega_j)P(\omega_j)}\right\} \tag{6.17}$$

over $p \in \{1, \ldots, P\}$ and $\omega \in \{1, \ldots, J\}$, and with $P(\omega_j)$ the prior probability of class ω_j.

The maximum posterior probability (MAP) values can be estimated from the training data in a conventional manner [70]. Let $N(\mathbf{i}_p)$ be the number of training vectors in the Voronoi cell of σ–tree exemplar $\hat{\mathbf{x}}_0(\mathbf{i}_p)$. Let k_ω be the subset of this N exemplars that belong to class ω. Given equal prior probabilities over the class labels ω, the MAP estimate of $p(\omega|\mathbf{i}_p)$ is $k_\omega/N(\mathbf{i}_p)$.

6.4 Successive Refinement Parzen Windows

The multiple stage formulation of the σ–tree structure induces a sequentially refined partitioning (sub–clustering) of training data, and when combined with a near neighbor rule, induces a sequence of partition refinements of the classifier's input space. For example, the nearest neighbor regions of a the partial path σ–tree exemplars $\{\hat{\mathbf{x}}_0(\mathbf{i}_{p-1}i_p); i_p = 1, \ldots, M\}$ form an M–way partition of the nearest neighbor region of the σ–tree exemplar $\hat{\mathbf{x}}_0(\mathbf{i}_{p-1})$.

The progressive partition refinements of the classifier's input space $\mathbf{x}_0 \in \Re^n$ provides an opportunity for the design of a sequential Bayesian classification system with progressively refined (localized) near neighbor class estimates over progressively smaller Parzen–like windows (exemplar's Voronoi regions). When a σ–tree classifier is viewed as an estimator of class posterior class probability given an observation of $\mathbf{x}_0$, this progressive partition refinement structure of a σ–tree classifier allows a controlled trade–off between large window, smoothed Parzen probability estimates and small window, local estimates of posterior probabilities in high–dimensional decisions spaces. This progressive Bayesian Parzen windowing proceeds in lock step with pixel intensity successive approximations–both processes guided by the σ–tree structure.

6.5 SAR Pixel Data Experiments

6.5.1 Test Site and Land Cover Ground Truth

A multipolarization AirSAR image set of a rural area in south Georgia of the United States is used to assess the performance of σ–tree classification of SAR pixel data for rural land use estimation. The data were measured 1 November 1998. These data provide an opportunity to make assessments of land cover late in the growing season during harvesting and post–harvest fallow preparations. The crops and land cover present during ground truth collection were cotton in three harvest states (foliage–unpicked, defoliated–unpicked and defoliated–picked–cut), corn in two post harvest states (cut stubble and stubble plowed under), pasture, fallow fields, soybeans (dried/unpicked), pine plantations, and pine trees planted for regeneration. Figure 6.1 shows example images taken of land use during on–site ground truth assessments. Figure 6.2 shows the locations of ground truth sites of different land cover classes in the particular SAR image used in these experiments. Each field identified in the ground truth is known to contained only one type of the crop class or tree class of that truth label.

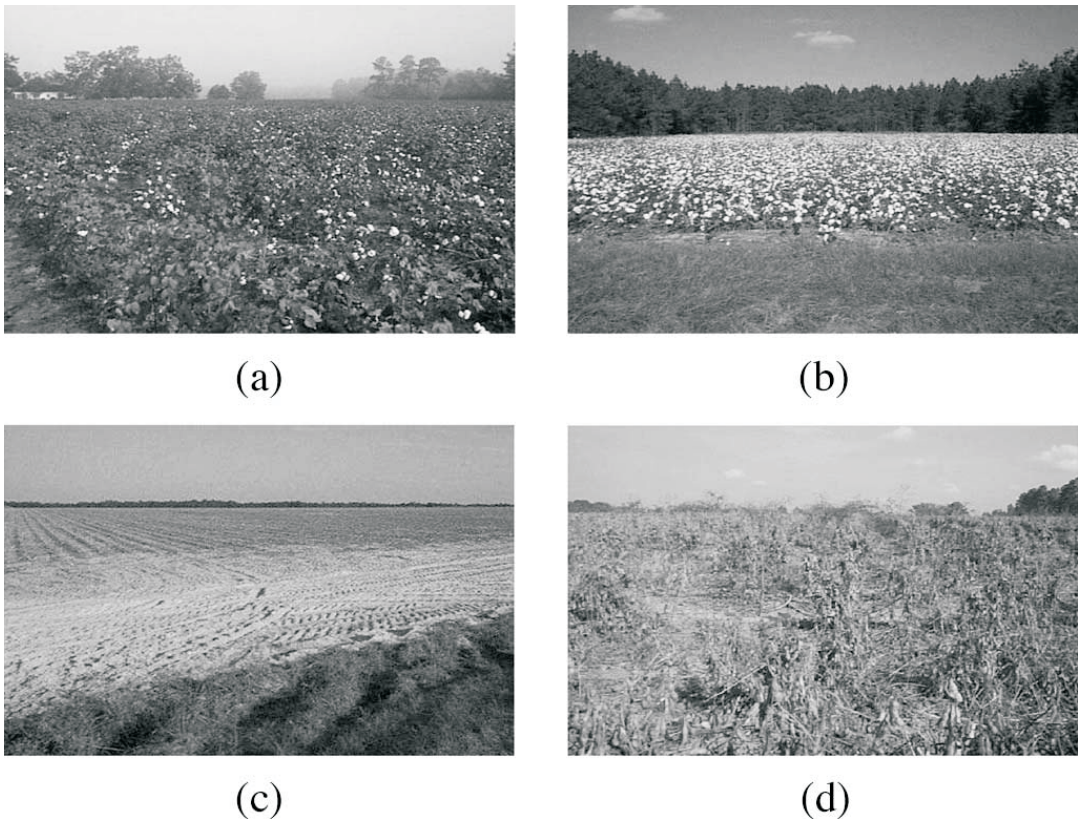

Figure 6.1. Examples of late season rural land use images taken during ground truth assessments. (a) Mature green cotton. (b) Defoliated cotton, unpicked. (c) Cotton harvested and cut. (d) Dry soybeans.

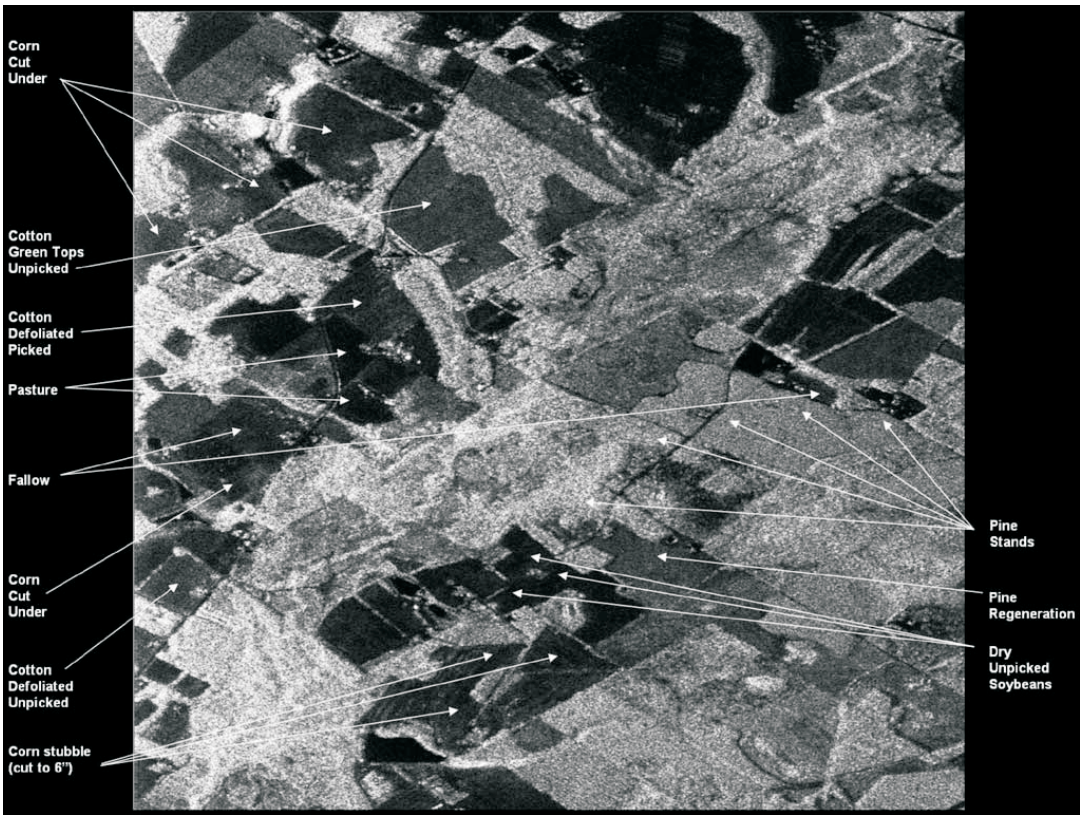

Figure 6.2. AirSAR image acquired 1 November 1998 near Alma, Georgia. Ground truth sites for land use classes shown by arrows.

6.5.2 AirSAR Training Data

This AirSAR data set was measured by a multiple polarization C–band radar and was focused to a resolution of about 1 meter in azimuth and 1.875 meters in range. The polarization layers of HH, HV and VV were fused into a multilayer SAR image set. A total power (TP) version of the scene was also measured and returned as a single layer SAR version of the scene.

A total of 17,618 image tiles of labeled training data were extracted from three polarimetric layers (HH, HV, VV) for both polarimetric–only and combined polarimetric/spatial experiments. Single layer image tiles were extracted from the same 17,618 training sample locations using only the total power layer (TP) for spatial–only classification experiments. The image tiles were expanded by including a negative version of the detected (magnitude) SAR image pixel blocks. The combined use of positive and negative pixel intensities provides a simple approach for image block energy normalization. Blocks of size $9 \times 9 \times 6 = 486$ pixels were extracted for the combined polarimetric/spatial experiments. Blocks of size $9 \times 9 \times 2 = 162$ pixels were extracted for the spatial–only experiments. Blocks of size $1 \times 1 \times 6 = 6$ pixels for the polarimetric–only experiments. Additional image tiles from unlabeled regions of the SAR image were extracted to form examples of a "other" label set not included in the known types of ground cover.

6.5.3 Classifier σ–Tree Parameters and Templates

A σ–tree was grown for each experiment (polarimetric/spatial, polarimetric–only and spatial–only) with the labeled AirSAR training set. Each stage of the σ–tree has 16 templates. A total of 8 stages were designed in each case with the design method described in the appendix. Hence, the set of possible near neighbors has $\hat{L} = 16^8$ elements to approximate, to one degree or another, the training set with $L = 17,618$ elements.

The different polarization layers of the σ–tree polarimetric/spatial template sets are shown in the first three images of Figure 6.3. The last of the four images in Figure 6.3 show the spatial–only total power (TP) σ–tree templates. All templates, except those of the

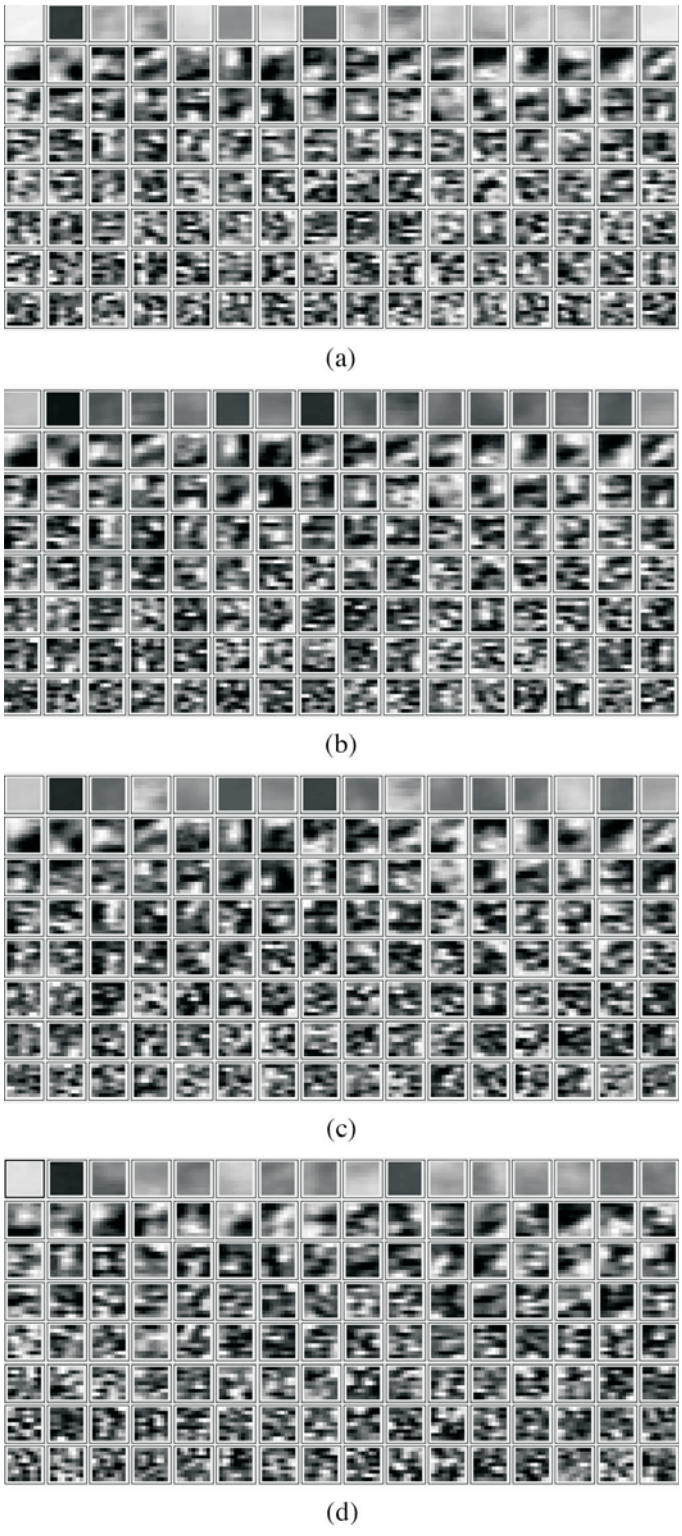

Figure 6.3. Two examples of eight additive successive refinement template sets (first three images show VV, VH and HH layers of the polarimetric/spatial σ–tree, the last shows the spatial–only total power σ–tree).

first stage, tend to have positive or negative sample values. The first stage template pixels are usually all positive amplitudes. The intensity levels of the refinement templates shown in Figure 6.3 have been normalized to better show texture detail. The actual intensity levels decrease with increasing stage index. Note that the spatial characteristics of the additive refinements progress from basically block mean values with some course structure, to increasing refinements of texture granularity. There is also significant polarimetric variability between the HH, HV and VV layers.

Shown in Figure 6.4 are four example σ–tree successive approximation sequences from the spatial–only experiment for a sample training block input from the corn stubble, cotton with foliage, pine and young pine classes. There are eight rows for each example that come from the eight residual stages of the σ–tree template set. The right most column contains the block–to–be–classified (repeated at each of the eight rows). The left most column is the best template greedily selected at each stage (shown with intensity normalization to show texture detail). The center column is the direct sum formed by adding the templates in the left column. Note the σ–tree classifier is able to provide a reasonable approximation of each input block, but does not seem to fully approximate the speckle content of the input block. (The negative version of the corn and cotton blocks are displayed because of the low energy returns from these land cover classes.) Further inspection shows that as the spatial extent of the blocks is reduced, the fidelity of the σ–tree approximation's of speckle content increases when the σ–tree parameters (number of stages and templates) are held fixed.

We note that the design process was interrupted at the eighth stage, but could have been permitted to progress until enough stages are generated that all 17,618 training blocks are represented with an arbitrarily high degree of intensity fidelity. Although this is possible, it leads to a severely overtrained classifier. But from another point of view, the σ–tree classifier could be viewed as an index generation system capable of providing unique content driven indexes $\mathbf{i}_P$ for all image tiles contained in a training set or data warehouse, regardless

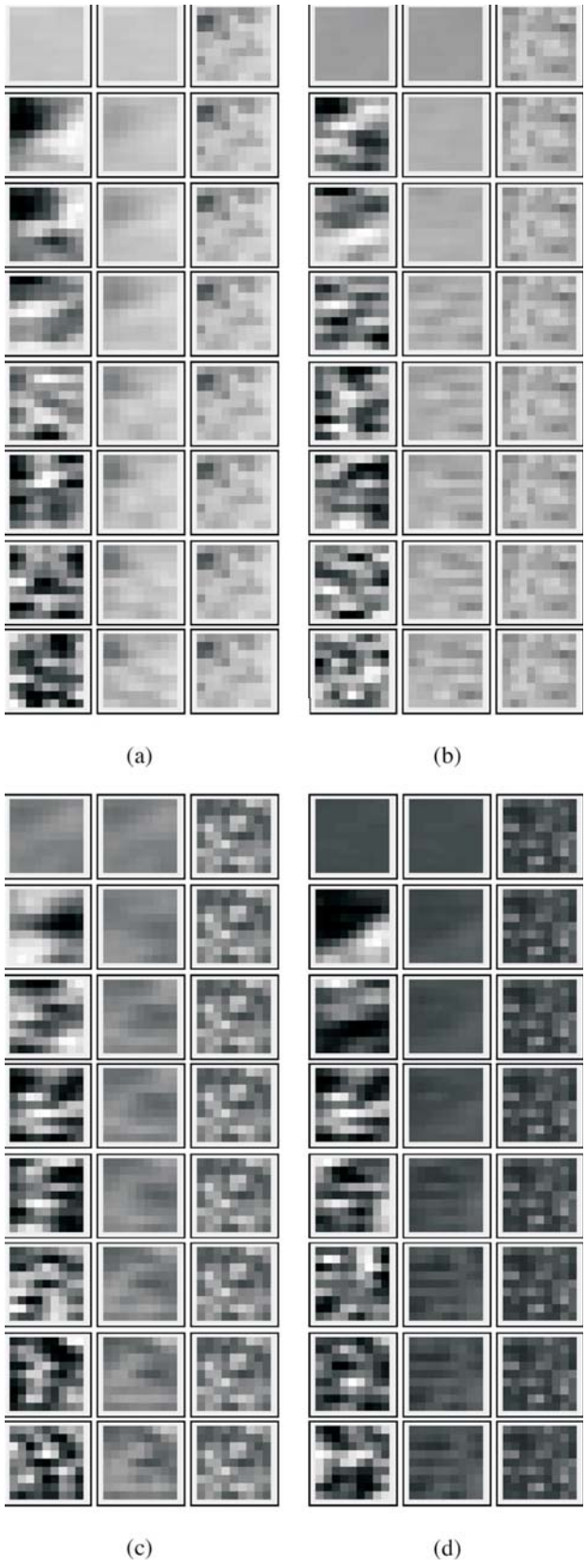

Figure 6.4. Example direct sum successive approximations. (Corn stubble. (b) Cotton with foliage. (c) Pine. (d) Young pine.)

of the number of examples in the training set. This technical capacity may have application in a number of image inventory and data mining applications [81], [82], [83], [84].

6.5.4 Accuracy Assessment

Classification experiments were performed using sequestered testing data not used for training. The test data were extracted from the same fields of the training data, but were not coincident with the training examples. Although this is not the most desirable separation of training and testing data, it is reasonable approach due to limited SAR data.

A error (confusion) matrix is used to assess the classification error and specify producer's accuracy and user's accuracy [85]. The probability of a reference pixel being correctly classified is the producer's accuracy, i.e., a measure of omission error. This is the number of pixels correctly classified as a land cover class divided by the total number of reference pixels for the class. The probability that a pixel classified in the image is really that land cover class is the user's accuracy, and this indicates the reliability of the classifier. The user's accuracy is calculated as the number of pixels correctly classified as a class divided by the total number of pixels that were assigned in that land cover class.

The classification results are shown in Tables 6.1–6.4, and a detection map from the polarimetric/spatial σ–tree classifier is shown in Figure 6.5.

The user's accuracy level for unharvested cotton with foliage is 79 percent, and drops to about 52 percent when defoliated but unpicked. These two classes are often confused, but when viewed as a superclass of "unpicked cotton," the user's accuracy is about 85 percent.

The user's accuracy levels for picked and cut cotton, fallow fields, and corn plowed over are in the range of 20 to 37 percent. The accuracy level for corn stubble is about 58 percent. All of these classes are often confused with each other. When viewed as a superclass of "harvested fields," the producer's and user's accuracy for the composite superclass is about 90 percent.

The user's accuracy level for pasture is about 47 percent. The user's accuracy level for dried, unharvested soybeans is about 67 percent. These two classes are often confused.

When viewed as a superclass of "grassy fields," the user accuracy is 99 percent.

The user's accuracy level for young pine trees is 81 percent for the producer, and 74 percent for the user. For mature pine trees these numbers change to 71 percent for the producer, and 100 percent for the user.

The classification results obtained with only polarimetric, single pixel inputs is shown in Table 6.3. There is a significant drop of about 15 to 60 percent in the user accuracy levels when spatial information is not provided to the σ–tree classifier.

The classification results obtained with only spatial, total power pixel inputs are shown in Table 6.4. The classes of unpicked cotton and young pine stands have a user accuracy drop by 10 to 14 percent. The other classes do not change significantly.

6.6 Conclusion

The σ–tree classifier has been demonstrated as a feasible and practical approach to SAR pixel data classification for rather specific target classes as those in late season rural land use estimation. These results indicate that the polarimetric/spatial σ–tree classifier is able to separate the C–band radar data into five late season land use classes: unpicked cotton, harvested fields, grassy fields, young pine stands and mature pine stands with an average user's specificity estimated to be about 90 percent, and to be no lower than about 74 percent. There is no significant loss in classifier performance for the harvested fields, grassy fields and mature pines when polarimetric information is not available. This is believed to be due to the lack of ground–canopy polarimetric interaction for these land use classes. Spatial inputs to a σ–tree classifier are required to segment these classes. On the other hand, loss of polarimetric information from spatial blocks of unpicked cotton and young pine stands significantly degrades classifier performance. This is due to the significant ground–canopy polarimetric interactions for these land cover classes.

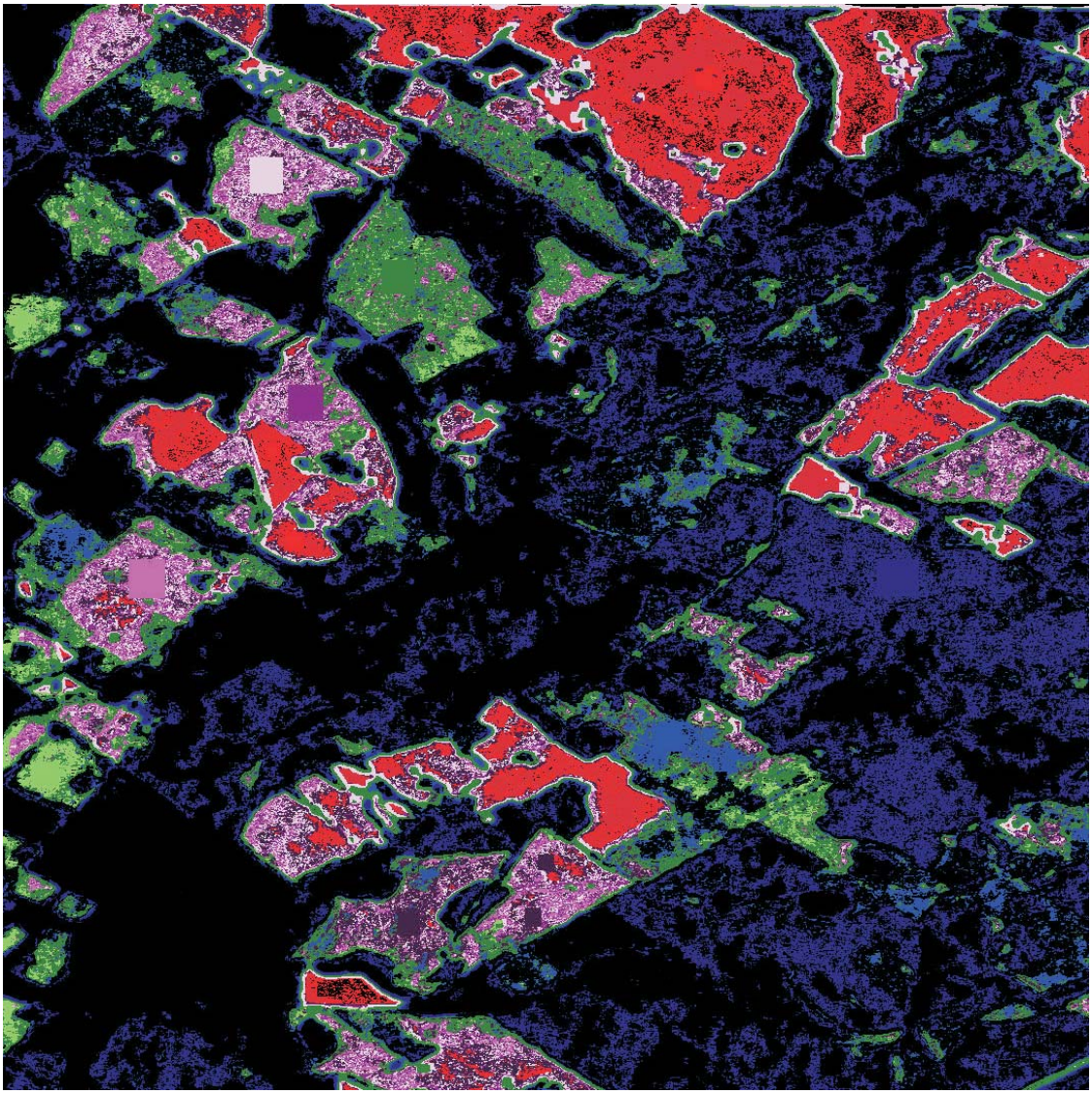

Figure 6.5. Classification map produced by the polarimetric/spatial σ–tree classifier. Grey scale colormap class code: black="other" class, darkest gray=pine, darker gray=young pine, gray=fallow/cut cotton/cut corn, lighter gray=unharvested cotton, white=pasture/dried soybean.

Table 6.1. Multipol AirSAR 9x9 Pixel Block Rural Land Use Classification Accuracy

Class Name	Producer's Accuracy	User's Accuracy
Cotton, Green, Unpicked	73.88%	78.84%
Cotton, Defoliated, Unpicked	69.51%	51.71%
Cotton, Defoliated, Picked	24.99%	30.04%
Fallow Fields	30.68%	19.85%
Corn, Plowed Under	32.72%	36.81%
Corn, 6" Stubble	54.52%	57.56%
Pasture	48.84%	47.14%
Soybeans, Dry, Unpicked	56.90%	67.12%
Young Pine Stands	80.76%	73.97%
Mature Pine Stands	70.64%	100.00%

Table 6.2. Multipol AirSAR 9x9 Pixel Block Rural Land Use Classification Accuracy

Composite Class Name	Producer's Accuracy	User's Accuracy
Unpicked Cotton	83.73%	84.83%
Harvested Fields	90.96%	90.38%
Grassy Fields	92.00%	98.99%
Young Pine Stands	80.76%	73.97%
Mature Pine Stands	70.64%	100.00%

Table 6.3. Multipol AirSAR 1x1 Pixel Block Rural Land Use Classification Accuracy

Composite Class Name	Producer's Accuracy	User's Accuracy
Unpicked Cotton	37.59%	42.11%
Harvested Fields	58.54%	61.63%
Grassy Fields	60.82%	63.41%
Young Pine Stands	24.94%	14.38%
Mature Pine Stands	37.69%	85.33%

Table 6.4. Total Power AirSAR 9x9 Pixel Block Rural Land Use Classification Accuracy

Composite Class Name	Producer's Accuracy	User's Accuracy
Unpicked Cotton	78.90%	74.43%
Harvested Fields	88.51%	89.46%
Grassy Fields	89.86%	99.59%
Young Pine Stands	61.34%	60.62%
Mature Pine Stands	67.77%	100.00%

6.7 Appendix: Design Algorithm

As described in ([77] p. 238), two different, but closely related residual template sets are generated during the design process to form a single σ–tree. One residual template set, called the encoder set, is used to design greedy, stage–sequential nearest neighbor mappings. The other residual template set, called the decoder set, is designed to satisfy a non–causal (non–greedy) joint optimality condition across all decoder stage template sets. Only the encoder set is used in the runtime of the σ–tree classifier. The decoder set is discarded once the design process is completed.

Two interlaced fixed point descent updates are used to design the σ–tree residual template sets. One fixed point process (called the outer process) is used to improve the sequential search performance of the encoder stage sets by testing the use of newly designed decoder stage sets in a candidate encoder to see if sequential search performance is improved. These new decoder stage sets satisfy a causal–anti–causal residual centroid condition (a condition necessary for non–greedy minimum mean squared error approximations formed from direct sum template sets [68]). A joint optimization of the decoder stage sets occurs in an inner Gauss–Sidel descent process driven sufficiently near a fixed point.

The σ–trees of this chapter, as described in ([77] p. 251), use a Type I variable block rate exit strategy in the sequential search encoding of classifier input blocks. A Type II

(variable stage entry strategy) is not required here because the normalization procedure of combining negative and positive versions of pixel blocks into a composite block causes all blocks to have the same mean level. If there is no residual template in the current encoder stage that provides a refined representation, the σ–tree search process for that input block is terminated. If at least one residual template stage provides a refined representation, then maximum *a posteriori* classification proceeds for that input block based on the utilized subset of residual template stages.

CHAPTER 7

CONCLUSION AND FURTHER RESEARCH

7.1 Conclusion

The major contribution of this research is the development of a fast imaging method for circular aperture synthesis. This method should prove to be a powerful tool for information processing in surveillance and reconnaissance radar systems. The Householder transform is used to obtain a ground-plane circular SAR (CSAR) signal phase history from the slant-plane CSAR phase history by inverting the linear shift-varying system model, thereby circumventing the need for explicitly computing a pseudo-inverse. The Householder transform has recently been shown to have improved error bounds and stability as an underdetermined and ill-conditioned system solver, and it is computationally efficient. The Fast CSAR algorithm is a high-resolution and high-speed algorithm that may find applications in diagnostic medicine, leading, for example, to earlier tumor detection. Because of the high-speed nature, the imaging algorithm can make ultrasonic imaging up to hundreds of times faster than current commercial ultrasound systems without a trade-off in resolution, an important issue in imaging dynamic targets, such as the human heart.

The research in harmonic analysis-based 2-D aperture synthesis was used to asymptotically expand the Green's function-based Fourier Integral. Simulations revealed an analogy with the Fourier optics discipline. The diffraction patterns from simulations corroborated our experimental results. A Circular aperture was found to be the only practical aperture shape for airborne SAR out of various aperture shapes found in the Fourier optics discipline. The optimality of the circular aperture was also discussed.

The refocusing of defocused images was a spin-off of our research into 2-D aperture synthesis. Refocusing of images may be necessary in machine vision as a preprocessing step before edge detection or image segmentation in the imaging and manipulation of 3-D objects. The 2-D aperture synthesis generates a complex amplitude distribution and the

corresponding psf in a manner similar to the Fraunhofer diffraction distribution model and its psf as seen in Fourier optics. The matched filter utilized in the 2-D aperture synthesis has a focus-in-altitude interpretation and may be varied to increase or decrease the radius of out-of-focus blur associated with a particular point spread function of scatterers of various heights.

Lastly, the σ–tree classifier has been demonstrated as a feasible and practical approach to SAR pixel data classification for rather specific target classes as those in late season rural land use estimation. These results indicate that the polarimetric/spatial σ–tree classifier is able to separate the C–band radar data into five late season land use classes: unpicked cotton, harvested fields, grassy fields, young pine stands and mature pine stands with an average user's specificity estimated to be about 90 percent, and to be no lower than about 74 percent. There is no significant loss in classifier performance for the harvested fields, grassy fields and mature pines when polarimetric information is not available. This is believed to be due to the lack of ground–canopy polarimetric interaction for these land use classes. Spatial inputs to a σ–tree classifier are required to segment these classes. On the other hand, loss of polarimetric information from spatial blocks of unpicked cotton and young pine stands significantly degrades classifier performance. This is due to the significant ground–canopy polarimetric interactions for these land cover classes.

7.2 Further Research

7.2.1 Elliptic Aperture Shape

An ellipse is a generalization of a circle. There is evidence of elliptic aperture shape in Fourier optics and the associated mathematical development is also available for study. An elliptic aperture shape is a flyable airborne SAR aperture, unlike triangular or rectangular aperture shapes. Therefore, elliptic aperture synthesis may be studied as a topic of future research as a generalization of circular aperture synthesis. Elliptic aperture synthesis would come in handy during reconnaissance and surveillance when the target to be imaged is asymmetric along one of the two orthogonal axes.

7.2.2 More Mathematical Tools

7.2.2.1 Differential Geometry

SAR imaging appears to be a problem in geometry rather than electromagnetics. We know from our understanding of 1-D SAR that for a linear flight path SAR image reconstruction is done in the Cartesian coordinate system. In 2-D SAR for a circular flight path CSAR image reconstruction is done in the polar or cylindrical coordinate system. Therefore, the choice of coordinate system is dictated by the flight trajectory. On the other hand, differential geometry is a mathematical discipline that uses the methods of differential and integral calculus to study problems in geometry and has grown into a field concerned more generally with geometric problems on differentiable manifolds. It appears that in solving more challenging SAR $\omega - k$ image reconstruction problems like non-linear manoeuvring SAR, passive SAR and bistatic SAR, we may have to rely on mathematical tools in differential geometry.

7.2.2.2 Finite Difference and Finite Element Methods

A lot of work has recently been done in developing finite difference and finite element methods. These mathematical methods have found applications in computational electromagnetics, image processing, computer graphics, heat transfer, diffusion and aerodynamics to name a few. SAR imaging is a study in inverse problems. A wealth of knowledge base exists in this area of inversion and experts from all imaging related disciplines including medical imaging, seismic imaging, sonar imaging, etc., tap this knowledge base. Equipped with these recent mathematical tools, research into numerically viable techniques needs to be done as future work. We will have to dive into the knowledge base of "inverse problems" contributed primarily by physicists and mathematicians with our understanding of the SAR problem.

REFERENCES

[1] J. Burki and C. F. Barnes, "Sar with two-dimensional aperture synthesis," in *Proc. IEEE International Radar Conference (Radar'2007)*, Waltham, MA, April 18 2007, pp. 590–595.

[2] ——, "Interpolation-free algorithm for sar 2d aperture synthesis," in *Proc. SPIE International Algorithms for Synthetic Aperture Radar Imagery XIII*, Kissimmee, FL, April 18 2006.

[3] ——, "Beam raster scanning for 2d flyover sar," in *Proc. IEEE International Workshop on Sensor Array and Multichannel Signal Processing (SAM'2006)*, Waltham, MA, July 13 2006, pp. 339–343.

[4] ——, "Csar processing using householder transform," *IEEE Trans. Image Process.*, vol. 17(10), pp. 1900–1907, Oct 2008.

[5] ——, "Fast csar imaging," in *Proc. SPIE International Algorithms for Synthetic Aperture Radar Imagery XV*, Orlando, FL, March 17 2008.

[6] ——, "Refocusing of defocused images using sar2 algorithm," in *Proc. SPIE International Advanced Signal Processing Algorithms, Architectures, and Implementations XVIII*, San Diego, CA, Aug 27 2007.

[7] C. F. Barnes and J. Burki, "Late-season rural land-cover estimation with polarimetric-sar intensity pixel blocks and σ-tree-structured near-neighbor classifiers," *IEEE Transactions on Geoscience and Remote Sensing*, vol. 44(9), pp. 2384–2392, Sept 2006.

[8] M. Soumekh, *Synthetic Aperture Radar Signal Processing with MATLAB Algorithms*. New York, NY: Wiley Interscience, 1999.

[9] M. I. Skolnik, *Radar Handbook*, 2nd ed. New York, NY: McGraw-Hill, 1990.

[10] D. L. Mensa, *High Resolution Radar Cross-section Imaging*. Norwood, MA: Artech House, 1991.

[11] G. Franceschetti and R. Lanari, *Synthetic Aperture Radar Processing*. New York, NY: CRC Press, 1999.

[12] D. R. Wehner, *High Resolution Radar*. Norwood, MA: Artech House, 1995.

[13] W. G. Carrara *et al.*, *Spotlight Synthetic Aperture Radar Signal Processing Algorithms*. Norwood, MA: Artech House, 1995.

[14] H. Zmuda and E. N. Toughlian, *Photonic Aspects of Modern Radar*. Norwood, MA: Artech House, 1994.

[15] D. Gabor, "A new microscope principle," *Nature (London)*, vol. 161, pp. 777–778, 1948.

[16] E. N. Leith and J. Upatnieks, "Reconstructed wavefronts and communication theory," *J. Opt. Soc. Am.*, vol. 52, p. 1123, 1962.

[17] ——, "Wavefront reconstruction with diffused illumination and three-dimensional objects," *J. Opt. Soc. Am.*, vol. 54, pp. 1295–1301, 1964.

[18] R. E. Blahut, *Theory of Remote Image Formation*. Cambridge, UK: Cambridge University Press, 2004.

[19] G. F. Roach, *Green's Function*, 2nd ed. Cambridge, UK: Cambridge University Press, 1982.

[20] I. Stakgold, *Green's Function and Boundary value Problems*, 2nd ed. New York, NY: Wiley Interscience, 1998.

[21] P. M. Morse and H. Feshbach, *Methods of Theoretical Physics, Parts I and II*. New York, NY: McGraw-Hill, 1953.

[22] B. C. Barber, "Theory of digital imaging from orbital synthetic aperture radar," *Int. J. Remote Sensing*, vol. 6, p. 1009, 1985.

[23] C. Elachi, *Spaceborne Radar Remote Sensing: Applications and Techniques*. New York, NY: IEEE Press, 1987.

[24] J. C. Curlander and R. N. McDonough, *Synthetic Aperture Radar Systems and Signal Processing*. New York, NY: Wiley Interscience, 1991.

[25] J. W. Brown and R. V. Churchill, *Complex Variables and Applications*, 7th ed. New York, NY: McGraw-Hill, 2003.

[26] N. Bleistein and R. A. Handelsman, *Asmptotic Expansion of integrals*. Mineola, NY: Dover Publications, 1986.

[27] C. Cafforio *et al.*, "Sar data focusing using seismic migration techniques," *IEEE Trans. Aerospace and Electronic Sys.*, vol. 27(2), pp. 194–207, 1991.

[28] A. S. Milman, "Sar imaging by ω-k migration," *Int. J. Remote Sens*, vol. 14, pp. 1965–1979, 1993.

[29] M. Soumekh, "A system model and inversion for synthetic aperture radar imaging," *IEEE Trans. Image Process.*, vol. 1, pp. 64–76, Jan. 1992.

[30] A. F. Peterson *et al.*, *Computational Methods for Electromagnetics*. Piscataway, NJ: IEEE Press, 1998.

[31] A. Papoulis, *Systems and Transforms with Applications in Optics*. New York, NY: McGraw-Hill, 1968.

[32] J. Lopez-Sanchez and J. Fortuny-Guasch, "3-*d* radar imaging using range migration techniques," *IEEE Trans. Antennas and Propagation*, vol. 48(5), pp. 728–737, May 2000.

[33] M. Cheney, "A mathematical tutorial on synthetic aperture radar," *SIAM Rev.*, vol. 43, pp. 301–312, 2001.

[34] C. J. Nolan and M. Cheney, "Synthetic aperture inversion for arbitrary flight paths and nonflat topography," *Inverse Problems*, vol. 18, pp. 221–235, 2002.

[35] R. Stolt, "Migration by fourier transform techniques," *Geophysics.*, vol. 43(1), pp. 23–48, Feb. 1978.

[36] N. Bleistein *et al.*, *Mathematics of Multidimensional Seismic Imaging, Migration, and Inversion*. New York, NY: Springer, 2000.

[37] A. V. Oppenheim *et al.*, *Discrete-Time Signal Processing*, 2nd ed. Englewood Cliffs, NJ: Prentice Hall, 1999.

[38] N. N. Lebedev, *Special Functions and their Applications*. Mineola, NY: Dover Publications, 1972.

[39] I. G. Cumming and F. H. Wong, *Digital Processing of Synthetic Aperture Radar data Algorithms and Processing*. Norwood, MA: Artech House, 2005.

[40] J. W. Goodman, *Introduction to Fourier Optics*, 2nd ed. New York, NY: McGraw-Hill, 1996.

[41] J. D. Gaskill, *Linear Systems, Fourier Transforms, and Optics*. New York, NY: Wiley Interscience, 1978.

[42] M. Born and E. Wolf, *Principles of Optics*, 7th ed. Cambridge, UK: Cambridge University Press, 1999.

[43] D. Corr and A. Rodrigues, "Coherent change detection of vehicle movements," in *Proc. IGARSS, Seattle, Washington*, July 1998, pp. 2451–2453.

[44] D. H. Johnson and D. E. Dudgeon, *Array Signal Processing Concepts and Techniques*. Englewood Cliffs, NJ: Prentice Hall, 1993.

[45] B. F. Burke and F. Graham-Smith, *Radio Astronomy*. Cambridge, UK: Cambridge University Press, 1997.

[46] J. L. Walker, "Range-doppler imaging of rotating objects," *IEEE Trans. Aerospace and Electronic Sys.*, vol. 16(1), pp. 23–52, Jan. 1980.

[47] D. A. Ausherman *et al.*, "Developments in radar imaging," *IEEE Trans. Aerospace and Electronic Sys.*, vol. 20, pp. 363–400, July 1984.

[48] D. C. Munson *et al.*, "A tomographic formulation of spotlight-mode synthetic aperture radar," *Proceedings of the IEEE*, vol. 71(88), pp. 917–925, Aug. 1983.

[49] J. C. V. Jakowatz *et al.*, *Spotlight-mode Synthetic Aperture Radar a Signal Processing Approach*. Norwell, MA: Kluwer Academic Publishers, 1996.

[50] F. Natterer, *The Mathematics of Computerized Tomography*. New York, NY: Wiley Interscience, 1986.

[51] M. Soumekh, "Reconnaissance with slant plane circular sar imaging," *IEEE Trans. Image Process.*, vol. 5, pp. 1252–1265, 1996.

[52] ——, *Fourier Array Imaging*. Englewood Cliffs, NJ: Prentice Hall, 1994.

[53] J. Demmel and N. J. Higham, "Improved error bounds for underdetermined system solvers," *SIAM J. Matrix Anal. Appl.*, vol. 14(1), pp. 1–14, Jan. 1993.

[54] G. H. Golub and C. F. V. Loan, *Matrix Computations*, 3rd ed. Baltimore, MD: Johns Hopkins University Press, 1996.

[55] A. Björck, *Numerical Methods for Least Squares Problems*. Philadelphia, PA: SIAM, 1996.

[56] J. W. Demmel, *Applied Numerical Linear Algebra*. Philadelphia, PA: SIAM, 1997.

[57] C. L. Lawson and R. J. Hanson, *Solving Least Squares Problems*. Philadelphia, PA: SIAM, 1995.

[58] W. Givens, "Computations of plane unitary rotations transforming a general matrix to triangular form," *SIAM J. Matrix App. Math*, vol. 6, pp. 26–50, 1958.

[59] A. S. Householder, "Unitary triangularizaiton of a nonsymmetric matrix," *J. Assoc. Comput. Math*, vol. 5, pp. 339–342, 1958.

[60] P. Businger, "Linear least squares solutions by householder transformations," *Numerische Mathematik*, vol. 7, pp. 269–276, 1965.

[61] M. Subbarao *et al.*, "Focused image recovery from two defocused images recorded with different camera settings," *IEEE Trans. Image Process.*, vol. 14(1), pp. 23–48, 1995.

[62] J.-H. Lee *et al.*, "Implementation of a passive automatic focusing algorithm for digital still camera," in *Proc. IEEE International Conference on Consumer Electronics*, Aug 1995, pp. 449–454.

[63] J. M. Tenenbaum, "Accommodation in computer vision," Ph.D. dissertation, Stanford Univ., Palo Alto, 1971.

[64] J. H. Debes *et al.*, "High contrast imaging with guassian shaped pupils," *Proceedings of the SPIE*, vol. 4860, pp. 138–148, Feb. 2003.

[65] L. Lastras *et al.*, "All sources are nearly successively refinable," *IEEE Trans. Inf. Theory*, vol. 47, no. 3, pp. 918–926, Mar. 2001.

[66] S. Nawab *et al.*, "Approximate signal processing," *J. VLSI Signal Process*, vol. 15, no. 1/2, pp. 177–200, Jan. 1997.

[67] C. F. Barnes, "Successive approximation source coding and image enabled data mining," in *Proc. Data Compression Conf., Snowbird, UT*, March 23 2004, p. 525.

[68] C. F. Barnes *et al.*, "Vector quantizers with direct sum code-books," *IEEE Trans. Inf. Theory*, vol. 39(2), pp. 565–580, 1993.

[69] F. D. Frate *et al.*, "Crop classification using multiconfiguration c-band sar data," *IEEE Trans. Geosci. Remote Sens.*, vol. 41, no. 7, pp. 1611–1619, July 2003.

[70] R. O. Duda *et al.*, *Pattern Classification and Scene Analysis*. Hoboken, NJ: Wiley, 1973.

[71] C. F. Barnes *et al.*, "Coding and quantization," *DIMACS Series in Discrete Mathematics and Theoretical Computer Science*, vol. 14, pp. 33–53, 1933.

[72] M. Y. Zaidan *et al.*, "Use of sigma-trees as constellations in trellis-coded modulation," *IEEE Trans. Inf. Theory*, vol. 43, no. 6, pp. 2005–2012, Nov. 1997.

[73] P. R. Kersten *et al.*, "Unsupervised classification of polarimetric synthetic aperture radar images using fuzzy clustering and em clustering," *IEEE Trans. Geosci. Remote Sens.*, vol. 43, no. 3, pp. 519–527, Mar. 2005.

[74] C. Cortes and V. Vapnik, "Support-vector networks," *Mach. Learn.*, vol. 20, no. 3, pp. 273–297, Sept. 1995.

[75] R. Gupta and A. O. Hero, "High-rate vector quantization for detection," *IEEE Trans. Inf. Theory*, vol. 49, no. 8, pp. 1951–1969, Aug. 2003.

[76] A. Dembo and I. Kontoyiannis, "High-rate vector quantization for detection," *IEEE Trans. Inf. Theory*, vol. 48, no. 6, pp. 1590–1615, June 2002.

[77] C. F. Barnes *et al.*, "Advances in residual vector quantization: A review," *IEEE Trans. Image Process.*, vol. 5, no. 2, pp. 226–262, Feb. 1996.

[78] G. F. Hughes, "On the mean accuracy of statistical pattern recognizers," *IEEE Trans. Inf. Theory*, vol. 14, no. 1, pp. 55–63, Jan. 1968.

[79] K. Fukunaga and D. M. Hummels, "Bias of nearest neighbor error estimates," *IEEE Trans. Pattern Anal. Mach. Intell.*, vol. 9, no. 1, pp. 103–112, Jan. 1987.

[80] G. Lugosi and K. Zeger, "Concept learning using complexity regularization," *IEEE Trans. Inf. Theory*, vol. 42, no. 1, pp. 48–54, Jan. 1996.

[81] H. Daschiel and M. Datcu, "Cluster structure evaluation of a dyadic k-means algorithm for mining large image archives," in *Proc. Int. Conf. Pattern recognit.*, vol. 3, 1996, pp. 361–369.

[82] M. Datcu *et al.*, "Advanced value adding to metric resolution sar data: Information mining," in *Proc. 4th Eur. Conf. Synthetic Aperture Radar*, 2002, pp. 409–412.

[83] J. Li and R. Narayanan, "Integrated spectral and spatial information mining in remote sensing imagery," *IEEE Trans. Geosci. Remote Sens.*, vol. 42, no. 3, pp. 673–685, 2004.

[84] G. B. Marchisio and J. Cornelison, "Content-based search and clustering of remote sensing imagery," in *Proc. IGARSS, Hamburg, Germany*, vol. 1, Jun. 1999.

[85] R. G. Congalton *et al.*, *Assessing the Accuracy of Remotely Sensed Data: Principles and Practices*. Boca Raton, FL: CRC, 1999.